UNIVERSITY
OF TRENTO - Italy
DEPARTMENT OF INDUSTRIAL ENGINEERING

XXIX cycle

Doctoral School in Materials, Mechatronics and Systems Engineering

Novel PM Tool Steel with improved hardness and toughness

Faraz Deirmina

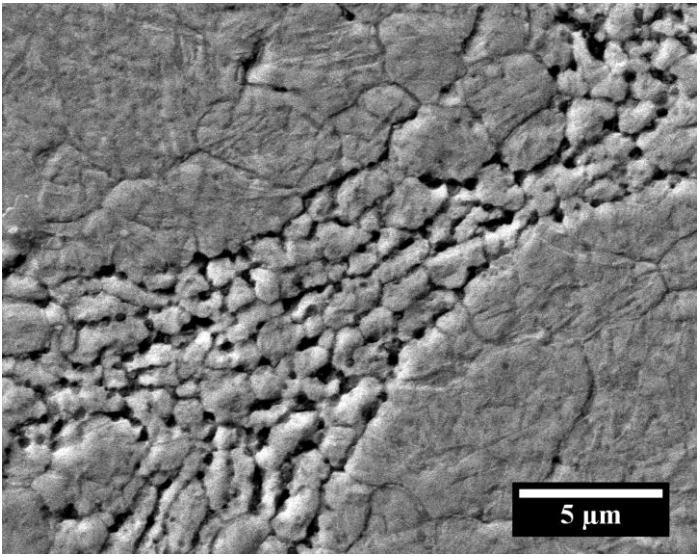

September 2017

NOVEL PM TOOL STEEL WITH IMPROVED HARDNESS AND TOUGHNESS

Faraz Deirmina
E-mail: Faraz.deirmina@unitn.it

Approved by:

Prof. Massimo Pellizzari -, Advisor
Department of Industrial Engineering
University of Trento, Italy.

Ph.D. Commission:

Prof. Alberto Molinari,
Department of Industrial Engineering
University of Trento, Italy.

Prof. Maurizio Vedani,
Department of Mechanical Engineering
Politecnico di Milano, Italy.

Prof. Elena Gordo ODÉRIZ,
Department of Materials Science and Engineering and Chemical Engineering
University of Carlos III de Madrid, Spain.

University of Trento,
Department of Industrial Engineering
September 2017

University of Trento - Department of
- - - - - - - - -

Doctoral Thesis

Name - 2017
Published in Trento (Italy) – by University of Trento

ISBN: - - - - - - - - -

To my wife, my comrade Camellia,
and her adorable children
Oblomov, Truffaut and Hugo

Abstract

Ultrafine grained (~ 1µm) steels have been the subject of extensive research work during the past years. These steels generally offer interesting perspectives looking for improved mechanical properties. UFG Powder Metallurgy hot work tool steels (HWTS) can be fabricated by high energy mechanical milling (MM) followed by spark plasma sintering (SPS). However, similarly to most UFG and Nano-Crystalline (NC) metals, reduced ductility and toughness result from the early plastic instabilities in these steels. Industrialization of UFG PM Tool Steels requires the application of specific metallurgical tailoring to produce tools with sound mechanical properties or in a more optimistic way, to break the Strength-Toughness "trade-off" in these materials. Among the possible ways proposed to restore ductility and toughness without losing the high strength, "Harmonic microstructure" design seems to be a very promising endeavor in this regard. Harmonic microstructure materials consist of a tunable volume fraction of evenly spaced "isolated" coarse-grained particles (CG) surrounded by a 3D interconnected network of UFG particles. CGs provide ductility and toughness, while high strength is guaranteed by the interconnected network of UFGs. This peculiar design offers an extra work hardening due to the generation of geometrically necessary dislocations at the interfaces of UFGs and confined CGs that are essentially present to accommodate the strain gradient imposed by the inhomogeneous (bimodal grained) microstructure.

The first part of this work is devoted to the development of PM tool steels with harmonic microstructure. Due to the difficulties of processing hard tool steel particles according to the methods reported in the literature, an economical, simple alternative approach is also proposed. Near full density "Harmonic structure" AISI H13 samples were produced using different volume fractions of UFG/NC mechanically milled (MM) and CG as-atomized particles followed by short time (30 min) low-temperature (1100°C) SPS. A combination of high hardness and significantly improved fracture toughness was achieved for the blends containing more that 50% UFG particles. The optimized mechanical properties was achieved by the mixture of 60% UFG particles where the sample showed a hardness near to the value predicted by the rule of mixtures (i.e. 405 HV10 vs. 406 HV10) while apparent fracture toughness (Kapp) was about 10% higher than that of predicted by the same rule (i.e. 52.0 MPa*m1/2 vs. ~47.0 MPa*m1/2). A toughening effect was evidenced for the samples essentially showing harmonic microstructure. Toughening was interpreted to be the result of the deviatory effect of coarse-grained round atomized particles together with energy

dissipation by decohesion at the CG/UFG or UFG/UFG interfaces leading to a local drop of the driving force for the crack propagation. The design allowed to easily adjust the strength and toughness to meet the specific application-oriented requirements. The harmonic steel was also subjected to Thermal Fatigue (TF) testing. The preliminary results confirmed that this microstructure combined the beneficial effects of both of its constituents, i.e., the low crack nucleation rate of CG H13 and the low crack propagation rate of UFG H13, thus showing the lowest pyrocracking factor. Moreover, TF crack deflection as an extrinsic toughening mechanism was evidenced in Harmonic Microstructure.

The second part of this work deals with the production and characterization of a PM HWTS reinforced with partially stabilized zirconia (PSZ). HWTS composites show improved hardness and remarkable wear resistance but generally also a systematic lower fracture toughness than the base material. Deteriorated toughness in metal matrix composites (MMCs) with a high strength matrix is mainly interpreted as a result of early damage initiation at the hard particles (HPs) or Matrix-HP interface. This damage can be even anticipated in the presence of readily damaged HPs (i.e. processing related flaws). Selection of PSZ as reinforcement was aimed at improving the strength and fracture toughness of the composite by taking advantage of the transformation toughening effect of PSZ. Two different types of PSZ, different volume fractions (10 and 20 vol. %) and sizes of reinforcement were used. Mechanical Alloying (MA) was used to process the composite powders to refine the matrix microstructure and both the matrix and PSZ particle size hence increasing the strength of the PSZ particles according to the Griffith strength formalism, and also to overcome the aggregation problems. Powders were consolidated by (SPS). The influence of processing parameters on density and microstructure was investigated. Short time (30 min) low-temperature (1100°C) consolidation by SPS allowed preserving the refined microstructure while achieving a maximum relative density of 98.6%. Moreover, short time sintering did not allow the extensive formation of thermodynamically plausible reaction products at the PSZ-H13 interface. As a result of dispersion hardening, the hardness of the as-sintered composites (i.e. maximum hardness of ~ 920 HV10) was increased compared to the mechanically milled UFG H13 (i.e. ~ 755 HV10), while in comparison to the as-atomized H13 (i.e. ~ 640 HV10) the improved hardness was ascribed to the synergic effect of dispersion hardening, microstructural refinement and strain hardening induced by MA. In these composites, tempering resistance at 550°C and 650°C was significantly improved due to the dispersion hardening effect. The hot compressive yield strength of the composites at 650°C and 450°C was increased up to 1.8 times the unreinforced UFG H13. *t to m* transformation during hot compression was evidenced and contributed to the strengthening. The hardness of the composites in heat treated condition (i.e. ~ 600 HV10) was significantly improved compared to that of the unreinforced matrix (i.e. ~ 420 HV10) while the apparent fracture toughness was drastically decreased to half the Kapp of the base material (19 MPa*m1/2 vs. 36 MPa*m1/2). However, the fracture toughness was slightly higher than that of a TiC reinforced H13 (i.e. 17 MPa*m1/2) with the same hardness (i.e. ~ 600 HV10).

Table of contents

"All human knowledge takes the form of interpretation"

Walter Benjamin

Chapter I
Introduction

1.1 Strength and Toughness, two mutually exclusive properties

A fundamental requisite for a broad range of engineering materials is the proper combination of strength and toughness. However, these properties are usually mutually exclusive[1]. Strength is consistently considered as a measure of material's resistance to permanent deformation (e.g. plastic deformation in ductile materials) whereas toughness is literally a measure of the amount of energy absorbed by the material before fracture. Therefore, the capability of undergoing plastic deformation will increase the toughness of the material by the aid of local energy dissipation which would otherwise be spent for fracture. In general, the toughness in polycrystalline metallic materials is tightly correlated to the plasticity corresponding to the dislocation motion. However, energy dissipation can be linked to several other *intrinsic* and *extrinsic* toughening effects in steels and other types of engineering materials such as ceramics[1].

The strength of steels is predominantly dependent on the difficulty of dislocations mobility[2]. Therefore, the basic understanding of strength and temperature dependence of strength is determined by the crystal structure, which in turn gives information on the slip systems, Burgers vector, and also lattice frictional stresses (i.e. Peierls stress)[2]. Demand for much higher strength steels has invoked the need of introducing structural and microstructural complexities. Some of the strengthening methods which are of interest in the present work are briefly introduced and their influence on toughness and ductility is discussed accordingly.

1.1.1 Grain boundary strengthening

The well-known Hall-Petch equation can describe the relation between Yield stress and grain size in a polycrystalline material [2].

$$\sigma_0 = \sigma_i + KD^{-1/2} \quad (1)$$

where σ_0 is the yield stress, σ_i is the "friction stress," K is a constant representing the "relative" hardening contribution of grain boundaries and D is the grain size. The model is based on the experimental evidence that grain boundaries act as obstacles to dislocation motion.

The equation is originated from the consideration that for grain with diameter D which sends dislocations from its interior to pile up at the grain boundary, a certain *critical shear stress* (τ_c) at the tip of the pile up must be applied to overcome the grain boundary barrier and to continue slip. Thus by putting the (τ_c) equal to the applied resolved shear stress minus the lattice friction stress (the stress that resists against dislocation movement), the minimum resolved shear stress to cause yield can be calculated. Eq.1 can be described by expressing the considerations above regarding axial stresses. However, the Hall-Petch equation cannot be used for nano-sized grain materials (D<100 nm) due to the validity limitation of Eq.1 when dealing with small pile-ups (less than 50 dislocations). In this case, a different model, which directly correlates the dislocation density (inversely proportional to grain size) to the strength and avoids the stresses at the grain boundaries (Eq.2), seems to be more appropriate[3]. It is noteworthy to mention that for BCC steels, K' is reported to be lower in case of grain sizes less than 0.23 μm where the number of dislocations is lower than 20 [4]. However, there is no clear understanding on the nature of the curve and the slope (K') at grain sizes below ~ 10-15 nm.[5]

$$\sigma_0 = \sigma_i + \alpha G b \rho^{1/2} = \sigma_i + \alpha G b D^{-1/2} = \sigma_i + K' D^{-1/2} \quad (2)$$

A similar relation also holds for indentation hardness[6]. Moreover, a similar relation stands for the cleavage fracture strength and fatigue resistance of high strength ultrafine grain and nanostructured steels.

1.1.2 Strengthening from fine hard particles

In dispersion hardening, the hard particles (e.g. ceramics) are mixed with the matrix material and processed by taking advantage of some processing routes including Powder Metallurgy (PM). An obvious advantage of dispersion hardening compared to conventional precipitation hardening and age hardening is that in the latter the solubility of the second phase in the matrix at elevated temperatures might hinder the high-temperature strength. On the other hand, a non-soluble second phase in dispersion hardened material can guarantee excellent thermal stability and a significant resistance to recrystallization and grain growth compared with the matrix material [2].

The strengthening mechanism can be summarized into four main effects, i) the load transfer from matrix to particle in the presence of a strong interface [7], ii) the generation of dislocations at the matrix-reinforcement interface due to the coefficient of thermal expansion mismatch between the two components [8], iii) the Orowan strengthening due to the barrier to dislocation motion by hard particles (HPs) [9] and iv) the increased work hardening introduced by HPs [10]. Strengthening is strongly dependent on the HP volume fraction, size and distribution inside the matrix which gives rise to the critical concept of "inter-particle spacing." A very simple definition of inter-particle spacing or mean free path can be written as:

$$\lambda = \frac{4(1-f)r}{3f} \quad (3)$$

where *f* is the volume fraction of (spherical) particles of radius *r*. As an example, the contribution of Orowan strengthening is inversely proportional to λ, and in the presence of a high strength matrix, it can be written as a Hall-Petch type equation[2]:

$$\Delta\sigma = \sigma_0 + K\lambda^{-1/2} \quad (4)$$

The work of Shewfelt and Brown[11] defines the contribution of "Dispersion Hardening" in terms of temperature (T) and strain rate ($\dot{\varepsilon}$) dependency of the ability of dislocations to overcome the obstacles by local climb (i.e. the dislocation remains in its slip plane except at the particle)

$$\sigma_p = \frac{Gb}{\lambda}[(0.51 \pm 0.01) + (0.12 \pm 0.02)log\left(\frac{\dot{\varepsilon}kTR^2}{4\pi\rho b^2 a_v G\lambda D_0}\right) + (0.052 \pm 0.009)\left(\frac{Q}{kT}\right)] \quad (5)$$

where G is the shear modulus, b the Burgers vector, D_0 is a pre-exponential component of the self-diffusion coefficient of iron ferrite, Q is the activation energy for self-diffusion, k is the Boltzmann constant, $\dot{\varepsilon}$ is the strain rate, R is the particle radius, λ is the square inter-particle spacing and a_v is the area associated with a vacancy. The equation is very similar to Eq.4, from which it is derived.

1.1.3 Strain hardening

Strain hardening or cold working is a well-known and widely used strengthening process for metals and alloys which cannot be hardened by heat treatment. In a polycrystalline metal, plastic deformation results in an increased number of dislocations and a higher state of internal stress can be achieved as a result of their interaction.

In the field of powder metallurgy, Mechanical Milling is considered as an efficient method to introduce both strain hardening and dispersion hardening to metal powders [6,12].

1.1.4 Martensite Strengthening

The transformation of austenite (γ-FCC) into martensite (α'-BCT) by rapid cooling via a diffusionless displacive transformation is the most common strengthening technique for steels. The outstanding strength can be ascribed to the lattice distortion by C atoms, to the presence of strong barriers against dislocation motion, i.e. plate (high C steels) and lath (medium/low C steels) martensite boudaries and also to substructural defects like twins (*plate* martensite) and very high dislocation density (*lath* martensite). All features listed above provide a considerable resistance against slip thus increasing the strength of the steel.

The main strengthening mechanism in martensite is attributed to the carbon atoms. Below 0.4% C content the hardness is highly dependent on the amount of carbon[2,13]. Upon quenching the steel (i.e. γ-α transformation), due to the solubility limit of carbon in α-ferrite, the carbon atoms strain the ferrite lattice and eventually redistribute by diffusion at room temperature to relieve the strain energy. This event leads to a strong engagement of carbon atoms and dislocations and puts a restriction on dislocation motion. Another strengthening mechanism can be explained by taking the formation of carbon atom clusters on {100} planes into account which in turn act as barriers to dislocation mobility[2].

Norstrom[14] proposed an equation (Eq.6) for the yield strength of low-medium carbon martensitic steel

$$\sigma_y = \sigma_0 + \sigma_1 + K_y D^{-1/2} + K_s d^{-1/2} + \alpha G b[\rho_0 + K(\%C)]^{1/2} \qquad (6)$$

where σ_0 is the lattice friction stress for iron, σ_1 is solid solution strengthening from alloying elements, d is the lath martensite width, D is the martensite packet size, and ρ_0 is the dislocation density of martensitic pure iron. The equation might additionally give an estimation of the effect of grain refinement corresponding to a decrease of either packet size or lath size on increasing the yield strength of the martensitic microstructure. On the other hand, the effect of strain hardening might be considered as included in the equation by taking the dislocation density into account.

So, in summary, it would be convenient to express the strength in terms of a linear contribution of each of the mechanisms above using a rough approximation that none of those are interacting[15].

$$\sigma_y = \sigma_0 + \sigma_g + \sigma_d + \sigma_s + \sigma_p \qquad (7)$$

where σ_0 is the strength of the annealed matrix, σ_g is the contribution of grain refinement, σ_d is the contribution of dislocation (strain hardening), σ_s stands for the solid solution hardening and σ_p represents the dispersion strengthening.

1.2 Effect of strengthening on fracture toughness and ductility

Apart from the *grain refinement*, all other strengthening mechanisms mentioned above have a negative influence on toughness and ductility of steel [16,17]. As an example, second phase hard particles are typically responsible for crack nucleation and propagation since the particles have a lower surface energy than the metallic matrix. These particles fracture at small deformations, increasing the probability of crack propagation at a very low energy [18]. The size, distribution and volume fraction of second phase particles are the most decisive factors to affect the toughness, as it will be discussed in detail later (section 1.5.2) in the present work.

Strain hardening would also lead to a drop in fracture toughness, especially in the case of the materials showing stronger hardening directly after yielding. Monotonic pre-strained quenched and tempered 4340 steel [19] showed a drastic drop of fracture toughness and an increase in yield strength by increasing the amount of pre-strain. The fracture toughness (mainly in ductile materials) is strictly dependent on the plastic strains at the crack tip which in turn is governed by the yield strength and the strain hardening properties, pre-straining might alter both factors thus affecting the fracture toughness.

1.2.1 Effect of grain refinement on fracture toughness

Most of the structural materials including low alloy steels exhibit a temperature dependent transition from ductile to brittle fracture which is related to the lattice frictional stress stated earlier. Many researchers [20,21] have claimed that the decisive properties to explain the plane strain fracture toughness of the sample when the crack propagates by cleavage are the yield strength (σ_y) and the cleavage fracture stress (σ_{cl}). Upon decreasing of the difference between these two stresses, as soon as yield occurs, small plastic strains (i.e. lower stresses) at the tip of the crack are needed to reach the critical stress for the cleavage. Therefore, the fracture toughness decreases drastically. The effect of grain size is schematically shown in Figure (1).

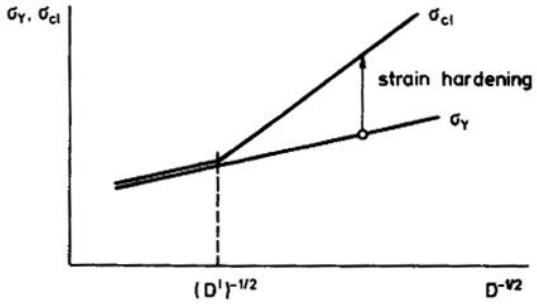

Figure I-1. Influence of grain size on yield (σ_y) and cleavage (σ_{cl}) stress[22]

The plot shows that by reducing the grain size, the difference gets larger thus an increase in fracture toughness is expected. It is not surprising that the cleavage stress of ferritic steels is dependent on the grain size (D):

$$\sigma_{cl} = 343 + 103D^{-1/2}(\mathrm{MN/m^2}) \quad (8)$$

The rise in fracture toughness by decreasing the grain size is however reported to show a threshold of 1 μm [23] below which, sparse yet contradictory results are found in the literature demonstrating the effect of microstructural refinement down to ultrafine grained (UFG) and nanocrystalline (NC) regime [24]. Drop in the fracture toughness might be related to an alteration of fracture mechanism from trans-crystalline fracture to a mixed intercrystalline and trans-crystalline mode by refining the grain size down to less than 1 μm [25].

Due to the limitations in producing samples with dimensions required for the test, the data on Charpy impact tests of UFG steels is very limited. The impact test results (small specimen) of a UFG (0.2 wt.% C) steel with grain size equal to 1.3 μm showed that the upper shelf absorbed energy (e.g. room temperature in this case) of UFG steel is much lower compared to the coarse-grained counterpart [23]. However, the DBTT (ductile to brittle transformation temperature) was decreased by refining the grain size. (Figure 2)

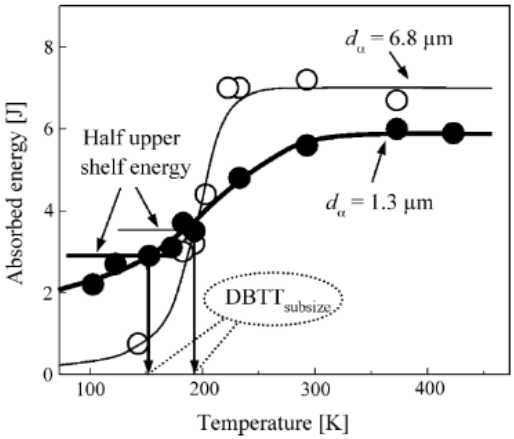

Figure I-2. Dependence of the Charpy impact test properties on temperature of the 0.2%C steels with different ferrite grain sizes[23]

The drop of DBTT by grain refinement should not be surprising, since as described earlier the critical stress of fracture increases more rapidly than the yield stress by refining the grain size.

1.2.2 Effect of grain refinement on ductility

The effect of grain refinement on ductility is even more challenging, while numerous reports exist on superior room temperature tensile strength of UFG steels processed through various microstructural refinement techniques [26–28] all of those also agree on the deterioration of the amount of work hardening in these steels. The reduced work hardening which negatively affects the tensile ductility can be perceived by the high *yield ratios* (σ_y/σ_{UTS}) [4].Therefore in theses steels, smaller "uniform" elongation is expected. Figure (3) clearly shows the grain size dependence of ductility in BCC steels. Two main explanations of reduction of tensile ductility by grain refinement down to UFG regime can be found in literature so far.

1. Dynamic recovery (softening) leads to a reduction in apparent work hardening rate. Within deformation, the dislocations that accommodate the intragranular strain are trapped in grain boundaries. Therefore, the kinetics of dynamic recovery is linked to the spreading of trapped dislocations at the grain boundary [29,30]. In the UFG steels, the time required for the dislocations to move into the boundaries is shorter than

the time of tensile testing [31]. Thus the decrease of dislocation density inside the grain negatively influences the work hardening in comparison with coarse-grained steels.

2. Taking the Considère criterion into account, the condition that satisfies tensile plastic instability is when the work hardening rate (i.e. slope of the true stress-true strain curve) is equal to the true stress, Eq. (9). At this point, the uniform elongation is overwhelmed by the neck initiation.

$$\frac{d\sigma_t}{d\varepsilon_t} = \sigma_t \quad (9)$$

As discussed above, on one side, UFG steel shows very high flow stresses at the early stages of plastic deformation but, on the other one, its work hardening capacity is reduced. As a consequence, the plastic instability occurs soon after plastic deformation which demolishes the ductility by suppressing the uniform elongation.

Ma [32], in the frame of an interesting article, has summarized the additional ***extrinsic causes*** to explain low toughness and ductility of UFG and NC materials processed from powders. A fully dense bulk NC material is very difficult to process. Therefore poor sample quality leads to very low fracture strength. The residual porosity, weak interparticle bonding, residual stresses, and impurities would all trigger early plastic instability and brittle fracture in tension.

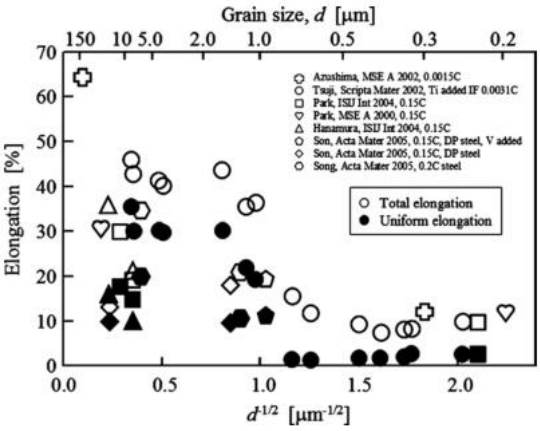

Figure I-3. Grain size dependence of ductility in some BCC steels, black symbols represent uniform elongation and hollow symbols total elongation[4]

1.3 Powder Metallurgy tool steels

The first and foremost distinctive competence which is the driving force for applying PM processing route for the fabrication of tool steels is the feasibility of avoiding or minimizing the segregation of carbides (Figure 4). Compared to the conventional methods such as casting and forming [33,34], PM parts show enhanced strength, wear resistance and enhanced isotropy. The latter is due to the absence of a continuous interconnected network of grain boundary carbides that act as preferential paths for crack propagation which is usually observed in conventional counterparts. (Figure 5)

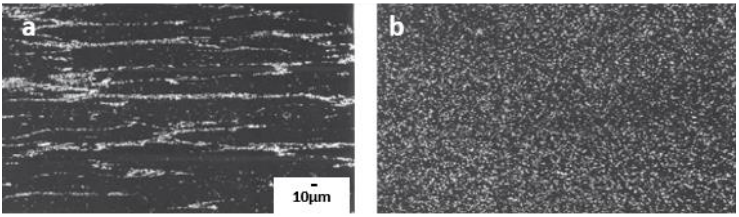

Figure I-4. Microstructure of conventional HSS (a) in comparison with PM HSS (b) at the same magnification, carbides are white in both micrographs

This potential stems from the gas-atomization of the molten batch of pre-alloyed steel which is characterized by much higher solidification rates compared to conventional large ingots. Higher solidification rate in small atomized particles opposes the segregation of carbides. The other advantage of PM route is the capability of producing parts with complex geometries and with minor material loss and small machining. The production of PM tool steels has been a topic of both academic and industrial interest since 70's [35]. Since then, many endeavors have been undertaken to produce and characterize novel tool steels and tool steel matrix composites via PM production routes.

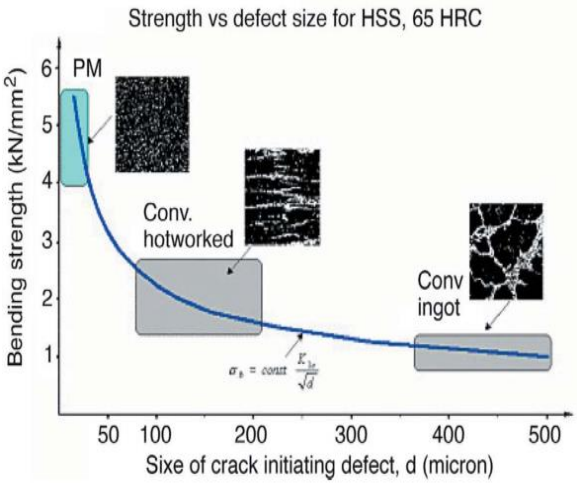

Figure I-5. Effect of carbide structure on fracture initiation and bend fracture strength

1.3.1 Microstructural refinement of powders and processing of composite powders

Atomized powders can be used in the as-received state for consolidation purposes. However, the need of microstructural refinement to increase the strength of the consolidated compact has led to the use of several syntheses and processing techniques such as high energy Mechanical Milling (MM) to refine both *particle size* and *microstructure*[5]. The former is generally seen in MM of powders with high hardness (e.g. tool steel powders) and is a crucial point of attention during sintering, for the smaller particle size provides a higher driving force for sintering due to the higher surface energy. Moreover, non-equilibrium solid-state processing techniques such as Mechanical Alloying (MA) have been introduced to produce a variety of *composite powders* showing equilibrium or metastable phases which cannot be processed using any other technique [36]. The other advantages of MA and MM are the capability of production of bulk quantities of the material at room temperature, by implementing very simple equipment.

1.3.2 Mechanical Milling and Mechanical Alloying

The ball milling process initially was used to coat hard phases (e.g. WC) with softer metals (e.g. Ni) [12]. It was also reported that the metal powders could undergo repeated fracturing and cold-welding by the aid of ball milling process. The intense

cold working induced by the collision of the balls during MM affects the thermodynamically stable state of the material by introducing a huge quantity of lattice imperfections such as dislocations and interfaces at room temperature[37,38]. The grain size reduction is characterized by the formation of high energy grain boundaries in which the atomic arrangement does not own any long or short range order. Mechanical Milling has been applied successfully to a large number of metallic powders [6,39,40] to obtain an UFG or nanosized microstructure within the powders. On the other hand, MA of metal powders (ductile-ductile system) [41] or metallic powders with ceramic hard particles (ductile-brittle system) [42] have frequently been reported to yield novel composite materials after proper consolidation. The latter will be briefly described as it is related to a part of the present work.

As it is shown in Figure (6a), in the first stages of mechanical alloying the ductile powders get flattened due to the impact of the balls while the brittle HPs are fragmented. The fine fragmented HPs then are trapped in the lamellas of the ductile matrix. Upon further milling, the ductile matrix is highly work-hardened and undergoes fragmentation, and its lamellar microstructure is tangled and refined as depicted in Figure (6b). In this stage, the actual composition of individual powders should theoretically approach the nominal mixing composition, and the particle morphology becomes more or less spherical. By extending the milling time, the matrix microstructure will be further refined and the second phase (HPs) dispersion into the matrix becomes more uniform (Figure 6c) giving rise to the formation of composite powders.

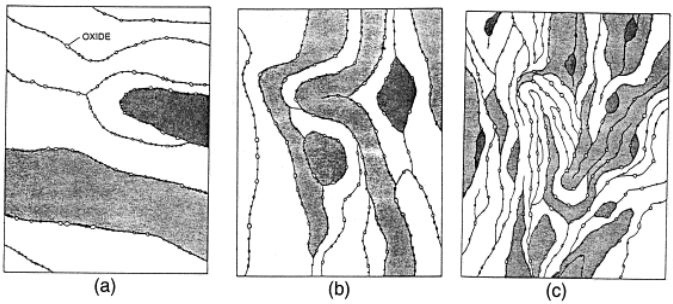

Figure I-6. Microstructural evolution during milling of ductile-brittle combination of powder,a) ductile powders get flattened and oxides are fragmented and trapped in the matrix, b) ductile matrix is highly work-hardened ,refined and undergoes fragmentation while oxides are trapped in the refined lammellas and c) further refinemrnt of matrix microstructure, the figure represents the specific case of oxide dispersion strengthening [12]

The major drawback of MA process is the powder contamination during milling [12]. The small size of the powders, large surface area and generation of fresh new surfaces during the fragmentation process all contribute to the powder contamination. While too many sources of contamination can be effective during MA, the primary cause of contamination in most cases is the milling atmosphere. The leakage of air into the milling container can easily contaminate the powder through nitrogen and oxygen pick-up. For example, the formation of cubic phase during long time milling of Ti was evidenced and attributed to the formation of TiN [43]. Pellizzari et al. [44] have also reported oxygen and nitrogen pick-up during ball milling of AISI H13 steel. Oxides can play a detrimental role in consolidation by impeding the strong interparticle bonding. The presence of oxides might further alter the fracture mechanism of the consolidated UFG and NC materials, from this viewpoint the contamination during MA or MM might have a two folded effect on the mechanical properties of these materials.

1.3.3 Consolidation techniques

Due to the high hardness of atomized tool steel powders and low sintering activity of these alloys, a fully dense bulk cannot be obtained by conventional pressing and sintering[45]. PM Tool steels are mainly produced by Hot Isostatic Pressing (HIP) in mass production[46]. New technologies such as hot extrusion sintering, metal injection molding and spark plasma sintering are considered as attractive routes for the fabrication of advanced materials with improved mechanical properties[44,47].

1.3.3.1 HIP Consolidation

Tool steel inert gas atomized powders are often consolidated using Hot Isostatic Pressing (HIP) followed by hot forming (e.g. extrusion, forging or rolling) [33,46,48,49]. The technique involves the application of isostatic pressure at high temperatures in a vessel [50]. Encapsulated powders or sintered components thus are densified to yield more isotropic and improved mechanical properties. Figure (7) shows the density-temperature maps for various particles sizes of Tool Steel powders HIPed with a pressure of 100 MPa (i.e. industrial practice).

As it can be deduced from the Figure, the principal mechanism of densification till reaching a relative density of 98% is the power law creep regime in which the contribution of applied pressure in densification is the greatest since $\dot{D} \propto P^n$, where $\dot{D}$ is the densification rate and P is the applied pressure. The retained porosity (~2%) is most likely to be removed by the grain boundary diffusion which is mainly

dependent on temperature. Holding time helps the promotion of creep and completion of consolidation.

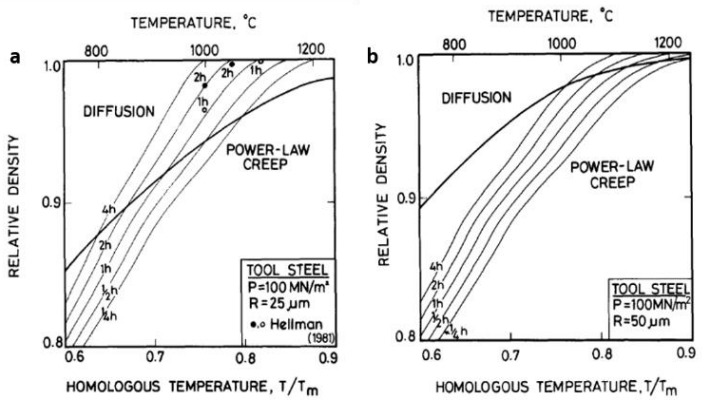

Figure I-7. Density-temperature maps at P=100 MPa for tool steel with particle sizes of a) 50 μm and b) 100 μm [46]

As reported by Takigawa et al. [51] a near fully dense (~99%) tool steel can be achieved using different pressure/temperature values in less than 1 hour by HIPing. However, the response of the sample to mechanical testing is totally different. For example, in Figure (8a), it can be clearly observed that the fully dense sample HIPed at 1000°C and 100 MPa is showing an inter-particle fracture suggesting that even if the applied pressure was high enough to plastically deform the particles and promote densification, the temperature was not sufficiently high to promote the diffusion for a complete consolidation and development of strong bonding. On the other hand, the sample processed at 1200°C and 20 MPa shown Figure (8b) demonstrates an entirely different fracture surface on which no particle boundary is traceable. The result suggests that a strong bonding is developed between the powder surfaces thanks to the processing at higher temperatures.

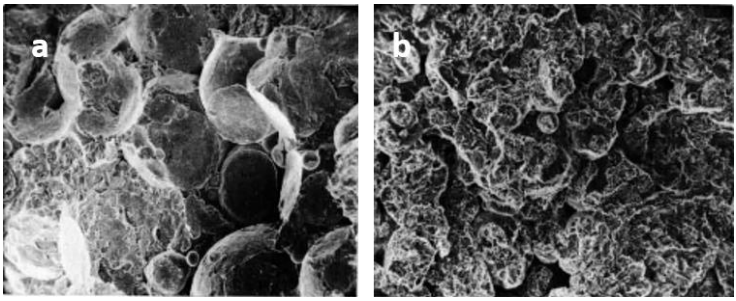

Figure I-8. Fracture surfaces (magnification: 150x) of bend test samples both showing ~99% relative density, a) 1000°C, 100 MPa and b) 1200°C, 20 MPa [51]

Processing at high temperature for longer holding times might be detrimental for the MM or MA powders which are microstructurally refined down to UFG and NC regime due to a high probability of *recrystallization* and *grain growth*. For instance, a comprehensive study [52] on annealing the work-hardened MM Fe powders (~HV 950 and crystallite grain size less than 20 nm) suggests that, at a temperature lower than 850°C, 30 minutes of holding is enough to cause local strain relief, followed by recrystallization and grain growth. A considerable increase in crystallite size was observed especially at temperatures above 650°C. Therefore, the industrial practice of HIPing tool steel (i.e. 1100°C, 4 h, 100 MPa) imposes a significant risk of grain growth and the deterioration of work hardened refined microstructure of MM and MA powders. While for the latter, the second phase particles added to pin the grain boundaries might have positive effects on lowering the kinetics of grain growth.

1.3.3.2 Spark Plasma Sintering

A successful alternative approach to consolidate MM or MA steel powders is *Spark Plasma Sintering (SPS)* [53–56]. Numerous experimental reports suggest that densification of metal powders and ceramics by SPS can be achieved in shorter times and at lower temperatures and pressure levels compared to the conventional Hot Pressing (HP) or HIP [57]. The schematic of an SPS apparatus is depicted in Figure (9).

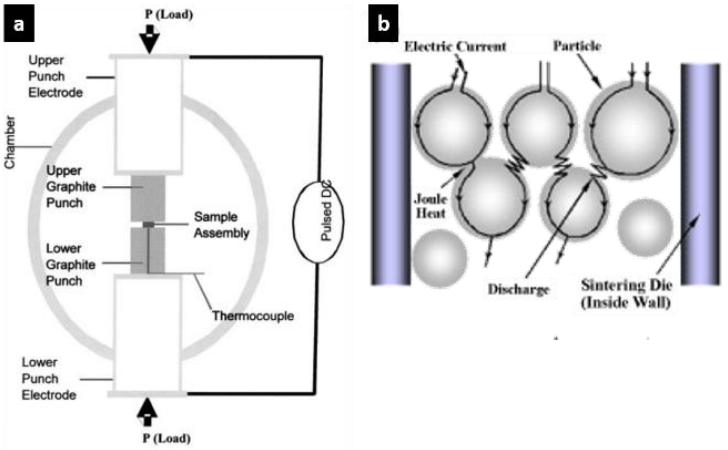

Figure I-9. a) Schematic representation of SPS apparatus [58], b) pulsed current flow through powder particles [59]

SPS is characterized by the consolidation of powders under the concurrent influence of a low voltage, high current electromagnetic field, and uniaxial pressure. Powders fill the sintering die (e.g. graphite die) and heating is provided by passing a pulsed DC (Direct Current) through the die and powders (in the case of sintering of conductive powders) and uniaxial pressure is simultaneously applied through the punches. The distinctive competence of SPS compared to HP or HIP includes i) application of a pulsed DC and ii) high heating rates, which lead to the achievement of a fully dense material at lower sintering temperatures and shorter times. The thermal effect of current (i.e. Joule heating) facilitates the achievement of high heating rates (up to 1000°C/min) that can suppress grain coarsening by by-passing the surface diffusion mechanism. The efficiency of the process has been pointed up to the consolidation of refined MM and MA powders while retaining the desirable NC or UFG microstructure [54,60,61].

The short sintering time might oppose the formation of thermodynamically plausible parasitic reaction phases at the interface of matrix/reinforcement in MA powders which may have been otherwise formed by the extension of sintering time. Moreover, experimental evidence can be found in literature confirming electric field induced dielectric breakdown of non-conductive surface oxides at the inter-particle contact areas during spark plasma sintering of metallic powders resulting in enhanced inter-particle bonding [62–64]. Surface cleaning from oxides is of great importance while dealing with tool steel particles since the risk of surface oxidation is very high even

by a careful handling and by using proper protection systems [65,66]. Apart from Joule heating, there is still ambiguity on the inherent characteristics of the electric field on the processing of conductive and non-conductive materials which is far from the scope of the present thesis [62].

A study on consolidation of MM-UFG High-Speed Steel powder clearly shows that the refined microstructure impelled by MM is retained after 5 minutes of SPS at 1130°C (Figure 10b)[53]. Much finer and homogeneously distributed carbides could be achieved in comparison with HIP/Forging processing (Figure 10a). The homogeneous carbide distribution and refined carbide size gave rise to improved 0.2% proof compressive yield stress by 21% (i.e. ~3600 vs. 3000 MPa for conventional HIP/Forged) at room temperature and 6% (i.e. 2500 vs. 2350 MPa for conventional HIP/Forged) at 550°C for MM/SPS samples.

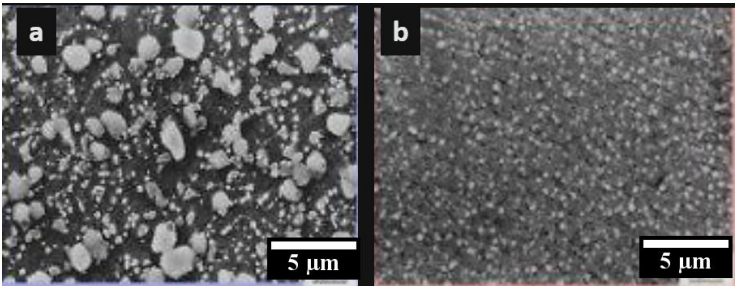

Figure I-10. SEM micrographs of a) conventional PM HSS processed by HIP/Forging and b) MM/SPS HSS[53]

1.4 AISI H13 Tool Steel

The contemporary narrative of tool steels begins in a small town near Sheffield (UK), where Benjamin Huntsman, a clockmaker, developed the crucible melting process in the 18th century. The process allowed to achieve cast steels with a carbon content that fell between the wrought irons and that of cast irons. The steels could be hardened by heat treatment and found their application in cutting and machining the other metals. Since then, the tooling industry has frequently introduced many types of tool steels with complex microstructures and various alloying elements. The modern tool steels show a combination of hardenability, red hardness, toughness, and wear resistance. AISI H type tool steels are characterized by a very good combination of properties. They are used in quenched and tempered condition and show high toughness, high hot strength, good thermal conductivity, tempering resistance and low coefficient of thermal expansion. The tempering temperature is often between 550 to 650°C depending on the service temperature. The motivation

behind tempering is to trigger the formation of secondary carbides of the carbide forming alloying elements (i.e. Cr, Mo, W, and V) which is known as secondary hardening process. The secondary carbides retard the softening at elevated temperatures and also guarantee the high hot hardness (strength)[67]. AISI H13 is a chromium hot work tool steel which is widely being used as dies for Al or Mg extrusion, die casting dies, forging dies and tools thanks to its good wear (abrasion) resistance, high hardness and good toughness.

1.4.1 Research progress in production of UFG PM AISI H13

While a considerable number of research works are dealing with the hot isostatic pressing of AISI H13 tool steel and tool steel matrix composites [68,69], very limited attention has been paid to the consolidation of this steel via SPS. The work of Fedrizzi et al. [70] showed that it was possible to obtain an UFG AISI H13 by short time SPS of NC and UFG mechanically milled powders. Mechanical Milling of gas atomized H13 powders was conducted using Fritsch Pulverisette 6 planetary mono mill at 450 rpm under vacuum. Spheres with 10 mm diameter of 100Cr6 (63HRC) and a ball to powder weight ratio (BPR) of 10:1 was selected. At the early stages of the high energy MM (i.e. 200 min), both particle size and crystallite size showed a sharp reduction. The cellular microstructure of the Atomized powders showing micro-segregated areas as a consequence of the rapid solidification process was totally destroyed. Finally, a nearly homogenous UFG lamellar microstructure was achieved. The continuation of MM resulted in further slight particle size refinement, similarly to the crystallite size as shown in Figure (11).

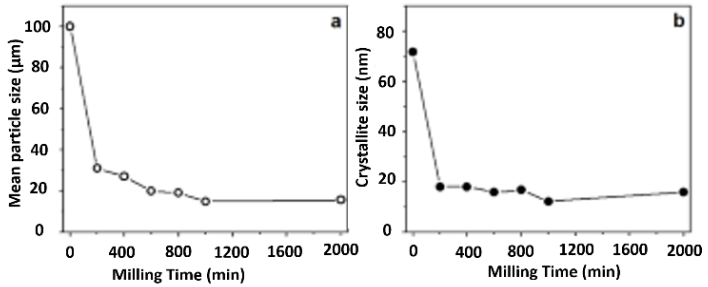

Figure I-11. Mean particle size (a) and Crystallite size (b) as a function of milling time[70]

The powders were then consolidated by SPS at 1100°C for 5 min to yield a UFG microstructure as depicted in Figure (12b).

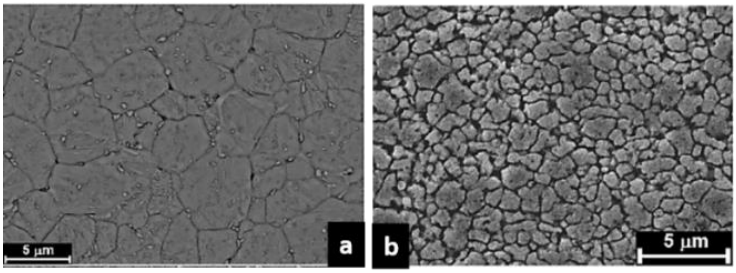

Figure I-12. SEM micrographs of SPS a) atomized H13 and b) MM-H13 [71]

The MM-H13 samples showed higher hardness than the atomized counterpart (Figure 12a) both in as sintered (800 HV10 vs. 640 HV10) and also in heat treated condition (quenching from 1020°C in a 5bar nitrogen, followed by double tempering at 625°C). However, a drop in fracture toughness was evidenced (58 MPa $m^{1/2}$ vs. 77 MPa $m^{1/2}$). This drop was ascribed to i) the effect of grain size reduction down to 1um, ii) oxygen pick-up during high energy milling that resulted in a higher concentration of surface oxides impeding the formation of strong metallic bonding, and iii) the slightly lower relative density of the MM samples compared to the as atomized ones (99.4% vs. 99.6%) due to the lower compressibility of strain hardened MM particles.

1.5 Particle reinforced Hot Work Tool Steels

Particle reinforced tool steel matrix composites (MMCs) are developed to increase the wear resistance of the tool. The designs aim at integrating of the high toughness of metallic matrix and superior hardness of the hard particles to develop an excellent wear resistant material [72]. A strong motivation behind the production of these composites is the increasing demand of abrasive wear resistance for dies used in the extrusion of lightweight metal matrix composites (i.e. Aluminum and Al alloys reinforced with SiC). The interaction of hard ceramic particles (HPs) with the die can severely damage and decrease its lifetime. A dramatically high die wear is observed when processing MMCs using conventional tool steels as die material [73]. Pagounis et al. [69] have shown that the incorporation of 12 vol. % reinforcing particles (i.e. VC or Cr_3C_2) in a PM hot work tool steel led to increased three-body abrasive wear resistance up to seven times, compared to the matrix base material.

Even if PM is more expensive than conventional processing routes such as casting, the *particle* reinforced tool steel matrix composites are generally produced via *PM* routes due to improved mechanical properties as discussed earlier. The atomized

powders are mechanically milled or mixed with the hard particles of the second phase (i.e. ceramics) in a ball mill or mixer; the powders are then consolidated mostly using HIPing to obtain a fully dense material[18,72].

1.5.1 Role of HPs in Densification of MMCs

In general, the solid state consolidation of MMCs is carried out at sintering temperatures well below the melting point of HPs. Therefore, the HPs should be considered as rigid, non-deformable particles during densification. Recalling the densification mechanism in HIP and SPS (i.e. plastic deformation, power law creep, grain boundary and bulk diffusion), consolidation of powder blends of HPs and matrix particles, called soft particles (SPs), is strongly dependent on HPs volume fraction, size (d), shape and the ratio of (d_{SP}/d_{HP}) [74–76].

At low vol. % of HPs (i.e. **isolated** HPs), upon application of the pressure at the processing temperature the matrix particles can deform and fill the holes in the vicinity of HPs and matrix particles contacts to accomplish the densification. By increasing the HP volume fraction, the risk of formation of HP **aggregates** becomes higher. In this case, filling the holes, namely the *excluded volume* [77] trapped in between of rigid HPs by the soft metallic matrix even by the application of high levels of pressure or long holding times (i.e. long creep time) is almost impossible. Therefore a fully dense material cannot be achieved. This drawback appears more detrimental when dealing with a very fine HP size compared to coarser HPs [75].

Upon further increasing the HP's vol. % a **percolating** HP network might be formed. The network may partly support the applied external pressure so that the effective pressure on softer metallic particles will be reduced which in turn leads to hindering of densification. On the other hand, in this condition, densification might progress by the rearrangement of the percolated HP network under the applied pressure. The ease of the rearrangement is dependent on the shape of HPs, the rearrangement of the spherical particles is easier compared to the irregularly shaped HPs. However, due to inherent brittleness of HP, rearrangements may be in accompany with *HP fracture and cracking* which will consequently demolish the expected mechanical properties of MMCs under mechanical load.

The vol. % thresholds of the three highlighted conditions (i.e. isolated, aggregated and percolated HPs) is tightly dependent on the d_{SP}/d_{HP} ratio (Figure 13). Moreover, since the increased contact area of HPs can hinder the densification in all three regimes described above, the spherical morphology which offers the lowest contact area between the hard particles is considered the optimum HP morphology with regard to ease of densification.

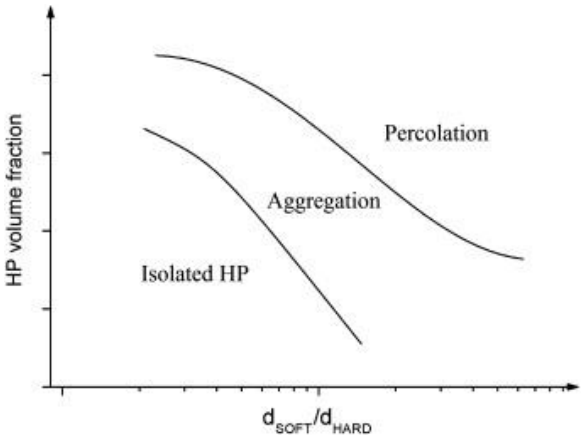

Figure I-13. Effect of hard particle volume fraction and particle size ratio on the densification behavior of hard and soft powder mixtures [78]

However, from a mechanical properties viewpoint, the strength of hard ceramic particles in the metallic matrix is highly dependent on their particle size. In the fine ceramic particles, the probability of the existence of processing related flaws (i.e. pores, inclusions and grain boundary fissures) exceeding the critical flaw size is very low. Therefore according to the Griffith strength formalism [79], the strength of fine HPs is higher than that of coarser ones. To overcome the percolation and aggregation of HP's, MA has been suggested by many researchers as a very efficient technique. MA provides a very homogeneous distribution of fine HPs in the metallic matrix thus by-passing the percolation threshold typically found by simple mixing of the powders [56,80–82].

1.5.2 Role of HPs in Mechanical performance of the steel matrix composites

Apart from the governing function of the hardenable metallic matrix, the critical parameters that influence the mechanical properties of MMCs are briefly described in the following.

1.5.2.1 HPs size and volume fraction

A fine HP size provides higher strength due to the reduced mean free path between hard particles. For the same reason, fracture toughness drops significantly. In the presence of a theoretically clean and seamless interface, when the stress at the

poles of the particles becomes high, the crack initiates and easily propagates inside the HPs. Therefore, at given HP content, the higher the number of HPs the higher the probability of crack initiation and consequent crack propagation either through the HPs or HP/Matrix interface [18]. Figure (14) schematically depicts the effect of HP size on the strength and fracture toughness of steel based MMCs. However, the *critical flaw size* in *ceramic particles* should also be considered. The probability of premature failure (initiated from particles) due to the presence of processing related flaws in larger ceramic particles is much higher than that of the finer ones [82]. Therefore, even if the schematic presentation in this figure can be assumed for a qualitative evaluation of strength and toughness, it cannot be a design guideline to produce MMCs with improved toughness using coarser HP sizes.

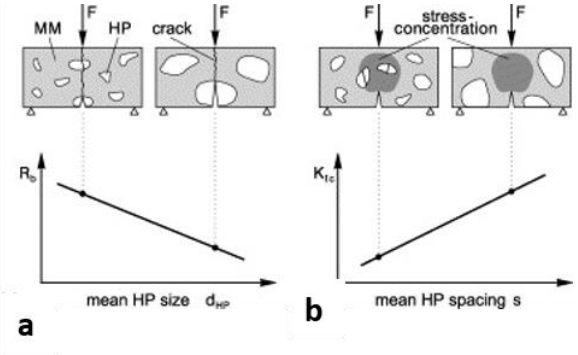

Figure I-14. (a) Bend Strength and (b) fracture toughness dependence of MMC on HP size [72]

Figure (15) clearly shows the influence of the HPs volume fraction and size on the impact toughness of hot work tool steel composites. No practical difference in impact toughness can be observed with regard to the size of the reinforcing particles. This conveys the fact that the *quantity* of processing related flaws *larger* than the critical flaw size serving as the locations of the initiating defect is much higher inside the coarse particles. These defects deteriorate the strength of the coarse ceramic particles and compensate for the positive effect of increased mean free path between them in view of mechanical properties of the MMCs. Moreover, it is shown that by increasing the volume fraction of HPs, a drastic drop in toughness is clearly evidenced. It is also noteworthy to mention that a very high volume fraction of reinforcement does not necessarily provide better wear resistance in hot work tool steels. Since in the presence of the secondary carbides, the martensitic matrix will not be able to support and accommodate excessive volume fractions of the second phase during the wear test due to the limited toughness, the matrix can not support

the reinforcing particles thus spalling of the HPs occurs easily [69,83]. Spalling of the HPs has a two folded effect on increasing the wear loss. Firstly, the pulled out HPs act abrasively in addition to the abrasive grits. Secondly, as a result of spalling, the mean free path (interparticle spacing) between HPs will be increased, and thus providing a larger mean free path for the action of abrasive media. The latter becomes crucial when the hardness of HPs is higher than that of the abrasive particles.

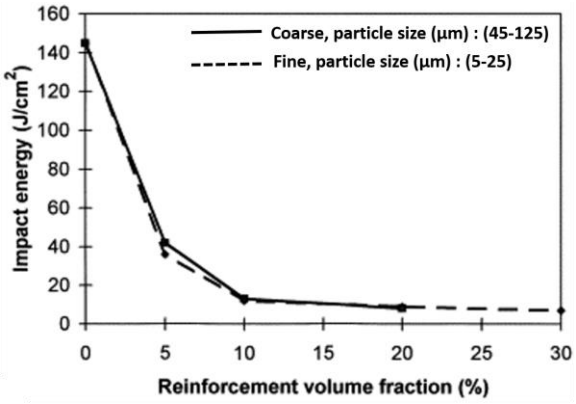

Figure I-15. Impact toughness dependence of hot work tool steel composite on size and vol.% of HPs (Cr_3C_2) [18]

1.5.2.2 HPs distribution in the Matrix

In addition to the effect of HPs dispersion on the densification behavior of composites, a homogenous distribution of HPs into the matrix provides isotropic properties of the MMCs which is essential to efficient use of load bearing capacity of HPs [84]. HPs clusters may promote crack initiation and linkage of the cracks under loading[85]. Therefore these clusters negatively affect ductility and fracture toughness in view of local fracture initiation toughness, crack growth toughness and global fracture toughness.

In order to obtain a homogenous distribution of HPs in a ductile matrix, a geometrical model based on the HP size (d_p) and matrix powder size (d_m) was proposed by Tan and Zhang [86]. This model includes the HPs volume fraction (f) and the strains induced to the samples by a secondary process (i.e. extrusion and/or rolling). The model is extended by Sabirov et al. [87] for the severe plastic deformation (SPD) processes that induce a high amount of shear strain (γ) to the sample (e.g. equal

channel angular pressing). Based on the model, the HPs distribution is expected to be homogenous when the HP size (d_p) is not smaller than a critical value.

$$d_p \geq \frac{d_m}{\left[\left(\frac{\pi}{6f}\right)^{\frac{1}{3}}-1\right]\frac{\sqrt{R}}{1-R'}\gamma} \quad (10)$$

where R is the extrusion ratio and R' reduction ratio during rolling. It appears that the large shear strains can effectively lower the critical size of HPs needed to achieve a homogenous distribution into the matrix. It was shown that in an extruded Al6061 powder metallurgy MMC reinforced with 20 vol. % fine Al_2O_3 particles showing diffused clusters elongated in the extrusion direction, 7 Passes of ECAP (i.e. introducing γ to Eq. 10) was sufficient to homogenize the particle distribution within the matrix[87]. As a result, the fracture toughness was increased from 1.5 to 2.7 KJ/m^2. Therefore, in order to achieve a homogeneous distribution of fine HPs inside the matrix, SPD processes seem to be highly efficient.

1.5.2.3 Matrix-Reinforcement Interface

Considering the possible different strengthening mechanisms of HPs in MMCs, load transfer and matrix strengthening models predominantly rely on the existence of a defect free and strong matrix/HP interface [88]. During solid state processing of composites, the interface can be classified according to the possible reactions between HPs and matrix into pure mechanical bond or reaction bond [18,89]. As a general rule, the formation of reaction zones at the interface can significantly affect the mechanical properties, since most reaction products are brittle [56]. However, there exist sparse results in the literature indicating that the formation of a limited (in size) reaction zone might improve the bonding between the matrix and the HPs thus improving the load transfer from matrix to the reinforcement [90].

Chapter II
The aim of the work

2.1 PM AISI H13 with "Harmonic Microstructure"

As author tried to introduce and rationalize the effect of grain refinement down to UFG regime on the deterioration of uniform elongation and toughness in ferritic steel, It would be thus of high *industrial importance* to imply some metallurgical practices to overcome ductility problem. One is to produce gradient grain microstructure in which, only the surface is characterized by (UFG) microstructure and the coarse grain (CG) core plate provides ductility. This can be achieved by implementing different mechanical or thermomechanical treatments [91–94]. A successful industrial practice is hot rolling close to the transformation temperature and high rolling strains to achieve UFG ferrite on the surface down to 0.25 thickness of the strips as a result of strain induced transformation from austenite to ferrite due to the large strains and high undercooling [95]. Other thermomechanical processes such as cryogenic rolling followed by secondary recrystallization are useful to produce heterogeneous bimodal grain materials [96]. Bimodal grain size microstructure can also be achieved through powder processing [97].

In theory, similar to the concept developed by Ashby[98] describing the deformation of plastically non-homogenous materials, the increased strain hardening capability in these heterogeneous microstructure materials stems from the storage of geometrically necessary dislocations (dislocations of the same sign). Since the coarser grains undergo higher plastic deformation than that of the UFGs, there will be a plastic deformation gradient build up in the microstructure. Accommodation of this plastic strain gradient requires the storage of geometrically necessary dislocations. The dislocation density gradient is maximum in case of randomly distributed CGs that are fully embedded inside the surrounding UFGs [99].

However, when considering the toughness, bimodal grain size materials do not always show a homogenous behavior due to the inhomogeneous distribution of fine grains inside the coarse grain matrix [100] or the grain shape and orientation dependency of toughness in severely plastically deformed grains [24].

An interesting extension to the gradient grains and heterogeneous bimodal grain size microstructures is realized by a powder metallurgical production route leading to

the achievement of the so-called *"Harmonic Microstructure"* [101], in which, instead of generating high strength and toughness very locally, as it appears in the aforementioned "gradient grain" structure, a 3D interconnected network of UFGs surrounding the CGs with fairly uniform spacings is formed in the bulk. This microscopically heterogeneous structure thus provides a homogenous combination of high strength thanks to the 3D interconnected network of UFGs and an acceptable level of uniform elongation provided by the strain hardening capacity of the enclosed coarser grained areas and also the generation of geometrically necessary dislocations at the interfaces of CGs and UFGs resulting in delayed plastic instability. As shown in Figure (1), this PM route involves the severe plastic deformation on the surface of powder particles to a certain depth by controlled mechanical milling and subsequent fast consolidation. The method thus allows the development of an interconnected network of UFG microstructure (*Shell*) surrounding a CG (*Core*) matrix. The mechanical properties strongly depend on the volume fraction and distribution of UFG *Shell* so that a controlled shell to core ratio provides excellent properties combination [102–105].

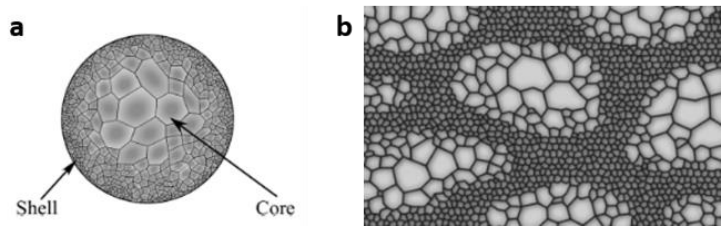

Figure II-1. Schematic representation of (a) milled powder and (b) consolidated material[106]

In most cases, the data reported in the literature is limited to pure metals (i.e. Ni, Cu, and Ti) and relatively low hardness alloys that show easy to deform FCC crystal structures (i.e. stainless steel). Dislocation interactions in materials with a BCC structure is accompanied with the formation of immobile dislocations, crack nucleation and finally brittle fracture of the powders. Therefore controlling the volume fraction of *Shell* seems to be impossible. Hence, in the case of BCC structured materials, an easier control of the volume fractions can alternatively be achieved by mixing and/or low energy mechanical milling of the desired vol. % of the MM-UFG particles with the as received powders. In this manner, the finer MM-UFG powders accumulate on the surface of the bigger as received powders (satellite structure) to yield a 3D interconnected network after consolidation.

The aim of the **first part** of this work is to evaluate the fracture toughness of a PM hot work tool steel with a harmonic microstructure obtained by mixing of UFG

mechanically milled (MM) and coarser grained as atomized (AT) powders consolidated by SPS. In a second step, the best performing harmonic microstructure has been subjected to thermal fatigue testing. Considering the industrial application of hot work tool steel for hot forging and die casting, surface damages by heat checking most likely occurs [107,108]. Heat checks are defined as a network of surface cracks which are formed because of the fatigue developed upon the repetition of thermal stresses. These stresses are generated because the expansion and contraction of the surface during heating and cooling is constrained by the core. Crack initiation at the surface of the tool impairs surface finishing and forces repairing operations. A deep propagation of these cracks may eventually trigger the tool failure. Resistance to heat checking can be improved by a combination of hot strength, ductility, and toughness together with inherent high thermal conductivity and low coefficient of thermal expansion. Thermal fatigue resistance evaluation of a harmonic microstructure can then be then of interest in its potential industrial application where the tool has to show a combination of high toughness and reasonable hardness together with high TF resistance. Therefore, the TF resistance of the harmonic PM AISI H13 tool steel is also investigated using a simple TF test equipment.

2.2 PM AISI H13-PSZ composites

Previous studies confirmed that the failure of MMCs with a high strength matrix initiates predominantly either from the HP or matrix-reinforcement interface [10,18,109]. Moreover, the difference between the coefficient of thermal expansion of matrix and reinforcement generates a hydrostatic tensile field of stress in the matrix upon cooling from the processing temperature, which in turn deviates the crack towards the matrix/reinforcement interface and lowers the fracture toughness [69]. One way to reduce the negative influence of the reinforcement on toughness is to select "Ceramic Materials" with relatively high stress to fracture and high fracture toughness.

Partially stabilized Zirconia (PSZ), firstly introduced by Garvie et al.[110] showed promising properties. Below 1170 °C, ZrO_2 transforms from the tetragonal phase *(t)* into a monoclinic structure *(m)*, accompanied by 3% to 5% volume expansion. In PSZ, by using dopants (e.g. Y_2O_3 or MgO) the tetragonal phase will be metastable at room temperature and shows stress-induced martensitic transformation into the monoclinic structure. In view of the aforementioned feature, PSZ shows higher fracture toughness (i.e. $K_{IC} \sim 8$ MPa $m^{1/2}$) in comparison with other ceramics as a result of the dissipation of the strain energy in the vicinity of the tip of a propagating crack due to the stress-induced transformation of the metastable tetragonal phase (*t*)

into the stable monoclinic one (*m*). Another toughening mechanism has been ascribed to the creation of compressive strain fields about the crack tip, due to the volume expansion resulting from *t* to *m* transformation, that opposes crack propagation [111]. In a PSZ containing composite, the effective volumetric transformation strain (θ_T) is defined by Eq. 1 [112]

$$\theta_T = C\theta_T^P \quad (1)$$

where *C* is the volume fraction of transforming particles and θ_T^P is the volumetric transformation strain of the particles when the particles are not constrained by the matrix. In a composite material containing small vol. % of transforming phase (i.e. PSZ), the effective volumetric transformation strain will be enhanced if the matrix material is not stiffer than PSZ (E ~ 210 GPa , ν = 0.3)[111,112]. The energy-dissipative stress induced phase transformation of PSZ thus can be expected to enhance the toughness of the tool steel matrix composite (E_{matrix} ~ 208 GPa) in comparison with the same tool steel reinforced with other ceramic compounds.

Partially stabilized zirconia shows much higher hardness compared to the metals. A good combination of both hardness and fracture toughness makes it a proper candidate as a tribological material [113]. PSZ shows the potential to enhance the abrasive wear resistance of the MMC more than other ceramic compounds not showing such kind of transformation. If there exists a strong bonding between PSZ and the matrix, volume expansion caused by phase transformation creates compressive zones at the tip of the propagating cracks which in turn opposes the linking up of these cracks and delays the particle removal by fracture [114].

The strengthening mechanism of PSZ in a metallic matrix was investigated by Martin et al. [115]. Incorporation of PSZ into a TRIP steel matrix led to an increase in the strength of the composite material with reference to the unreinforced alloy and also in comparison with the TRIP steel reinforced with a conventional HP (i.e. Al_2O_3). The load transfer to PSZ particles and energy dissipation due to the stress induced transformation before particle fracture or particle debonding was also well documented [115–117].

In the frame of the **second part** of the present work, the feasibility and mechanical properties of a tool steel matrix-PSZ composite by mechanical alloying and spark plasma sintering has been evaluated. Two different types of zirconia and different volume fractions of reinforcement is taken into consideration. Mechanical Milling is carried out to achieve a full dispersion of hard particles into the severely deformed tool steel matrix to pursue the synergistic effects of i) strain hardening and microstructural refinement due to severe plastic deformation and ii) dispersion hardening by HPs.

Chapter III
Materials and Experimental Procedures

3.1 Materials and fabrication of samples

3.1.1 Harmonic microstructure design

To tailor the feasibility of development of a Core/Shell Structure in AISI H13 gas atomized powders, controlled mechanical milling was performed. A commercial gas atomized AISI H13 powder (Table 1) was used.

Table III-1. Chemical composition of AISI H13 powder (wt. %)

	Fe	C	Cr	Mo	V	Mn	Si	N*	O*
AISI H13	Bal.	0.41	5.1	1.6	1.1	0.35	0.9	383	105

*in ppm

Particles showed an average size of 100 μm and the maximum particle size was lower than 150 μm. The initial micro-hardness was 710 HV0.1, in agreement with the martensite (plus some retained austenite) microstructure obtained during rapid solidification. A first powder batch was used in the *as-atomized* state (AT) while a second one was *annealed* (AN) to reduce hardness and to improve the strain hardening capability. Annealing was performed in a tubular furnace (Alumina tube) in a reducing atmosphere (20% H_2 and 80% Ar). Preheating rate was 0.5 °C/min up to 200°C, and powders were heated at a rate of 3.5 °C/min up to 860°C. Dwell time was set to 2 hours followed by slow cooling (0.5 °C/min) down to 560°C and subsequent free cooling to room temperature.

Powders were then subjected to low energy (controlled) mechanical milling using a Fritsch Pulverisette 6 planetary mono mill with a 500 ml vial using 100Cr6 steel balls under vacuum at room temperature for 16 hours. Parameters of the rotational speed (RPM) and ball to powder weight ratio (BPR) were chosen in order to reduce the

frequency of high energy impacts to avoid powder fragmentation during mechanical milling. Therefore, as suggested in previous research works[118],[119] the ball to powder ratio was set to 1.5:1(g/g) and the rotational speed of 150 rpm.

An alternative approach to producing harmonic-microstructure AISI H13 was also examined. The powders were subjected to high energy mechanical milling (MM) at 450 rpm under vacuum. The milling time was set to 200 min, and cycles of 2 min ON and 9 min OFF were chosen to reduce frictional overheating. The ball to powder ratio (BPR) was set to 10:1.5 (g/g). Seven powder samples were prepared of which two samples were mono-sized grain namely AT (0%MM) and 100%MM. The rest of the samples were prepared by mixing of the different fractions (20, 40, 50, 60 and 80 vol. %) of MM powders with the AT particles using a Turbula mixer for 60 min. Mixing was carried out to develop a satellite structure consisted of the finer UFG-MM powders fully covering the coarser AT ones.

It has to be noted that, for the production of Thermal Fatigue test samples (Section 3.2.8), to further homogenize the harmonic microstructure architecture, the MM powders were mixed with the AT ones and then the batch was subjected to a *low energy mechanical milling* for an hour. The reasoning behind this additional production step was that low energy milling allows finer MM particles to fully cover the coarser AT particle surfaces more homogenously forming a percolating 3D interconnected network after SPS. This process may also guarantee more uniform AT particles spacing inside the UFG-MM network. The complete list of materials is listed in table 2.

Table III-2. Description and codes of the samples

Sample code	Description
AT-H13	As received gas atomized powders
AN-H13	Annealed powders
AT-H13(16h)	Subjected to Low energy mechanical milling for 16h
AN-H13(16h)	Subjected to Low energy mechanical milling for 16h
MM-H13	High energy mechanically milled
20%MM	20 vol. % of MM-H13 mixed with 80 vol. % AT-H13
40%MM	40 vol. % of MM-H13 mixed with 60 vol. % AT-H13
50%MM	50 vol. % of MM-H13 mixed with 50 vol. % AT-H13
60%MM (HS)	60 vol. % of MM-H13 mixed with 40 vol. % AT-H13
80%MM	80 vol. % of MM-H13 mixed with 20 vol. % AT-H13

3.1.2 AISI H13 Tool Steel-PSZ composites

Commercial AISI H13 tool steel powder (d < 45μm) was selected as the matrix material (Table 3). Two different types of PSZ particles, namely Magnesia Partially Stabilized Zirconia (Mg-PSZ) and a commercial 3 mol. % Yttria Stabilized Zirconia (from now on referred to as 3Y-PSZ) with mean particle sizes equal to 5 and 0.5 μm respectively (Table 4), were selected as the reinforcement.

Table III-3. Chemical composition of AISI H13 (wt. %)

	Fe	**C**	**Cr**	**Mo**	**V**	**Mn**	**Si**	**O**
AISI H13	Bal.	0.38	5.1	1.0	1.4	0.35	1.0	0.05

Table III-4 Chemical composition of reinforcement (wt. %)

	$ZrO_2 + HfO_2$	Y_2O_3	SiO_2	Fe_2O_3	Al_2O_3	Na_2O	MgO	TiO_2
3Y-PSZ	Bal.	5.23	0.003	0.002	0.005	0.007	N/A	N/A
Mg-PSZ	Bal.	N/A	0.025	0.005	N/A	0.006	3.5	1.0

From the as-received powders sandwich like samples (H13/PSZ/H13) were consolidated (Figure 1) using the exact processing condition (i.e. the uniaxial pressure of 60 MPa , sintering temperature of 1100°C and 30 min holding time) planned to consolidate the MMCs. The samples were used to trace probable interfacial reactions between the matrix and reinforcement.

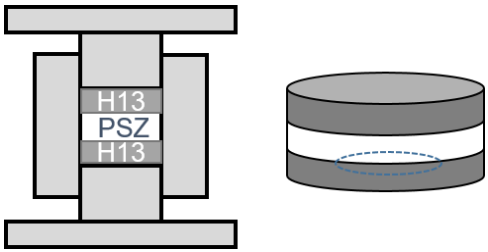

Figure III-1. Schematic of sandwich structure

Tool steel powder was mixed to 10 and 20 vol. % of reinforcement using a turbula mixer for 30 minutes. 0.2 wt. % Kenulube was added as the process control agent

(PCA). The powder mixture was then mechanically alloyed (MA) using a planetary mono mill under vacuum at a rotational speed of 450 rpm. The ball to powder ratio (BPR) was set to 10:1.5 (g/g). Milling was extended up to 340 minutes, and powders were collected after 90 min, 200 min and 340 min of milling to determine the optimum processing time. Cycles of 2 min ON (i.e. milling) and 9 min OFF (i.e. stop) were selected to avoid overheating. Air cooling suppressed drastic variations in vial temperature.

For the purpose of comparison, a TiC reinforced H13 were also produced under the same processing condition. The mean particle size of TiC powder was 3 µm. A list of developed composites specifying the reinforcement type, vol. % and mean particle size is listed in table 5.

Table III-5 composition and codes of MA powders

Sample code	Reinforcement vol. %	Reinforcement type	Reinforcement Mean particle size (µm)
MA(H13+10%Mg-PSZ)	10	Mg-PSZ	5
MA(H13+20%Mg-PSZ)	20	Mg-PSZ	5
MA(H13+10%3Y-PSZ)	10	3Y-PSZ	0.5
MA(H13+20%3Y-PSZ)	20	3Y-PSZ	0.5
MA(H13+20%TiC)*	20	TiC	3

* TiC reinforced H13 (i.e. MA(H13+20%TiC)) serving as a reference tool steel composite produced in lab of metallurgy using the same technique was just evaluated by means of fracture toughness and hardness

3.1.3 Spark Plasma Sintering

All Powders in this work were consolidated using a DR. SINTER® SPS1050 apparatus (Sumitomo Coal & Mining, now SPS Syntex Inc.) using graphite dies. The disc-shaped samples with small dimensions (20 mm in diameter, 7 mm in height) were heated at *100 °C/min* up to the sintering temperature (1100°C) and were held for 30 minutes. A pressure of 60 MPa was applied once the temperature reached 570°C. The samples were free cooled from the sintering temperature. Due to the limitation of the apparatus, heating rate could not exceed 50 °C/min for relatively large samples. Therefore, disks for the plane strain fracture toughness tests (30 mm in diameter and 7 mm height) and Thermal Fatigue test (40mm diameter and 20mm height) were consolidated using a lower heating rate (i.e. 50 °C/min).

Overall views of the production of harmonic microstructure and tool steel-PSZ composites are schematically shown in Figures (2a) and (2b) respectively.

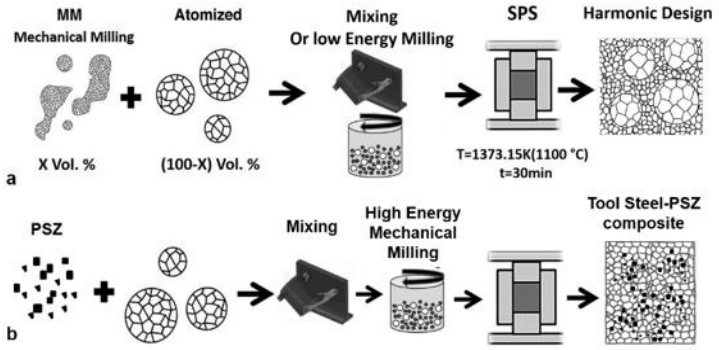

Figure III-2. Overall view of production routes, a) harmonic microstructure and b) tool steel-PSZ composite

3.1.4 Heat treatment

Samples were vacuum quenched from 1020°C x15 min using 5 bar nitrogen and tempered twice at 625°C for 2 h; the heating rate was set to 13 K/min.

3.2 Materials Characterization

3.2.1 X-ray diffraction

XRD data were carried out on powders and sintered samples using an Italstructures IPD3000 instrument equipped with a Cu anode source (line focus) (K_α=0.15418 nm), a multilayer monochromator to suppress k-beta radiation and fixed 100 µm slits. The samples were positioned in reflection geometry with a fixed omega angle with respect to the incident beam, and spectra were collected using an Inel CPS120 detector over the omega +120° two-theta range. Acquisition time was 1800 seconds per diffractogram.

The data was analyzed using Rietveld method (i.e. considering the area under peak proportional to the vol. % of the corresponding phase), and elaborated by MAUD (Materials Analysis Using Diffraction) software [120]. Mean crystallite size and the lattice average microstrain were calculated to tailor the effects of severe plastic deformation on the structural refinement.

Peak broadening is dependent on the instrument, lattice strain and mean crystallite size. After instrumental effect corrections, mean crystallite size and lattice strain are determined by the Scherrer formula

$$B = \frac{0.9\lambda}{dcos(\theta)} + \eta tg(\theta) \quad (1)$$

where *B* is the width of the peak at half of its height, *λ* is the radiation wavelength, *d* is the crystallite size, *η* is the lattice strain, and *θ* is the Bragg angle. The equation can be rearranged by multiplying both sides by *cos (θ)* to give a linear function of *θ*

$$Bcos(\theta) = (0.9\frac{\lambda}{d}) + \eta \sin(\theta) \quad (2)$$

where the slope (*η*) is the lattice strain. This method can be applied if the crystallite size distribution lies in the range of 10-100 nm[12].

3.2.2 Density measurements

Density measurements were done on as sintered specimen according to the "Archimedes" principle conforming to ASTM B962-08 [121]. The density of AISI H13 was considered to be 7.76 g/cm^3.

The density of composites was assumed to obey the linear " rule of mixtures."

$$\rho_{composite} = \rho_{H13}v_{H13} + \rho_{reinforcement}v_{Reinforcement} \quad (3)$$

where *ρ* and *v* are the absolute density and volume fraction respectively. The literature data on the absolute densities of 3Y-PSZ (6.05 g/cm^3) and Mg-PSZ (5.7 g/cm^3) were used.

3.2.3 Metallography

Sintered samples were cut by precision micro-cutting with a diamond blade. Metallographic sections were prepared by grinding with SiC papers up to 1200 grit followed by polishing with 3 µm and 1 µm diamond paste and chemical etching with Nital (5% nitric acid in ethanol solution) was carried out on sintered samples and powders. Sintered samples Microstructures and powder morphologies were investigated by Scanning Electron Microscopy (SEM). All semi-qualitative chemical analyses were performed by energy-dispersive X-ray spectroscopy (EDS). EDS line scan analysis and elemental mapping was carried out on sandwich samples and consolidated composites respectively to identify the possible formation of reaction layers.

3.2.4 Grain size measurement

Quantitative image analysis using the linear intercept method on SEM micrographs was implemented to measure the grain size of the samples. The results were elaborated according to ASTM E112-13.

3.2.5 Hardness measurements

Vickers hardness measurements on as sintered and heat treated samples was performed according to ASTM E92-82 [122]. The applied load was set to 10 Kg and the average of at least six indentations was reported.

Microhardness test was performed on the metallographic samples. Applied load was set to 0.05 N for the powders in order to eliminate the influence of the substrate. The load was set to 0.1 N for the bulks.

3.2.6 Measurement of yield strength

The yield strength of the harmonic microstructure samples was measured using spherical indentation according to the *empirical* method proposed by Herbert et al. [123]. The technique gives a good estimation of the yield stress for materials showing small yield strain (less than 1%) in which, yielding occurs well before any finite-deformation effects [124]. The advantages of this method are its nondestructive characteristics, relatively low cost and the possibility of applying the test on the small samples. For the construction of "stress-strain curves," the contact area during indentation has been calculated by the following equation

$$a = \sqrt{2h_cR - {h_c}^2} \quad (4)$$

where a is the contact radius, h_c is half the amount of h, the total displacement of the indenter into the sample, and R being the radius of the spherical indenter using the Hertz solution which is proved to be algebraically straightforward and precise in this context[123]. According to the observations of Tabor[125] and using Eq.5, it is possible to define the mean pressure (P_m) as the applied load (P) over the contact area.

$$P_m = \frac{P}{\pi a^2} \quad (5)$$

Following the work of Mesarovic and Fleck [124], the yield is observed when (a/R) (i.e. contact area divided by indenter radius) approaches 0.16, this ratio is independent of the magnitude of σ_y , Young's modulus, and Poisson's ratio. At this point, the mean pressure *(P_m= P/ πa²)* divided by 1.6, somewhat estimates the yield point of the material [123].

The stress and strain in the uniaxial tensile test are equivalent to:

$$\sigma_{indentation} \approx \frac{P_m}{\psi} \approx \sigma_{uniaxial\ tensile\ test} \quad (6)$$

$$\varepsilon_{indentation} \approx 0.2\frac{a}{R} \approx \varepsilon_{uniaxial\ tensile\ test} \quad (7)$$

where ψ is a constraint factor and it's value depends on deformation regime. The indentations was performed using MTS 810 mechanical testing machine on the surface of heat treated bulks, 6 × 3 × 30 mm^3 (W × B × L), gently polished (3μm cloth) to minimize the risk of strain hardening by grinding at small depth and also to reduce the surface roughness aimed at obtaining meaningful and accurate measurements . The indenter was a zirconia sphere (R =2.5 mm). The experimental results show a good agreement with the model predictions for the large spheres, but for the smaller spheres (e.g. R = 14 μm) the model significantly overestimates the hardness[126]. The displacement limit and displacement rate were set to 0.5 mm and 0.05 mm/s, respectively. In order to further validate the results, uniaxial tensile tests were carried out for the AT (i.e. 0%MM) and 100%MM sample using an Instron 1343 100KN testing machine. A schematic of the test configuration is shown in Figure (3).

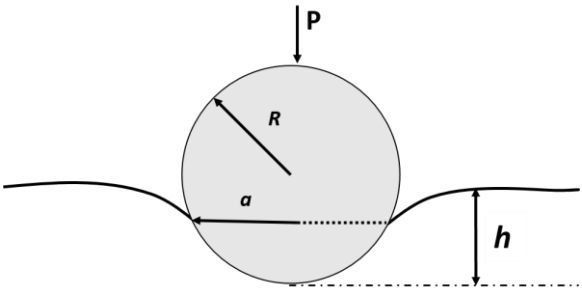

Figure III-3 schematic of spherical indentation on the surface of the samples

3.2.7 Fracture toughness

Fracture toughness tests have been carried out using a procedure suggested for small notched specimens[127]. Samples $6 \times 3 \times 30$ mm^3 ($W \times B \times L$) were cut from the heat treated disks. A notch with depth "a" equal to 0.5W and the root radii (ρ) of 50 μm was electro-discharge machined (EDM) in the samples. EDM may affect the microstructure in the vicinity of the crack tip especially due to the development of a heat affected zone (HAZ). However, EDM was performed using slow feed rate and relatively low current to reduce the thickness of the white layer and the HAZ. It should be also noted that fracture toughness data obtained in this thesis are only used to compare the toughness of the different samples which have all been undergone identical EDM processes.

Plane strain fracture toughness testing was performed using a 10-ton capacity universal tester. The specimens were loaded in three-point bending at a crosshead speed of 0.5 mm/min according to the ASTM E399-90 [128]. It has to be stated that the

use of a finite notch radius in place of a fatigue pre-crack, takes higher stress to reach the "critical stress intensity," therefore leading to apparent K_{app} values slightly greater than the corresponding K_{IC} obtained from fatigue pre-cracked specimen.

3.2.8 Thermal Fatigue test

Thermal fatigue testing was performed on three samples, namely the harmonic microstructure that showed the optimized mechanical properties, 100% UFG-MM and 0% MM (AT).
Dimensional specifications are shown in Figure (4). The thickness of the disk (20 mm) made it possible to develop a biaxial state of stress and bidirectional cracking on the surface. A condition which is similar to that observed in many industrial components [129].

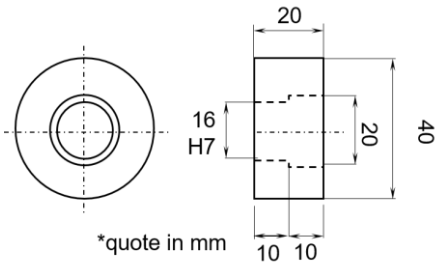

Figure III-4. Technical drawing of disks

TF tests were performed using a customary test rig as depicted in Figure (5). The rotating disc (8 rev/min) was induction-heated in a limited central portion of the external surface up to 660±10°C (i.e. higher than the tempering temperature of the samples) and rapidly cooled by a water jet (2l/min) down to 60°C. A beaker, continuously filled with flowing water, was also placed beneath the rotating disk to warranty the minimum temperature to be achieved. An infrared pyrometer continuously monitored the surface temperature.
Tests were interrupted after 200 and 500 cycles to evaluate surface thermal cracking after slightly polishing of the surface oxide layer. After 500 cycles metallographic cross sections parallel and perpendicular to the rotation direction were prepared to be analyzed by scanning electron (SEM) and optical microscopy (OM). The mean crack length (l_m), maximum crack length (l_{max}), crack density (ρ) and the product of these parameters, i.e. the so-called *Pyrocracking factor* (P) [129] were calculated using quantitative image analysis. For this purpose only cracks longer than 20 μm were taken into account.

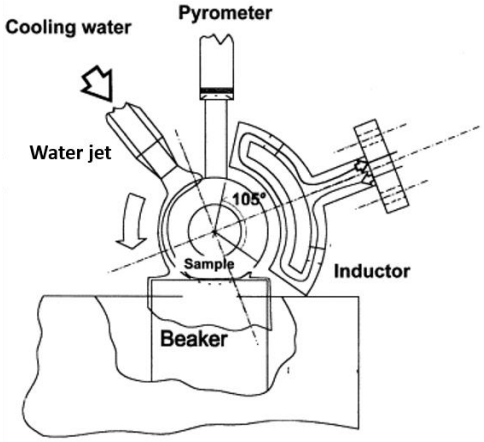

Figure III-5. Schematic view of the test rig

3.2.9 High-temperature chemical stability of composites

The chemical stability at the processing temperature was further studied by holding the consolidated samples at the SPS temperature (1100°C) under vacuum (5×10^{-4} mbar) for longer dwell times (i.e. 1 and 2 hours). The metallographic cross-sections were analyzed using EDS semi-quantitative analysis.

3.2.10 Tempering resistance

Tempering resistance testing was performed on cylinderes (10 mm in height , 5 mm in diamater) at 550°C and 650°C under vacuum (5×10^{-4} mbar), for a maximum holding time of 10 hours.

3.2.11 Hot Compression Tests

Cylindrical samples were extracted by electro-discharge machining (EDM) from the sintered cylinders, with the main axis along the pressing direction. Hot compression tests were carried out on these cylinders using a Bähr dilatometer model 805A/D at 650°C, 450°C and room temperature at a strain rate of 0.002 s^{-1} to 6% plastic strain.

Chapter IV
Results and Discussion

Part of this chapter has been published in:

F. Deirmina, M. Pellizzari, and M. Federici

"Production of a Powder Metallurgical Hot Work Tool Steel with Harmonic Structure by Mechanical Milling and Spark Plasma Sintering", *Metall. Mater. Trans. A, vol. 48, no. 4, pp. 1910–1920, Apr. 2017.*

F. Deirmina, M. Pellizzari

"Thermal fatigue resistance of a PM tool steel with bimodal grain size", *Proc. of 10th TOOL Conference, ASMET, the Austrian Society for Metallurgy and Materials, 4-7 October 2016, Bratislava, Slovakia, ISBN : 978-3-200-04786-0.*

F. Deirmina, M. Pellizzari

"Production and characterization of a tool steel-PSZ composite by mechanical alloying and spark plasma sintering", *J. Alloys Compd.*, vol. 709, pp. 742–751, Jun. 2017.

F. Deirmina, M.Pellizzari

"Production of HWTS (AISI H13) Matrix Composite Reinforced With Partially Stabilized Zirconia", *Proc. of the World PM 2016 Congress & Exhibition 9-13 October, Hamburg, Germany, ISBN: 978-1-899072-47-7.*

M. Pellizzari, F. Deirmina,

"POWDER METALLURGY OPENS NEW WAYS FOR TOOL STEELS," *(In press)*, International Journal of Microstructure and Materials Properties

Part 1

4.1 Harmonic structure design by low energy MM

Figure (1) shows SEM micrographs of the starting powders. The **AT** powder evidences the typical microstructure from rapid solidification, composed by primary martensite and retained austenite [71] (Figure 1a). Its hardness is rather high (712

HV0.05). Highly segregated areas can be detected in the intercellular regions. On the other hand, the annealed powders show carbide distribution mostly at prior intercellular regions, due to the local positive micro-segregation of carbide forming elements (Figure 1b). As a result of recrystallization, the hardness of the annealed powder is very low (190 HV0.05).

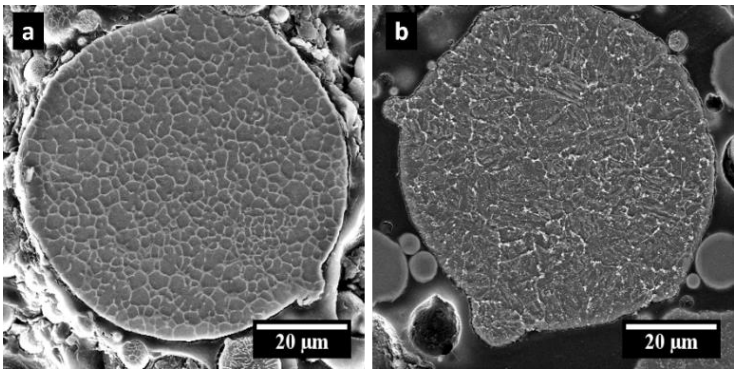

Figure IV-1. SEM micrographs of a) Gas Atomized (AT) powder and b) Annealed Powder (AN), (nital 5%)

Figure (2) shows the powders microstructure after 16 hours of mechanical milling. The hard (AT) particles show a visible deformed surface (Figure 2a) which can be recognized by the change in grain shape aspect ratio (i.e. prior austenite grain boundaries). The degree of straining gradually decreases towards the core. As a result of the lower hardness the (AN) particles (Figure 2b), experienced a much more severe surface plastic deformation.

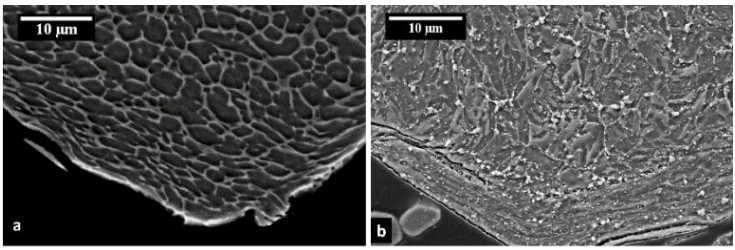

Figure IV-2. SEM micrographs showing the development of SHELL in a) (AT) and b) (AN) particles, (nital 5%)

Grain boundaries are difficult to be distinguished and the precipitated carbides, at the intercellular region, which act elastically against the impacts are forced to accumulate

and align tangentially to the surface of the (AN) particles (Figure 3). There also exists evidence of cracked carbides in the deformed matrix and voids that are initiated at the carbides and matrix interfaces. In both cases, the fraction of the microstructurally refined surface is about 10 vol. % of the entire particle.

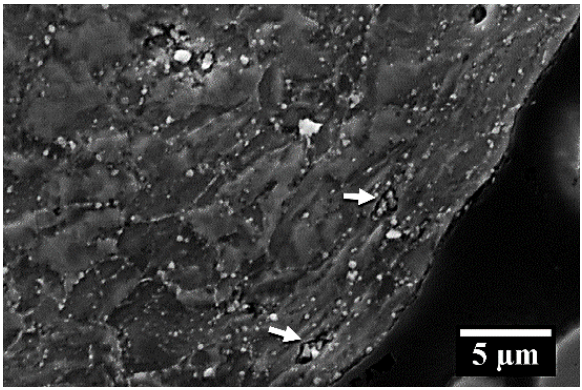

Figure IV-3. SEM micrograph showing the core/shell structure in (AN) powders, arrows indicating cracked carbides and generated void, (nital 5%)

XRD patterns of the four samples are shown in Figure (4), peak broadening is evidenced in both mechanically milled samples with respect to the un-milled ones. Moreover, It can be observed that γ (retained austenite) peaks are not present in collected spectra of AT sample milled for 16 h as an indicative of strain induced martensitic transformation in the shell area (Figure 4a). Since the penetration depth of Cu-Kα radiation in steel particles does not exceed more than a few microns [130], it is possible to assume that the collected data accounts for the severely deformed shell of (AT) and (AN) powders.

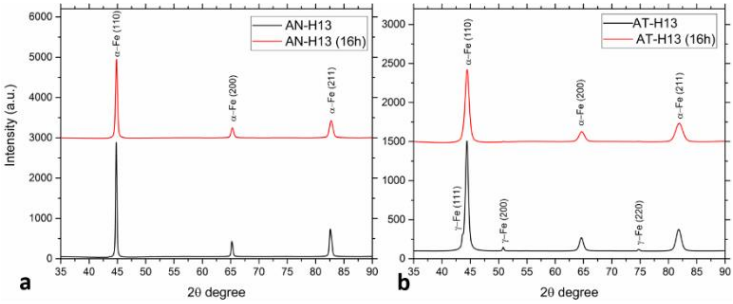

Figure IV-4. XRD patterns of a) AN and AN milled for 16 h, b) AT and AT milled for 16 h

The lattice microstrain vs. mean crystallite size of the samples are shown in Figure (5).

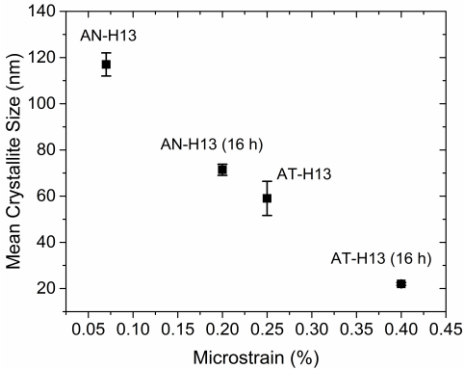

Figure IV-5. Lattice microstrain vs. mean crystallite size for all powder samples

The annealed powders show a drop in local strain and an increase in crystallite size as a result of dislocation recovery and grain growth; this becomes clearer when looking at the values obtained for rapidly solidified gas atomized powders. Samples which were subjected to mechanical milling, show microstructural refinement as the crystallite size is reduced compared to the un-milled counterparts. An increase in the lattice microstrain can be ascribed to the introduction of structural defects (e.g. dislocations) to the surface of the milled particles. The origin of microstrain will be discussed in more detail later in this work. The microhardness measurement results are depicted in Figure (6).

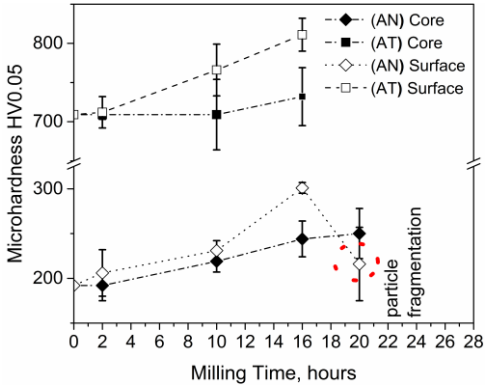

Figure IV-6. Microhardness evolution vs. milling time

The shell microhardness gradually increases by extending the milling time up to 16 h. As mentioned earlier, at this stage of milling, around 10 vol. % of the particles was severely deformed and microstructurally refined. By further extending the milling time, a drop in the shell micro-hardness is evidenced, in line with the SEM observations showing particle fragmentation after 20 h of mechanical milling (see Figure 7).

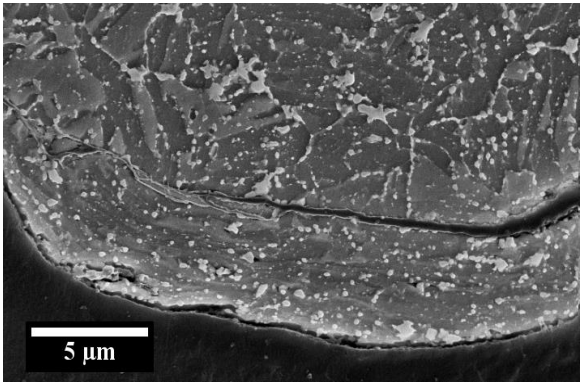

Figure IV-7. SEM micrograph showing the fragmentation after 20 h of milling in (AN) powders, (nital 5%)

The results thus suggest that in AISI H13 powder particles controlling the shell vol. % is rather hard or even impossible. To explain such behavior, one has to refer to the dislocation interactions in BCC structured materials. In a BCC structure material, the interaction of dislocations to generate a new dislocation with multiple Burgers vector of type <100> might nucleate a cleavage crack. However, there is strong evidence that the dislocations interaction cannot provide a stress concentration sufficient for a cleavage crack nucleation [131]. Therefore, the role of the carbides should also be taken into account [131]. As the surface of the particle is plastically deformed, at a certain level of strain hardening, a crack might nucleate in the carbides; the crack reaches the interface of carbide and strain hardened ferrite. Since strain hardened ferrite is not able to accommodate the plastic strain in the stress concentration site at the tip of the crack, the crack can be considered as a Griffith flaw. Therefore, once the length of these micro-cracks (i.e. cracking of coarse carbides or carbide films in the prior intercellular regions) reaches the critical length, because of the very slow velocity of dislocation movement in readily work hardened BCC ferrite [132], the crack will propagate by *cleavage* on the (001) plane. Another probability is to assume that the generated voids at the carbide/matrix interface acted as preferred sites for crack nucleation and subsequent cleavage fracture[133].

AT particles microstructure mainly consists of martensite showing higher initial microstrain and hardness due to the rapid solidification during gas atomization process. As a consequence, plastic deformation by MM will be more difficult, and the probability of early particle fragmentation is higher. Therefore, it was concluded that to develop a harmonic microstructure with controllable vol. % of UFG-shell, an alternative approach has to be applied.

4.2 Harmonic Microstructure design by high energy MM

4.2.1 Powder Characterization

Figures (8a) and (8b) show that mean particle size is significantly decreased after high energy MM. The microstructure of the heavily milled powders is shown in Figure (8d). MM destroyed the initial microstructure and segregated regions (see Figures 1a and 8c) were stretched to form a fine and closely packed lamellar microstructure. The lamellar spacing as an indicative of strain level is not completely uniform within the particles. The lamellar spacing is still detectable at the core of MM particles, whereas the outer and near surface areas show a much more refined microstructure probably because those regions experience more severe collisions compared to the core. The very initial stages of MM are characterized by particle fragmentation and severe plastic deformation. Continuation of milling will result in the cold welding of the fragmented particles together with a continuous increase of the level of strain hardening caused by severe plastic deformation. The process reaches a stationary stage when the rates of cold welding and fragmentation become equal. Cold welding of deformed particles may be responsible for the formation of micro and nanopores (Figure 8d) that are hard to be removed during consolidation. These porosities are reported to be one of the obstacles to the fabrication of fully dense UFG and NC materials[32]. Figure (9) clearly depicts that the particle size distribution has also become much narrower than that of the starting powders.

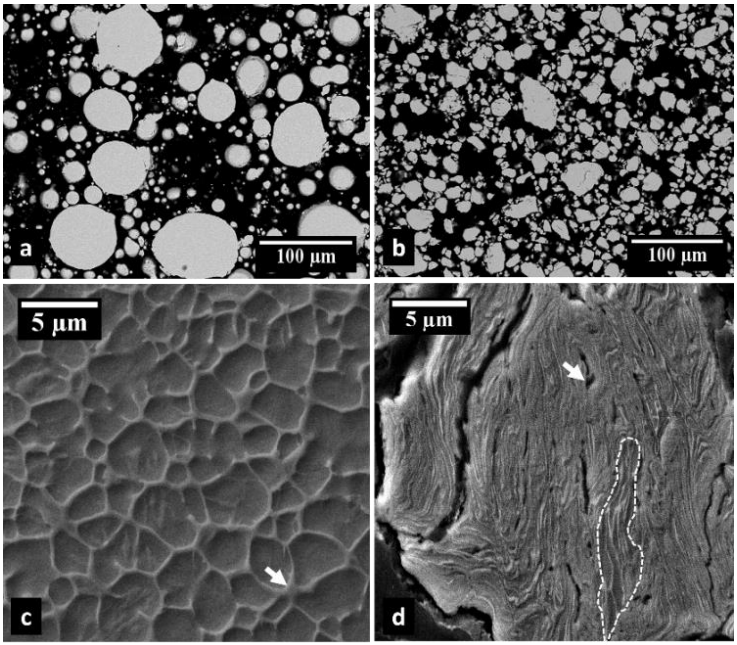

Figure IV-8. Morphology of a) gas atomized, b) mechanically milled powders (200min, BPR: 10:1.5 (g/g)), microstructures of c) gas atomized and d) mechanically milled powders. (SEM, nital 5%)

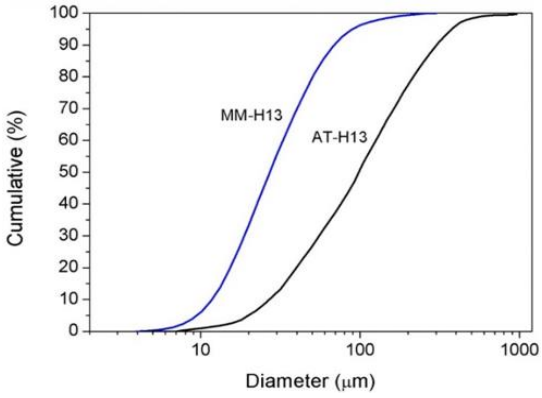

Figure IV-9. particle size distribution of AT and MM H13

The average microhardness is increased from 712 HV0.05 in atomized state to around 850 HV0.05 after heavy MM as a result of strain hardening and martensite substructure refinement (i.e. Hall-Petch relation) by severe plastic deformation[134]. As mentioned earlier, the absence of γ-Fe peaks in XRD spectra is a result of stress induced γ-α transformation.

The XRD spectra of MM powder is shown in Figure (10).

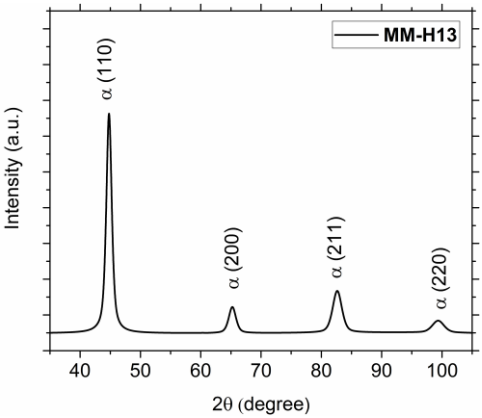

Figure IV-10. XRD pattern of MM-H13, please note peak broadening as compared with Figure (4b).

The quantitative XRD analysis results revealed that the mean crystallite size of the MM powders is refined to 16±6 nm and the lattice microstrain is increased to 0.5% (i.e. twice the rapidly solidified gas atomized particles reported in Figure 3). In MM powders two main strain fields are contributing to an increase in lattice micro-strain. One is around the dislocations (e.g. geometrically necessary dislocations) in the sub-grain boundaries (i.e. martensite laths), and the other one is at the grain boundaries (grain boundary layer) containing lattice defects and geometrically necessary dislocations to compensate for the misfit of neighboring grains [135]. When the powders are severely plastically deformed to refine the crystallite size down to less than 20 nm, the probability of finding dislocations within the grains approaches zero. Therefore, the only contribution to the rise in local strain arises from the grain boundary layer. Part of this microstrain will be released upon holding the powders at the sintering temperature (1100 °C) in response to dislocation recovery.

4.2.2 Spark plasma sintering

Figures (11a & b) depict the sintered microstructures of 0% MM (i.e. AT) and 100% MM respectively. The 100% MM shows a considerably finer grain size compared to the gas atomized counterpart, confirming that the fast Spark Plasma Sintering technique (30 min, 1100°C) allowed to retaining the structural modifications induced by MM.

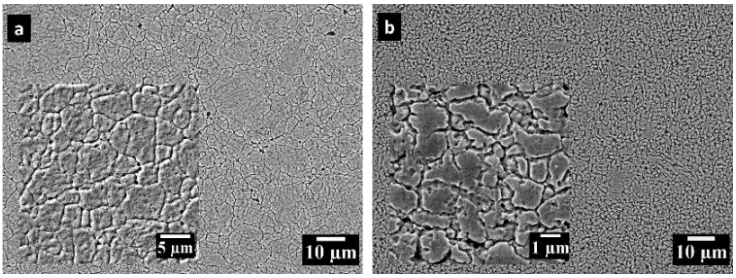

Figure IV-11. SEM (BSE) micrographs showing the microstructure of as sintered a) Atomized and b) 100% UFG-MM, (nital 5%)

The optical micrographs of sintered mixtures are shown in Figure (12). The micrographs revealed that a threshold of 50 vol. % UFG-MM particles should be overcome to achieve a 3D interconnected network of UFG-MM surrounding the CG (AT) particles. Otherwise, the UFG-MM will appear as isolated zones within the CG matrix. Therefore the 50 to 80% MM samples are referred to as “harmonic microstructures” while the 20 and 40% MM specimen are considered as “bimodal grained” microstructures.

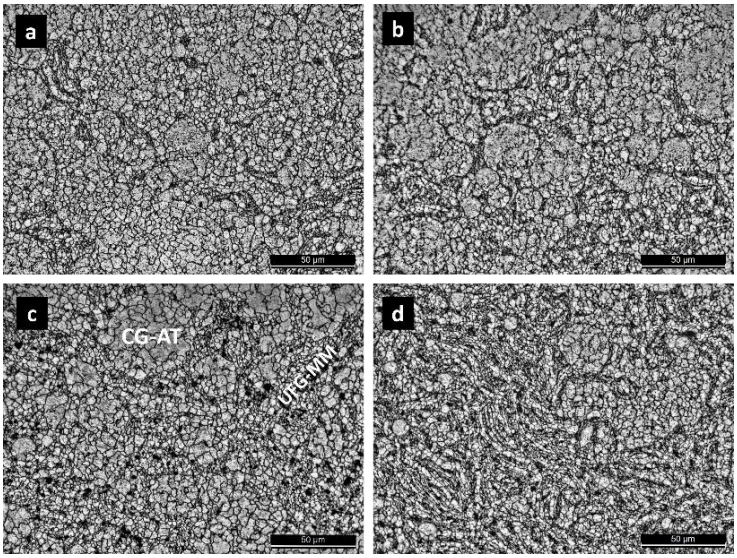

Figure IV-12. OM micrographs showing the microstructure of as sintered harmonic steels, a) 20%MM, b) 40 % MM, c) 60% MM and d) 80% MM (nital 5%)

The results of intercept length distribution are shown in Figure (13) and the corresponding average grain size is reported in Table 1. Mean grain diameter (i.e. prior austenite boundaries) for UFG-MM is 1.4±0.1 μm. 25% of grain size population is smaller than 1.0 μm and 75% of the population is finer than 1.8 μm. Whereas, the sintered AT particles show a mean grain diameter of 4.2±0.5 μm.

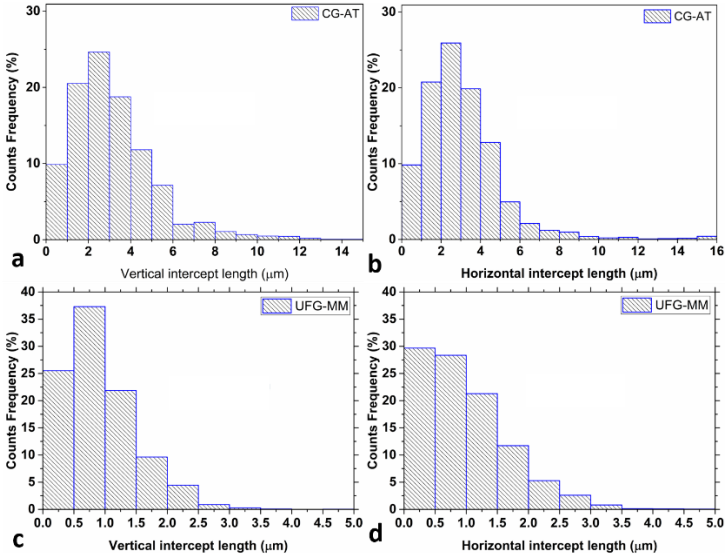

Figure IV-13. Results of grain size analysis by intercept method, a) vertical intercept length distribution for CG-AT zones b) horizontal intercept length distribution for CG-AT zones, c) vertical intercept length distribution for UFG-MM zones and d) horizontal intercept length distribution for UFG-MM zones

The grain aspect ratio defined by the ratio of horizontal intercept length to the vertical one is near 1 in both grain regimes. Both UFGs and CGs show a lognormal distribution and the null hypothesis for the lognormal distribution could not be rejected at a significance level of 0.05. The wide range of grain size distribution in UFG-MM zones can be explained by the random process of ball impacts on particles during MM which yields different particle sizes and grain sizes and is in line with the observations of non-uniform lamellar spacing formerly seen in Figure (8d). No sieving of the initial powders nor the milled powders makes it difficult to control the final grain size and homogeneity of the harmonic structure precisely, however, from an industrial perspective, this processing route seems to be the simplest and the most economical route.

Table IV-1 Grain Size ASTM E-112-96 Mean of Vertical and Horizontal Lines

Measuring Zone	**No. of grains (mm^{-2})**	**Avg. Grain area (μm^2)**	**Avg. Grain diameter (μm)**	**No. intercept (mm^{-1})**	**Mean linear intercept line (μm)**	**ASTM grain size No.**
UFG	530000	1.9	1.4	815	1.2	15.8
CG	59000	17	4.2	270	3.7	12.8

The presence of upper bainite and retained austenite (RA) is evidenced mostly in the UFG zones (see Figure 14).

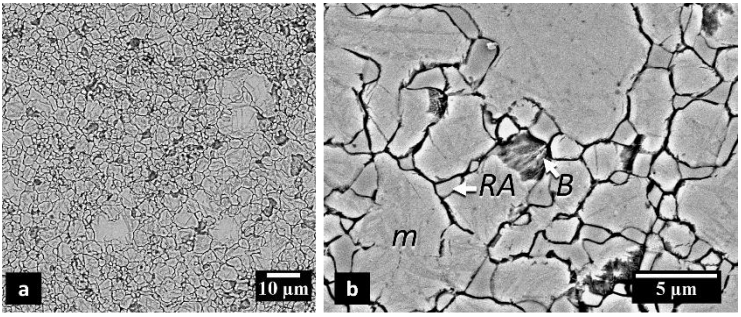

Figure IV-14. a) SEM (BSE) micrograph of 50% MM microstructure showing bainite in UFG-MM zones (dark areas) and b) a higher magnification SEM (BSE) micrograph highlighting the presence of upper bainite and retained austenite

Upon free SPS cooling (i.e. relatively low cooling rates), Austenite (γ) decomposition into bainite begins at the grain boundaries[136]. Therefore the higher grain boundary vol. % in UFG-MM promotes the formation of bainite by increasing the preferential nucleation sites. As it is highlighted in Figure (14), RA is evidenced in UFGs with a grain diameter less than 1 μm. It is widely accepted that austenite grain size reduction increases the stability of austenite, thus hindering the martensitic transformation[137,138].However, due to low vol. % of RA, this phase could not be quantified by XRD analysis. Since free cooling could not provide a fully martensitic microstructure, further quench and tempering of the samples will be necessary.

4.2.3 Density and hardness of the SPS samples

Figure (15) depicts the density and hardness measurements after SPS. Near full density samples were produced (see Figure 15a). A gradual decrease in relative density is observed by increasing the MM vol. %. On one side, MM powders possess a higher surface energy leading to higher driving force for sintering. However, on the other hand, this high surface energy is associated with a strong strain hardening of particles, showing very limited compressibility. As a consequence, neck formation and extension during SPS will become more difficult, thus hindering the sintering process.

All blends also show a negative deviation from the linear "rule of mixtures" calculated by Eq. 1.

$$\rho_C = f \times \rho_{MM} + (1 - f) \times \rho_{AT} \quad (1)$$

where f is the volume fraction of MM and ρ is the relative density. AT (i.e. 0%MM) and 100%-MM densities were considered as the reference values.

As it is shown in Figure 15(b), the hardness assumes a general increase by increasing the MM vol. %. Experimental measurements show a systematic negative deviation with respect to the theoretical values obtained by the rule of mixtures. This deviation can be tailored and justified by the same deviation observed in density measurements.

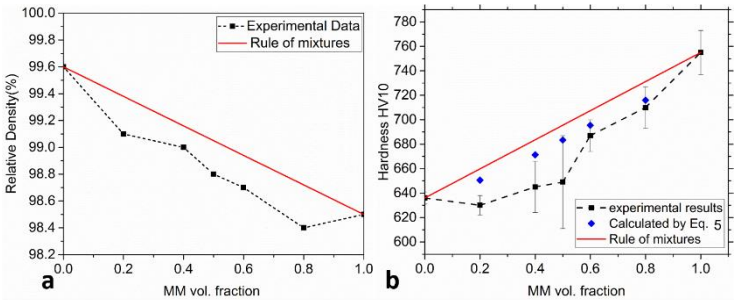

Figure IV-15. a) Relative density vs. MM volume fraction, b) average Hardness of sintered specimen vs. MM volume fraction (the straight lines show predicted quantities by the rule of mixtures)

There exist many experimental evidences that Young's modulus is negatively affected by porosity content in polycrystalline materials [5]. A widely accepted empirical relation is proposed by Sanders et al. [139]

$$E = E_0 exp(-bP) \quad (2)$$

Where E is the reduced modulus, E_0 being the fully dense bulk modulus, b is a parameter equal to 5.03 in a material with the nearly similar Young's modulus to H13 steel [140] and P is the porosity.

The Vickers indentation impression is a result of elastic-plastic deformation in a fully dense material. However, in a material containing porosity, pore closure by the indentation stress also contributes to the indentation impression. It is widely accepted that by increasing the porosity, hardness decreases. The extent of porosity closure is proportional to the level of stress induced by the indentation in bulk. By assuming an elastic deformation, the strain ε ($\varepsilon_{11}+ \varepsilon_{22}+ \varepsilon_{33}$) is linearly related to the stress σ ($\sigma_{11}+ \sigma_{22}+ \sigma_{33}$) by the elastic modulus.

$$\frac{\sigma}{3E} = \varepsilon \tag{3}$$

Hence it is convenient to roughly conclude that, the observed decrease in hardness is linearly proportional to a decrease in Young's modulus of the porous material.

$$\frac{H}{H_0} = k\frac{E}{E_0} \tag{4}$$

where k is a constant and is reported to be very close or equal to 1[140]. Therefore, combining (2) and (4), the relation between hardness and porosity is quantified as follows:

$$\frac{H}{H_0} = exp(-5.03\Delta P) \tag{5}$$

Taking the theoretical hardness calculated by the "rule of mixtures" as the reference hardness (H_0) for each sample, and ΔP as the porosity content difference of the experimental density measurements with that predicted by the mixtures rule, the predicted hardness (H) influenced by the porosity, somehow approaches the experimental results (see Figure 15b).

In addition to the effect of porosity, the non-uniformly distributed MM particles in 40% MM and 50% MM might account for the high scatters observed in hardness measurements. It means that whether indenting on a surface with the larger volume fraction of fine grains than the nominal mixed value, the hardness shifts towards higher levels and vice versa. However, referring to Eq.6, the radius of the plastic zone ($C_{p,}$) under the Vickers indenter is roughly around 350 μm as depicted in Figure (16). Looking at the micrographs in Figure (12) and taking the average diameter of AT and MM powders (i.e. 100 μm and 30 μm respectively) into account, makes it possible to postulate that the *average hardness* is statistically accounting for the bulk (i.e. average microstructure). This is schematically shown in Figure (16).

$$C_p = \sqrt{\frac{3P}{2\pi\sigma_y}} \tag{6}$$

Where P is the applied load (100 N, HV10), and σ_y is the yield stress of the material[141].

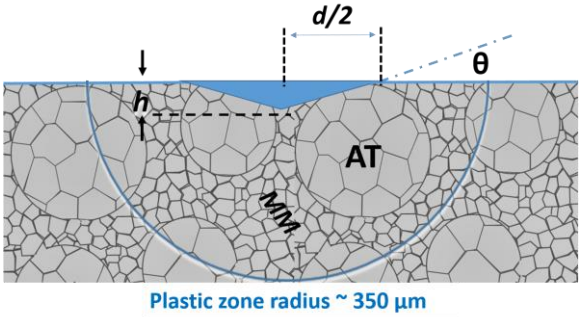

Figure IV-16. A schematic of the extent of plastic zone under Vickers indenter, d is the diagonal of residual impression of indentation which varies in between of 160 to 170 µm in the present experiment

4.2.4 Grain growth and recrystallization

In MM particles a closed pack lamellar spacing was observed. After SPS, the grains show a nearly equiaxed morphology that confirms the occurrence of recovery, recrystallization and limited grain growth during sintering. Both these effects are responsible for a part of hardness drop after sintering.

It is assumed that the Vickers indentation on powders is not affected by the porosity. The effect of "sintered sample" porosity (i.e. 1.4%) on the hardness can be elaborated using Eq. 5. The result suggests that, by neglecting the influence of porosity, the hardness should be around 810 HV10 in the as-sintered state. Therefore, the observed difference in hardness (i.e. 810 HV10 vs. 850 HV10 in MM powder) might be related strain relief and grain growth. XRD analysis results on the SPS sample confirmed that the mean crystallite size of the sintered 100% UFG-MM (i.e. 24±4 nm) is increased compared to the as-milled state (i.e. 16±6 nm). Around 40 HV10 drop in hardness is thus a consequence of the limited crystallite grain growth and follows the widely accepted Hall-Petch relation on the linear proportionality of strength (hardness) to the reciprocal square route of grain size. The relation also holds for martensite packets and α-Fe crystallite size in a microstructure which shows grains with random crystallographic orientations [134].

4.2.5 Heat treatment

Figures (17a) and (17b) show the microstructure of quenched and tempered CG-AT and UFG-MM zones in " harmonic structured " specimens, respectively. The CG zones show coarser carbides. A number of these carbides are in the form of films precipitated preferentially on the prior austenite boundaries. On the other side, The UFG-MM zones show a finer microstructure and a more homogenous distribution of very fine secondary carbides. One explanation is that the increased dislocation density in UFG-MM opposes the energy barriers to carbide precipitation and provides a larger number of nucleation sites[142,143].

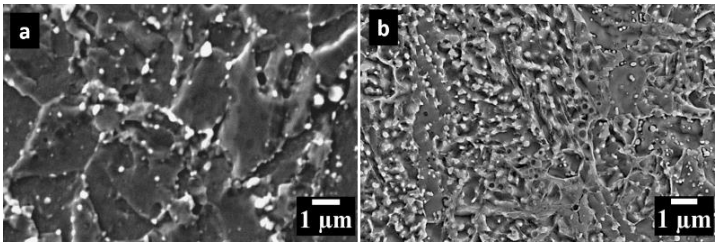

Figure IV-17. SEM (SE) micrographs of heat treated microstructure a) CG-AT regions and b) UFG-MM areas

The hardness of the heat-treated samples follows the same trend observed in as-sintered specimens while more conforming to the mixture rule (Figure 18a). The reciprocal square root of mean grain size of each specimen corrected by the statistical weight of fine and coarse grains according to the initial mixing volume fractions is plotted against hardness. The trend is more or less conforming to the Hall-Petch theoretical relation for hardness dependency on grain size (Eq. 7). The harmonic microstructures (i.e. 50 to 80% MM) show a slight positive deviation from the linear fit. The validity of the relationship is frequently reported for ultrafine grained materials down to a mean crystallite size of 20 nm. [134,144]

$$H = H_0 + K_H[(1 - V_{MM})d_{AT}^{-\frac{1}{2}} + (V_{MM})d_{MM}^{-\frac{1}{2}}] \quad (7)$$

where H is the hardness, H_0 being constant, K_H is the strengthening factor derived from the hardness measurements, and V_{MM} is the volume fraction of UFG-MM.

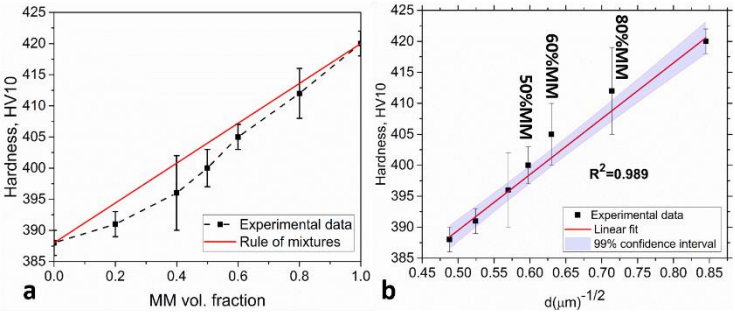

Figure IV-18. a) Average hardness vs. the volume fraction of mechanically milled powder b) Average hardness vs. d (μm)$^{-1/2}$

4.2.6 Spherical indentation

Figure (19a) plots the reconstructed stress-strain curves from the indentation curves for 5 samples, namely 0% (i.e. AT), 20%, 50%, 60% and 100% UFG-MM. Figure (19b) displays the tensile true stress-true strain curves for 0% MM and 100% MM.

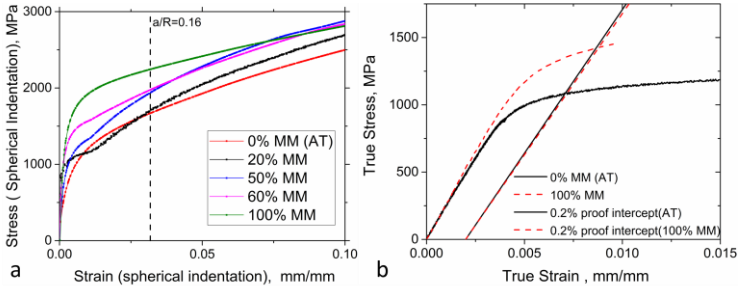

Figure IV-19. a) Stress-strain curves reconstructed from spherical indentation curves for the five samples and b) uniaxial tensile test true stress-true strain curves for 0% MM (AT) and 100% MM

Table 2 lists the 0.2% proof yield strength of the mono-size grain samples (i.e. 0%MM and 100%MM) together with the yield strength results obtained from spherical indentation. There is a good agreement between the values obtained from tensile tests and those of the spherical indentation. Moreover, results show a substantial increase in the yield strength of the samples by increasing the UFG-MM volume fraction.

Table IV-2. 0.2% proof yield strength of the specimen

Sample	YS (MPa) (Tensile Test)	YS (MPa) (Indentation)
0%MM	1053±6	1064±30
20%MM	-	1081±37
50%MM	-	1203±36
60%MM	-	1233±40
100%MM	1387±10	1375 ±42

A general negative deviation from the rule of mixtures is also evidenced by the yield strength results (Figure 20).

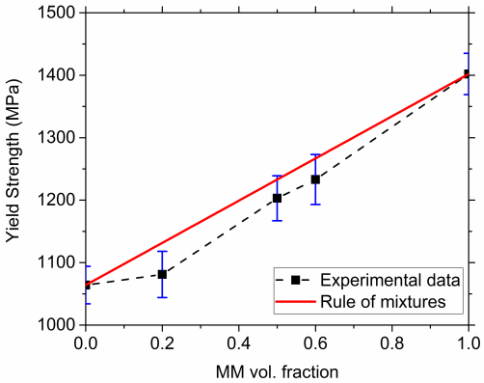

Figure IV-20. Yield strength vs. MM volume fraction

Apart from the influence of porosity on the yield strength of the samples, it would be more convenient to elaborate on the strengthening contribution of UFG-MM in heat treated samples by taking the Hall-Petch strengthening into account. Lesuer et al. [145] proposed that the yield strength for a mechanically milled dispersion strengthened iron can be written as:

$$\sigma_y = \sigma_0 + \sigma_g + \sigma_p \quad (8)$$

Where σ_o is the friction stress representing the overall resistance of the crystal lattice to dislocation movement, σ_g is grain boundary strengthening which also includes the martensite sub-structure strengthening, and σ_p is particle strengthening. For the moment, it is assumed that strain hardening contribution (σ_d) caused by mechanical milling as the other significant contributing factor to the strength of the *quenched* or *as-sintered* AISI H13, can be neglected for the *"heat treated"* samples. Since the

samples under investigation are tempered above the secondary hardening peak (i.e. at 625°C), this assumption is more than plausible. An explanation is that upon the isothermal holding of AISI H13 at temperatures above the secondary hardening peak, the dislocation recovery rapidly takes place irrespective of the initial micro-strain [146]. However, the initial dislocation density induced by severe plastic deformation during MM may increase the number of carbide nucleation sites as described previously, (see Figure 17) thus decreasing the carbides size and carbides spacing.

Considering (AT) as the reference specimen, it is possible to rewrite the equation for the rest of the samples as follows;

$$\sigma_y - \sigma_y^{AT} = \Delta\sigma_y = \Delta\sigma_g + \Delta\sigma_p \quad (9)$$

σ_g is the contribution of grain refinement and can be considered analogous to Eq. 7 but with a different value of K', while σ_p is the contribution of strengthening by particles and can be written as :

$$\sigma_p = K''\lambda_s^{-1/2} \quad (10)$$

where *K"* is a constant and λ_s is the carbide (particle) spacing which is derived from:

$$\lambda_s = 1.5^{1/2}\left[\left(\frac{\pi}{4f_v}\right)^{\frac{1}{2}} - 1\right]d_p \quad (11)$$

where f_v is the vol. Fraction and d_p is the average diameter of carbides. According to the quantitative image analysis the vol. % of carbides in the samples were estimated to be around 11.5, the average diameter of carbides (irrespective of the carbide type) was estimated to be around 90 nm for (AT) and 60 nm for the 100% MM sample. The value of *K"* is approximated to be 395 MPa $\mu m^{1/2}$ for iron [145]. Therefore, it is possible to estimate the strengthening contribution of fine carbides in harmonic microstructure and then to evaluate the contribution of grain refinement. Table 3 lists the $\Delta\sigma_p$ for the samples.

Table IV-3. Contribution of particle strengthening to the yield strength of the specimen considering 0% MM (AT) as the reference, d_p is corrected by the statistical weight of fine and coarse grains according to the initial mixing volume fractions

Sample	d_p (nm)	$\Delta\sigma_p$ (MPa)
0%MM (AT)	90	0
20%MM	84	32.8
50%MM	75	89.3
60%MM	72	110.4
100%MM	60	210.2

Figure (21) shows the contribution of distinct strengthening mechanisms in harmonic microstructures.

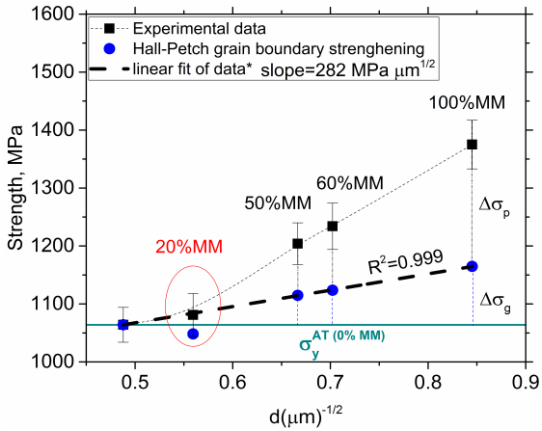

Figure IV-21. A comparison between experimental yield strength vs. individual strengthening mechanisms (please note that the fitted line excludes 20% MM data point)

The particle strengthening effect increases by increasing the UFG-MM vol. % as a result of reduced interparticle (carbide) spacing. Moreover, except from the 20% MM sample, which did not show a 3D interconnected network of UFG, the grain refinement strengthening is obeying the Hall-Petch relation. Disregarding the 20%MM sample, the slope (i.e. Hall-Petch slope) of the linear fit of data (dashed line) becomes around 282 MPa $\mu m^{1/2}$, very near to that reported in the literature for pure iron and steel (i.e. varying between 260 to 310 MPa $\mu m^{1/2}$)[145,147]. A similar trend is also reported for bimodally grained Iron and SUS 316L steel with harmonic microstructural design [148,149]. It is mandatory to note that in both grain size regimes,

the very fine secondary carbides that are not detectable by SEM are not considered in the above calculations.

4.2.7 Fracture Toughness

The apparent fracture toughness (K_{app}) is decreasing by increasing the volume fraction of harder MM particles (Figure 22). The Ka of AT-H13 is 61.5 MPa $m^{1/2}$ while that of 100%MM is 36 MPa $m^{1/2}$.

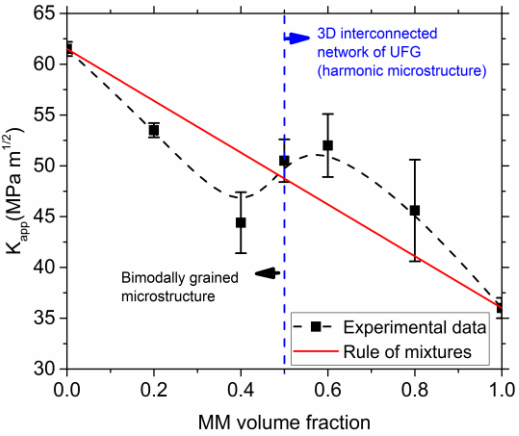

Figure IV-22. Fracture toughness (K_{app}) of the samples vs. volume fraction of UFG-MM (straight line shows the predicted values by rule of mixture)

20%MM shows a slightly lower fracture toughness with respect to that predicted by the " *rule of mixtures*." The sample showed a very similar hardness and yield strength as compared with the 0%MM (AT) but a lower relative density. The 40%MM shows a drastic decrease in fracture toughness with highly scattered values. An inhomogeneous distribution of UFG MM around the CG matrix results in highly scattered K_{app} values for bimodal grain sized materials [100]. As mentioned earlier, 40%MM does not show an interconnected network of fine grains due to the insufficient volume fraction of MM to fully surround AT particles (i.e. forming a 3D interconnected network). The confinement of isolated coarse grain zones by UFG is a prerequisite for enhancement of ductility and improved work hardening in bimodal grained metals by providing the condition for the development of strain gradients imposed by the microstructure[150,151]. This can somehow be extended to the toughness. Therefore, in the absence of an interconnected network, it is probable that the increased vol. % of hard isolated UFG-MM particles that act as energetically

preferential sites for crack propagation is responsible for this drop. Indeed, 50% to 80%MM samples (i.e. harmonic microstructures) and especially 60%MM show a positive deviation from the rule of mixtures. It was previously stated that there is a negative deviation from the mixtures rule for hardness and yield strength of these samples (Figures 18a and 20) attributable, at least in part, to porosity. Knowing that porosity plays a deleterious effect on the fracture toughness by providing local stress concentration, a general negative deviation should have been witnessed for the K_{app} values. Moreover, reduced carbide spacing in UFG-MM regions is well-documented to have a negative influence on toughness by providing a higher number of energetically preferred sites for crack propagation or in other words, decreasing the material resistance to crack propagation[152]. Therefore, despite the validity limits of the linear "mixtures rule" in predicting a complex fracture behavior, this systematic deviation might be related to a toughening mechanism induced by the harmonic microstructure.

The fracture surfaces and the crack propagation paths are depicted in Figures (23 & 24) and (25), respectively. As it is shown in Figure (23a), limited ductile fracture near the notch region is evidenced for the 0%MM (AT) sample. The rest of the fracture surface is characterized by interparticle fracture and a few cleavage facets. The interparticle fracture might be explained by the presence of surface oxides that hindered a full consolidation (i.e. development of strong metallic bondings between the particles) despite a nearly complete densification (Figure 15). The surface of the as-received gas atomized AISI H13 contains a mixed oxide layer on the surface consisted of a thin and homogeneous iron oxide layer (~7 nm thick) and isolated oxide particles rich in chromium, manganese, silicon and vanadium [65,66]. The elimination of these oxides requires high vacuum annealing up to 900°C which introduces a very expensive additional step to the production. Moreover, in spite of a careful protection (storage in glow box), the oxidation of the surface cannot be easily avoided while handling these highly reactive powders to the SPS unit.

The interparticle fracture might increase the apparent fracture toughness by promoting the crack path deflection [44]. This type of fracture, as shown in Figure (23d) is characterized by the presence of localized dimples as an indicative of sintering neck failure. The 20 and 40%MM samples also show an inter-particle fracture mechanism (Figures 23b and 23c). The islands of hard UFG-MM particles seem to anticipate the failure acting as defects inside the AT matrix. The presence of isolated UFG regions on the fracture path can be appreciated from Figure (25a).

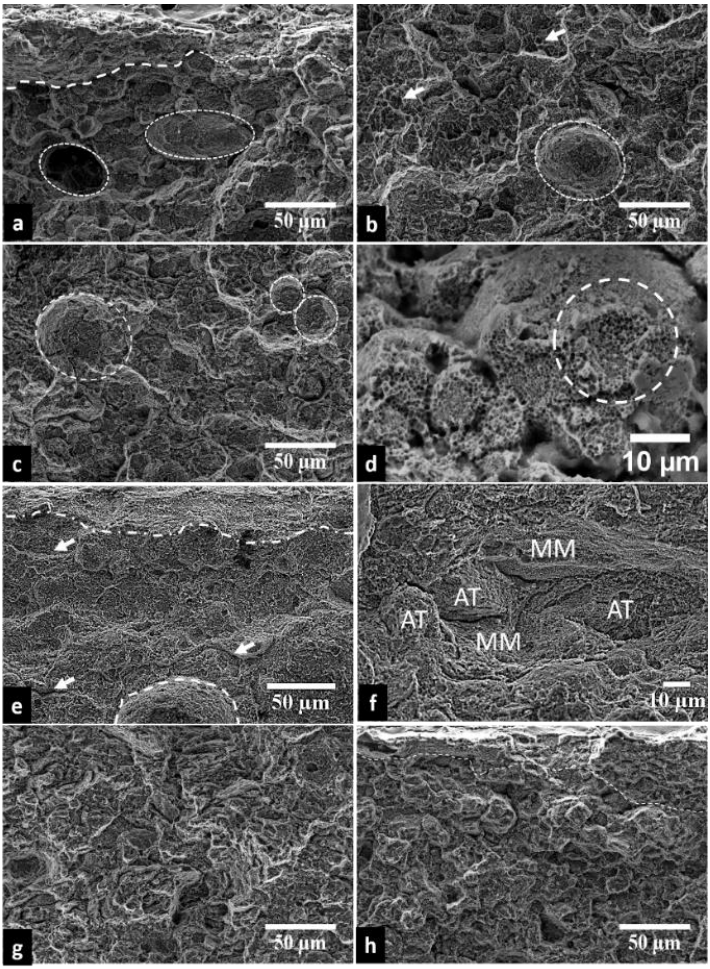

Figure IV-23. Fracture surface of a) 0%MM (AT), b) 20%MM (arrows indicating cleavage facets), c) 40%MM, d) sintering neck failure in 0%MM,e) 60% MM,f) higher magnification of 60%MM (arrows showing delaminations), g) 80%MM and h) 100% MM (in all micrographs the dashed lines are representing the boundary of near notch regions and the rest of the fracture surface, and dashed circles represent the AT particles)

In 50 to 80% UFG-MM samples, the inter-particle fracture can be observed. Moreover, the fracture surface is characterized by a few cleavage facets and plenty of very fine dimples (see Figure 24). Cleavage facets are in the range of 5 µm or

less, which can be related to the fracture of CG-AT particles. Dimples are the result of microvoid initiation at the fine secondary carbides precipitated on grain boundaries of UFG-MM (see the rugged crack propagation path in Figures (25b) and (25c)[25]. The fracture surface of 100%MM is also characterized by very fine dimples and limited cleavage facets.

The most peculiar aspect of the fracture in 50 to 80%MM samples is the presence of an extended number of decohesions at the interfaces of MM-AT or MM-MM particles. The origin of this type of interparticle decohesion might be explained by the presence of the 3D interconnected network of UFG-MM. Upon straining, a local strain mismatch build-up appears at the interface of CG-AT regions and the UFG-MM network. BCC structured UFGs are highly susceptible to the localized deformation because of the small number of dislocations inside the ultrafine grains and also reduced strain rate sensitivity[153,154]. to compensate for the strain mismatch, decohesion simultaneously occurs at the interfaces of (CG-AT) / (UFG-MM) and also at the interfaces of UFG-MM particles[155]. Some of these decohesions nearly lie in the planes perpendicular to the plane of the main crack (Figure 23f). Therefore, those might change the stress state by decreasing the stress triaxiality in front of the original crack [25] leading to higher stress to extend the original crack front. This interpretation plausibly justifies the positive deviation of apparent fracture toughness in harmonic microstructures. The presence of interparticle decohesion is evidenced in the near-notch region in the 60% MM sample (Figure 25b).

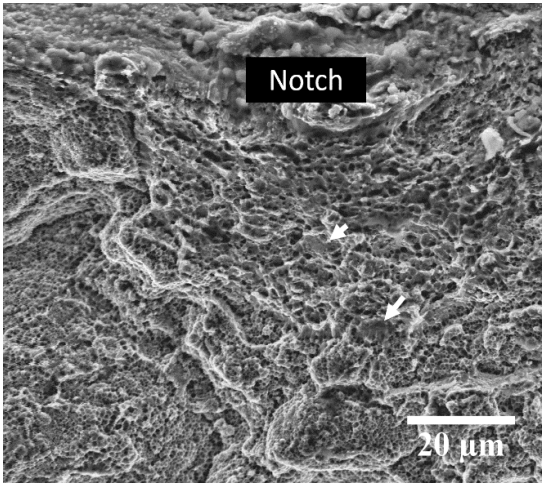

Figure IV-24 a closer view of near notch fracture surface in harmonic microstructure showing dimples and a few cleavage facets indicated by arrows

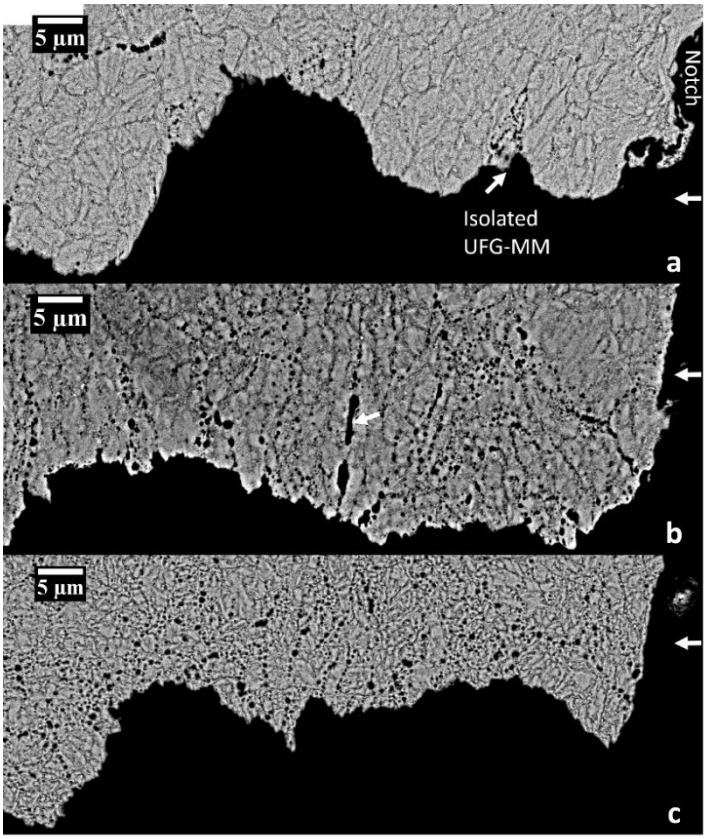

Figure IV-25 crack propagation path, a) 20% MM, b)60% MM, arrow is showing the decohesion and c) 80% MM (horizontal arrows are addressing the notch)

From mechanical properties viewpoint, the 60%MM sample (hereinafter referred to as harmonic sample (HS)) shows the optimum combination of strength and fracture toughness. The properties of this sample are in good agreement with the observations of Zheng et al. [148] which reported that optimized mechanical properties in steel with harmonic microstructure are achieved by the contribution of 50 to 60 vol.% ultrafine grains. It is noteworthy mentioning that the average CG size in their work was about 2 µm whereas the UFG grains were in the range of 0.7 µm.

4.2.8 Thermal Fatigue resistance of the Harmonic Microstructure

The optimized combination of hardness and fracture toughness in the bimodal harmonic structure are very promising looking at improved resistance to heat checking. Thermal fatigue resistance of the HS can be of interest in its potential industrial application where the tool has to show a combination of high toughness and reasonable hot strength and hardness together with high TF resistance.

4.2.8.1 Microstructure of HS sample used for TF test

The microstructure of the as sintered HS is shown in Figure (26). As stated earlier in the experimental part, the *soft milling of the mixed (UFG-MM and CG-AT) powders* for 1 hour improves the uniformity of the microstructure compared to the sintered bulk from the *mixed powders*. The as sintered and heat treated hardness of the 100%MM, HS and 0%MM (AT) disks were the same as the previously tested samples (Figures 15 and 18) while the standard deviation was considerably reduced in the case of HS (i.e. 680±8 and 408±2 in as sintered and tempered condition respectively).

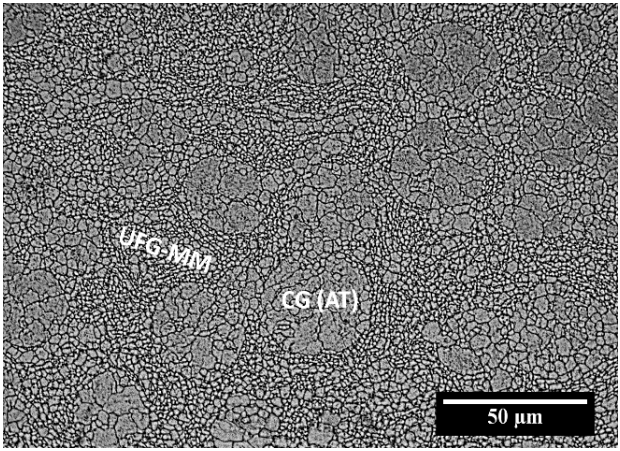

Figure IV-26 Optical micrograph of as-SPS HS produced for TF testing; please note the more homogeneous AT-AT spacing compared to Figure (12c)

4.2.8.2 TF test results

Figure (27) shows the TF damage of the samples after 200 and 500 cycles. The 0% MM (AT) (Figures 27 a,d) is clearly showing thicker heat checks which may be held

representative of deeper crack penetration. On the other hand, 100%MM (Figures 27 c,f) with an UFG microstructure is indicating a finer heat checking network. HS (Figures 27 b,e) evidences an intermediate behavior, showing an average crack width lower than AT, but higher than 100% MM.

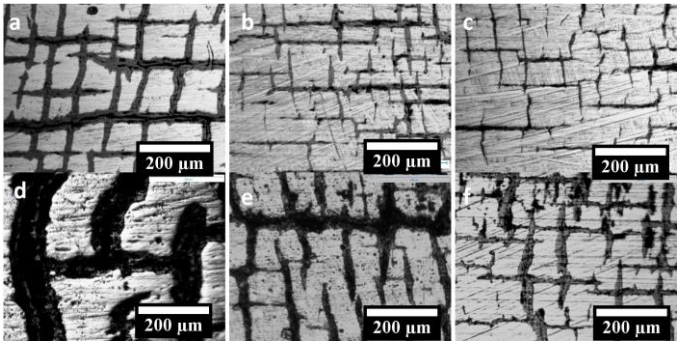

Figure IV-27. TF damage after 200 cycles a) 0% MM (AT) b) HS, c) 100% MM and after 500 cycles d) 0% MM (AT), e) HS and f) 100% MM

The mean crack length (l_m), maximum crack length (l_{max}), crack density (ρ) and the pyrocracking factor *P* after 500 cycles are reported in Figure (28). 0%MM (AT) shows a mean crack length exceeding 100 μm while the HS and 100% MM samples are showing values lower than 50 μm. 0%MM (AT) sample also shows the highest maximum crack length, confirming the faster propagation rate in this material. On the other hand, crack density is considerably higher for 100%MM evidencing the highest nucleation rate in that sample. 100%MM shows an ultrafine grain microstructure containing very fine secondary carbides. Carbides act elastically against thermomechanical stresses during TF testing and are considered as preferential sites for TF crack nucleation. Given the reduced carbide spacing in this material, higher crack nucleation rate thus higher crack density can be expected. HS seems to combine the best properties of the other two materials, namely the low mean crack length of MM and the low crack density thanks to the contribution of 40%vol. AT particles. The overall damage highlighted by pyrocracking factor P of 0%MM (AT) is approximately three times higher than the other two samples which show very similar P parameter while the lowest value belongs to HS. Looking at the cross-sectional view of TF damage in Figure (29), the deeper cracking in 0% MM (AT) is clearly confirmed.

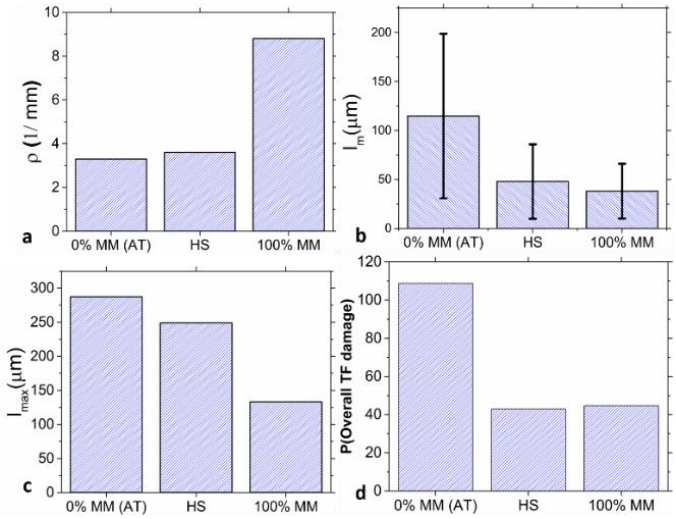

Figure IV-28 a) Mean crack length, b) Maximum crack length, c) Crack density and d) pyrocracking factor P measured after 500 TF cycles

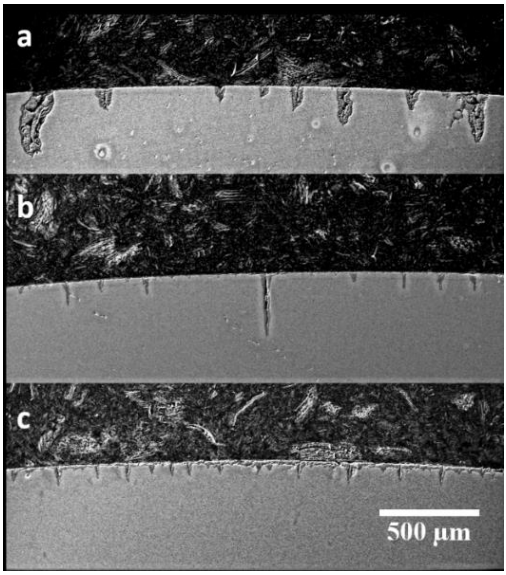

Figure IV-29. SEM micrographs of perpendicular plane to damaged surface of a) 0% MM (AT), b) HS and c) 100% MM

The heavy internal oxidation of cracks let to assume the contribution of oxide-induced propagation mechanisms[156]. The cracks are very open in this sample suggesting a considerably high plastic strain. On the other hand, 100%MM sample shows very short and sharp cracks, whereas HS shows a bimodal cracking which is responsible for an increase in l_m and l_{max} parameters compared to the 100%MM. The three-dimensional constraint for the (AT) regions by the harder UFGs is responsible for the absence of very open cracks in HS.

Figure (30a) depicts the microhardness profile after 500 cycles, normalized by the initial micro-hardness of each sample, measured in a central position of the TF specimen. A thermomechanically affected zone exists in all three samples. The depth of this region is about 2.5 mm for the coarse-grained 0% MM (AT) and around 1 mm for the HS and ultrafine-grained 100% MM. Moreover, the hardness drops to 0.7 initial value near the damaged surface for AT. The situation is different for 100% MM and HS that show a lower drop in hardness near the "damaged surface." The observations in Figure (29) and the microhardness results suggest that 0%MM (AT) is affected by *thermal* and *plastic strain induced softening* [108] more than the two other samples in the first hundreds of cycles of TF testing. Another important understanding from the hardness profiles is that the depth of the softening region is larger than the longest cracks observed in all 3 three samples. This observation conveys the fact that under the current testing condition (T= 660°C), the resistance to the TF cracking is mainly controlled by the hot strength and resistance to thermal softening rather than the toughness of the material [107,157]. Resistance to thermal softening can be directly linked to tempering resistance of the steel. The tempering curves at 650°C (i.e. near to the TF test temperature) for 0%MM (AT) and 100%MM are shown in Figure (30b).

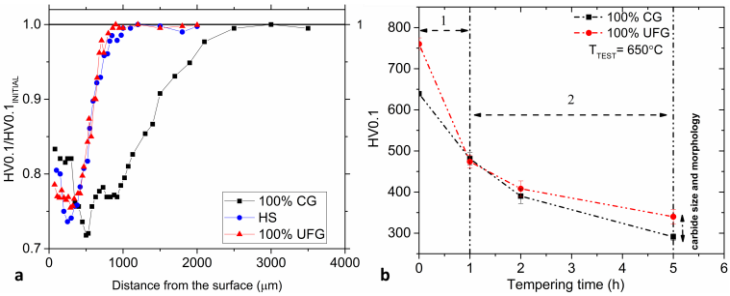

Figure IV-30 a) Microhardness profiles (surface to core) after 500 cycles of TF test and b) tempering resistance curves for 100% MM and 0% MM (AT)

After just 1 hour of tempering (Stage 1), the hardness is identical for both samples. A condition which conveys that hardness drop in 100%MM (H_{SPS}= 755 HV10) occurs at a higher rate compared to the 0%MM (AT) (H_{SPS}= 636 HV10). For longer isothermal holding intervals (stage 2), 100%MM shows a higher tempering resistance compared to the AT counterpart.

The sudden drop in hardness for 100%MM at stage 1 is in agreement with the stress relieving of the severely deformed UFG-MM microstructure at the tempering temperature. However, after prolonged soaking, the over-tempering is retarded in this sample in comparison with the (AT) counterpart. Such behavior is formerly reported for the AISI H13 tool steel isothermally hold at temperatures above the secondary hardening peak (i.e. 580°C) [107]. At these temperatures, the hardness drops drastically in the very early stages of isothermal holding irrespective to the initial microstrain (i.e. dislocation density and other structural defects) due to the fast dislocation recovery of the substructure interior (i.e. martensite lath)[146]. By extending the tempering time, the crucial parameter to determine the tempering resistance is the *precipitated carbides* type, morphology, distribution, and size. The finer and more homogenously dispersed carbides the higher the resistance to thermal softening. Therefore, the presence of finer secondary carbides in 100%MM corresponds to a better tempering resistance [158]. The contribution of 60 vol. % ultrafine grains forming an interconnected network in HS thus can be expected to increase the tempering resistance of this sample as well.

4.2.8.3 TF crack interaction with the harmonic microstructure

The interaction of the strain field in front of a TF crack with the harmonic microstructure is shown in Figures (31) and (32).

From the metallographic cross-sectional in Figure 29 and theoretical background on the mechanical properties of the UFG materials discussed earlier, it is convenient to postulate that most of the TF cracks in HS have been initiated in the UFG zones. The cracks inside the UFG-MM areas are sharp and propagate along the grain boundaries. As soon as the crack approach an AT particle, it is arrested (Figure 31a), and its propagation is retarded by crack-tip blunting as shown in Figure (31b). Crack tip blunting occurs because of the presence of relatively large grains at the tip of the propagating crack that accommodate a higher number of emitted dislocations without hindering the motion of the other dislocations. When more dislocations are emitted inside the coarse grains (i.e. at higher levels of thermomechanical stresses arising from heating and cooling cycles), the local strain mismatch between the CG and UFG will lead to the crack propagation by the decohesion of the UFG/CG interface. So that crack deflects through these interfaces (see Figures 32a-c) [155]. Therefore,

crack blunting and crack deflection as extrinsic toughening mechanisms are operative in HS thanks to the harmonic microstructural design.

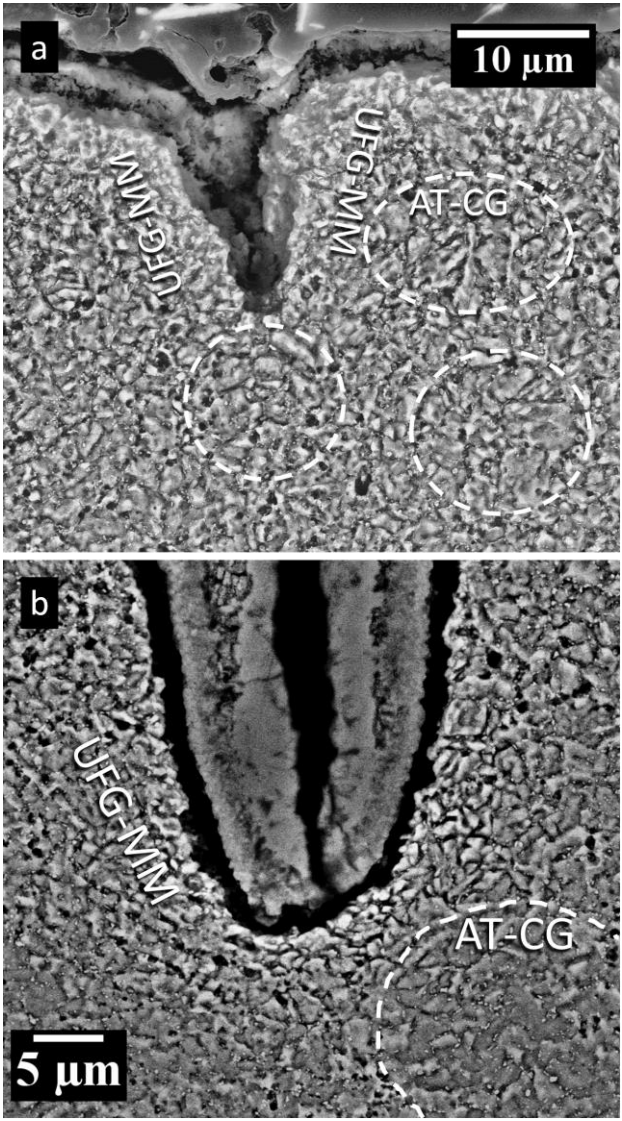

Figure IV-31. a) TF crack arrest and b) crack blunting at the vicinity of AT particles

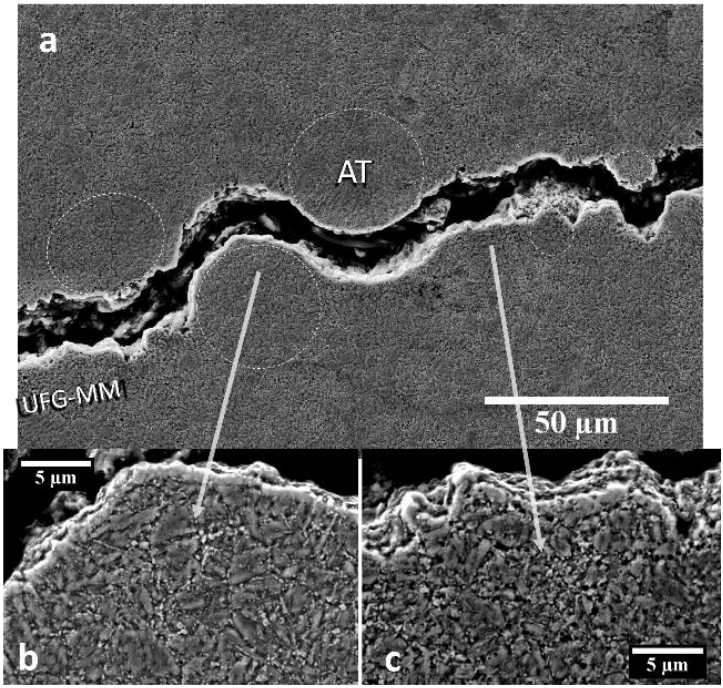

Figure IV-32. a) crack deflection along UFG/CG interface, b)closer view of CG AT particle and c) closer view of UFG-MM zone

To further validate the hypothesis supporting the development of a local strain mismatch between the UFG and CG zone, the strain hardening rates obtained from the spherical indentation test for 100%MM, HS and 0%MM is depicted in Figure (33). Even if these results are obtained at room temperature, those can be used as a qualitative comparison between strain hardening capacity of the UFG-H13 and CG-H13.

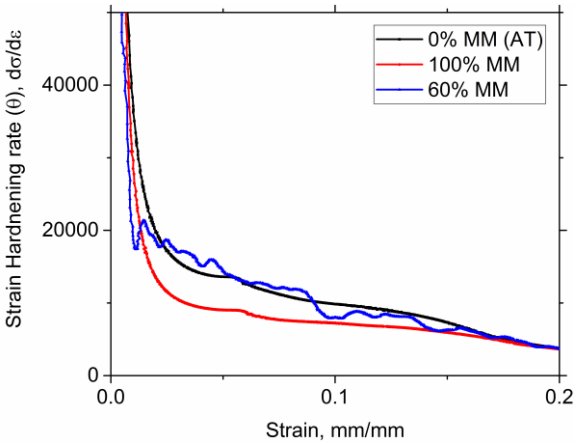

Figure IV-33. Strain hardening rates obtained from spherical indentation test

The pronounced difference between the hardening rates of these two materials up to ~ 15% plastic strain may reinforce the assumption above. It is also evident that the HS shows a transitional hardening rate expect for the early plastic strain regime where it shows higher strain hardening than the AT samples. In this strain regime, due to the presence of a high strength 3D interconnected UFG network it is probable that the tightly constrained CGs have undergone more intense strain hardening. Since the UFGs and CGs are not equally easy to deform under the spherical indentation, the confined coarse grains experience complex strain paths and triaxial strain components with large *plastic strain gradients*[96]. Therefore, according to the strain-gradient theory [159], this gradient plastic deformation of a length scale of ~10 μm or more (see the spacing between CGs in Figure 26) results in *extra strain hardening* due to the storage of large number of *geometrically necessary dislocations* near the interfaces of UFGs and CGs which are essentially present to accommodate the *plastic strain gradient*. In addition to the direct strengthening effect of the accumulated dislocations, because of the existence of dislocation density gradients, these dislocations generate long-range stresses impeding dislocation motion in regions far from the interface and cause additional hardening [99]. This behavior has been documented in a number of bimodal grain size, harmonic microstructure and also metals with dispersed nano-domains [99]. Upon further straining, as it appears at an equivalent strain of 15%, where the coarse grains (both in HS and AT samples) have accumulated a large number of dislocations, all 3 samples show a similar hardening behavior.

Conclusions of part 1

- Novel tool steels showing bimodal grain size were fabricated by spark plasma sintering of as atomized and mechanically milled particles. MM significantly refined the grain size and introduced a remarkable strain hardening which promotes a hardness increase in as sintered specimen. A harmonic microstructure, given by a 3D interconnected network of fine-grains surrounding coarse-grained atomized particles, was achieved by the addition of 50-80% MM powder.
- It was shown that in in the case of BCC structured materials, an easier control of the volume fractions of UFG/CG can be achieved by mixing and/or low energy mechanical milling of the desired vol. % of the MM-UFG particles with the as-atomized-CG powders
- The hardness of steel increased by increasing the vol. fraction of MM powder. Despite the bimodal grain size distribution in Harmonic microstructures, both hardness and yield strength obey the Hall-Petch relationship.
- The harmonic microstructure shows enhanced strain hardening compared to the both mono-size grain (i.e. CG and UFG) under spherical indentation due to the generation of geometrically necessary dislocation as a result of plastic strain gradient imposed by the microstructure.
- The fracture toughness decreased by increasing the vol. % of MM powder. A toughening effect was evidenced for the samples essentially showing harmonic microstructure. Toughening is interpreted to be the result of the deviatory effect of coarse-grained atomized particles together with energy dissipation by interparticle fracture at the CG/UFG or UFG/UFG interfaces leading to a local drop of the driving force for the crack propagation.
- Looking at TF test results, the harmonic microstructure combined the beneficial effects of both of its constituents, i.e., the low nucleation rate of 0%MM (AT)-H13 and the low propagation rate of 100% MM-H13 and showed the lowest pyrocracking factor. The harmonic microstructure shows two extrinsic toughening mechanisms, namely crack blunting and crack deviation along the interfaces between CG and UFG-MM particles.

Part 2

4.3 Fabrication of the Tool Steel-PSZ composite

4.3.1 Powder Characterization

Figure (34a) depicts the AISI H13 as-received powders (AT). The H13 particles show the typical spherical morphology characteristic produced by the gas atomization process. 3Y-PSZ and Mg-PSZ powders are shown in Figures (34b) and (34c) respectively. Ceramic particles are mostly agglomerated in both batches.

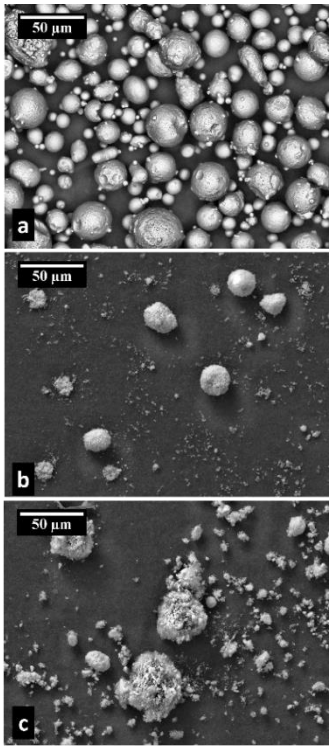

Figure IV-34. SEM micrographs showing the morphology of starting powders, a) AISI H13, b) 3Y-PSZ and c) Mg-PSZ powders

Figure (35) shows the morphology and cross-sectional view of the powders collected after various intervals of mechanical alloying. After 90 min, (Figure 35a), ball milling

destroyed the initial spherical morphology of AISI H13 and flattened the powders. The particle size is increased compared to the starting powder also due to cold welding caused by the intense collisions with the balls and the vial. The flat morphology suggests that the milling process has not reached the stationary state yet [12]. After 200 min the particles show an equiaxed morphology and a quite narrow size distribution. Moreover, a significant particle size reduction is evidenced (Figure 35b). After 340 min of MA (Figure 35c) no substantial changes regarding particle size and morphology was observed. Therefore, it is convenient to assume that the steady state has been reached after 200 min.

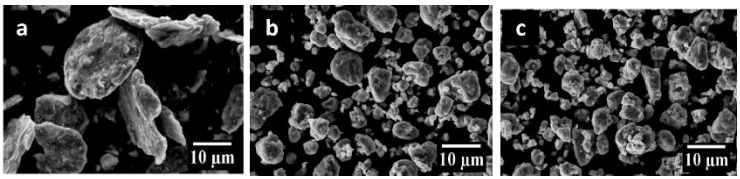

Figure IV-35. SEM micrographs of MA (H13+20 vol. % 3Y-PSZ) powders, a) SE image of MA, 90 min, b) SE image of MA, 200 min, c) SE image of MA, 340 min

As it is shown in Figures (36a) and (36b), after 90 min, the surface of the H13 particles is covered with PSZ agglomerates (brighter particles in BSE micrograph), confirming that a homogenous dispersion of PSZ particles into the matrix is not achieved. More importantly, the limited local deformability because of the presence of a hard shell of PSZ suggests that densification will be hindered during SPS. Even if the driving force for sintering in severe plastically deformed steel particles (see the steel microstructure in Figure (36b) is increased given the increased dislocation density and other structural defects, PSZ agglomerates impede the steel particles contact during sintering thus leading to a weak metallic bonding and consolidation. Furthermore, the lower specific surface area of the flattened particles partly counteracts the positive effect of the intense deformation on increasing the driving force for sintering. It is noteworthy to remark that for all four powders batches, the vol. % and (d_{SP}/d_{HP}) nearly satisfied the percolation or aggregation of PSZ particles[75,78]. Therefore the extension of milling time was necessary to bypass the aggregation or percolation threshold[82]. After 200 min (Figure 36c), the distribution of PSZ inside the matrix became more homogenous. Most particles were occluded in lamellas of severely deformed steel particles. The number of remained PSZ particles on the surface is very limited. That is further confirmed by looking at the cross-sectional view of the polished and etched MA particles in Figure (36d), showing a severely deformed microstructure characterized by ultrafine lamellas. An unalloyed, yet severely deformed, isolated H13 can be identified in the same figure. In Figures

(36c) and (36d), some micro-pores and nano-cracks appear at the conjunctions of the cold welded particles. These porosities might be retained after SPS of the MA powders and are reported to be one of the serious drawbacks to the production of fully dense nano-sized grain and UFG bulk via PM processing routes [160].

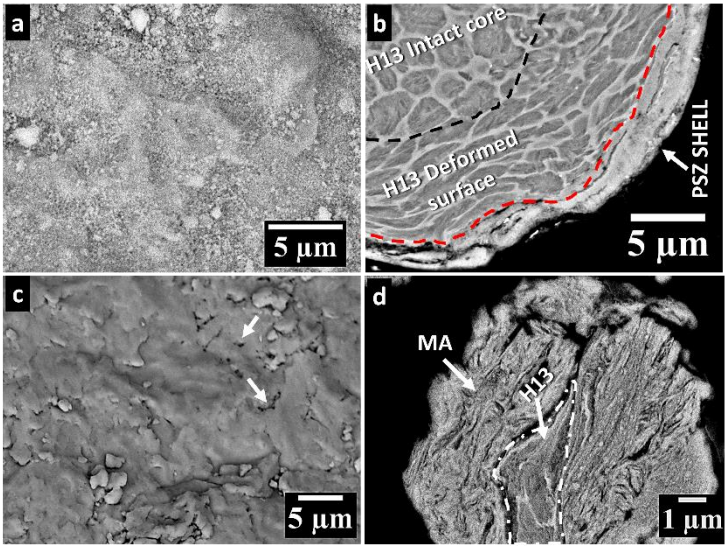

Figure IV-36. BSE image of MA (H13 + 20 vol. % 3Y-PSZ) powders a) after 90 min (powder surface, brighter particles are Zirconia, b) metallographic cross-section of MA powders, 90 min, c) BSE image of the powder after 200 min (brighter particles are Zirconia), please follow the arrow to see micro-pores, and d) metallographic cross-section of MA powders, 200 min

As shown in Figure (37), EDS elemental mapping on the cross section of the carefully polished MA powders confirmed the achievement of a nearly homogenous distribution of PSZ in the H13 matrix.

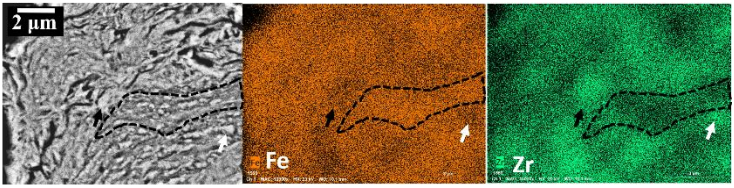

Figure IV-37. EDS elemental mapping on MA powder (20 vol. % Mg-PSZ), the dashed area shows a region with less concentration of PSZ and arrows are addressing to PSZ particles (PSZ particles appear brighter in BSE micrograph)

Figure (38) shows the particle size distribution of the starting AISI H13 powders and the mechanically alloyed powders for 200 and 340 min. Looking at the data of 200 min of MA, the size distribution has not been subjected to considerable change after 340 min. Therefore, 200 min was selected as the optimum milling time in this work.

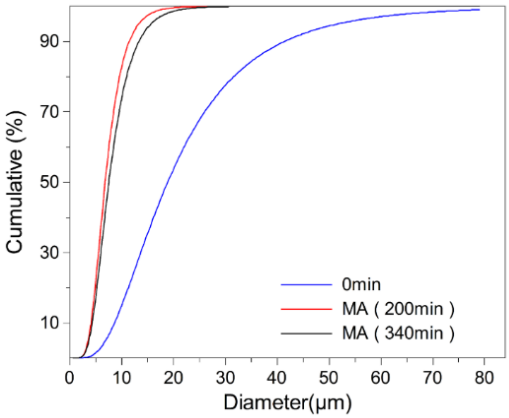

Figure IV-38. Particle size distribution of AT AISI H13 powders, MA (200min) and MA (340min)

The average microhardness of MA powders was higher than 1000 HV0.01 after 200min of milling, however no meaningful distinction between 10 vol. % and 20 vol. % reinforcement could be appreciated due to the very high scatter of the micro-hardness measurements which might be related to the very fine size of the powders, existing un-alloyed H13 areas and presence of microporosity previously shown in Figure 36. The AT powders microhardness was similar to that reported in section 4.1, and the average microhardness of mechanically milled H13 powders (MM-H13) powders was slightly higher than that reported in section 4.2.1 (i.e. 870 HV0.05).

Quantitative analysis results and XRD patterns and are shown in Table 4 and Figure (39) respectively.

Table IV-4. XRD quantitative results for powders

Sample	α-Fe	γ-Fe	t-ZrO_2	m-ZrO_2	c-ZrO_2	α-Fe crystallite size (nm)	α-Fe microstrain (%)
3Y-PSZ	0	0	64	28	8	N/A	N/A
Mg-PSZ	0	0	24	72	4	N/A	N/A
AT	94	6	0	0	0	40	0.2
MM	100	0	0	0	0	16	0.5
MA (H13+20%3Y-PSZ)	90	0	5.7*	4.3	*	12	0.6
MA (H13+20%Mg-PSZ)	91	0	3.6*	5.4	*	18	0.5

* In MA powders the vol. % of c-ZrO_2 could not be discriminated from that of t-ZrO_2. The cumulative vol. % of both phases is reported.

Figures (39a) and (39c) show the XRD patterns related to As-received (unmilled) 3Y-PSZ that contains 64 and 8 vol. % of tetragonal (t-ZrO_2) and cubic (c-ZrO_2) zirconia, respectively. Figures (39b) and (39d) depict the patterns of unmilled Mg-PSZ powders containing 24 and 4 vol. % t-ZrO_2 and c-ZrO_2 respectively. As it is illustrated in Figures (39e) and (39f), unlike the Atomized powders (AT), the MM-H13 and MA samples do not show peaks pertaining to austenite, as discussed earlier, γ to α strain induced transformation has been taken place during ball milling process. A slight peak shift to higher angles in MA samples is evidenced that might be related to an increase in point defects after mechanical milling. Peak shift might also occur because of the contamination during mechanical milling. However, as the balls were in steel, this hypothesis seems to be less plausible. Because of peak broadening, extreme peak overlapping, and low vol. % of PSZ, it was not possible to achieve a reliable distinction between t-ZrO_2 and c-ZrO_2 peaks in composite powders.

The (H13+3Y-PSZ) powders that contained higher initial vol. % of t-ZrO_2 show a relative reduction of (t+c) phase after MA (i.e. 57% vs. 72% in the starting powder). To explain this change, one should take the mean crystallite size of t-ZrO_2 in the as-received state (i.e. 46 nm) into the account. Assuming a log normal distrubtion for t-ZrO_2 crystallites size and by knowing that the stress induced transformation of *t* to *m* mainly involves tetragonal crystallites larger than 30 nm or crystallites with low stabilizer content [161], It can be deduced that the partial stress induced transformation of t-ZrO_2 crystallites to m-ZrO_2 during high energy milling is plausible [162,163].

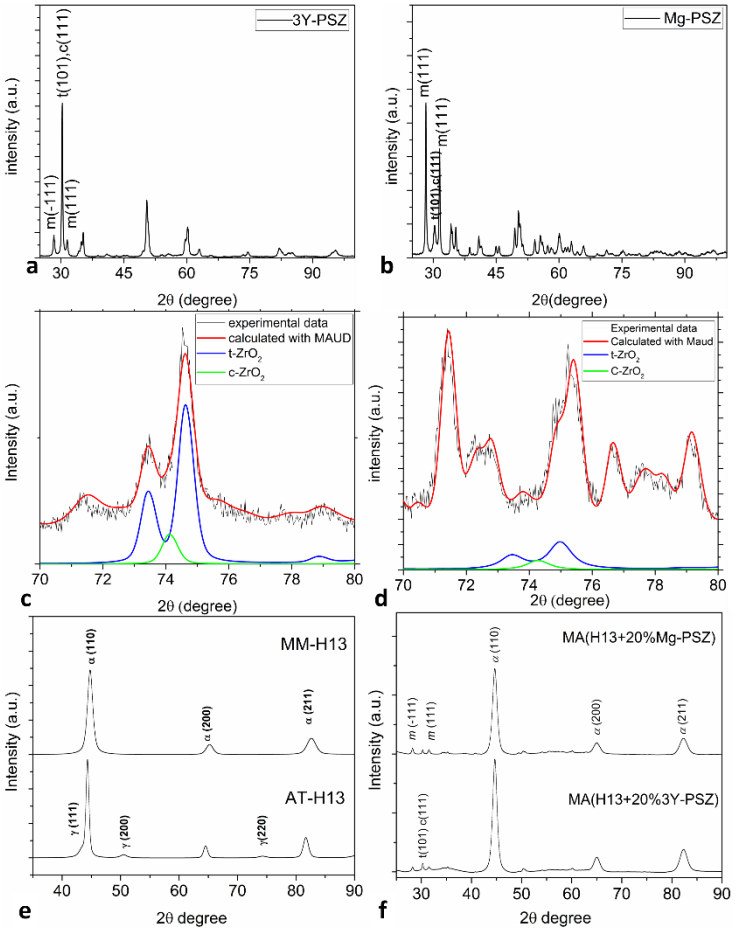

Figure IV-39. XRD patterns of a) 3Y-PSZ (unmilled), b) Mg-PSZ (unmilled), c) elaboration on c-ZrO_2 and t-ZrO_2 vol. % in 3Y-PSZ, d) elaboration on c-ZrO_2 and t-ZrO_2 vol. % in Mg-PSZ, e) unreinforced powders (i.e. MM and AT) and f) composite (MA) powders milled for 200 min

In the case of coarser Mg-PSZ powders with a large monoclinic phase content (i.e. 72 vol. %) in the as-received state, the vol. % of (t+c) phases is increased after MA (40% vs. 28% in the starting powder). The mean crystallite size of the t-ZrO_2 in as-received Mg-PSZ powders was calculated to be 16 nm. Therefore, in this system, the t-m stress induced transformation requires higher energy or longer milling time compared to the 3Y-PSZ reinforced composite powders [162]. On the other hand, even

without the addition of a stabilizer, m-ZrO_2 can be transformed to cubic and tetragonal phase by high energy ball milling. This transformation is a consequence of the significant crystallite size reduction *and/or* distortion of the monoclinic lattice because of the high-energy impacts during the ball milling process [164,165]. Moreover, in the presence of a stabilizer (i.e. MgO), the formation of solid solution is favored by high energy mechanical milling [166]. Probably, the same mechanisms are operative in composite powders containing Mg-PSZ and are responsible for *m-t* transformation during MA. It has to be noted that the mean crystallite size of the monoclinic phase in the unmilled Mg-PSZ powders was about 53 nm while this value reduced to around 21 nm after high energy milling.

PSZ does not show its nominal mixing volume fraction (i.e. 20 vol. %). Lower than expected zirconia volume fraction can be explained by the absorption contrast effects in XRD analysis due to the much bigger size of steel particles than that of the dispersed PSZ [167]. This assumption can be justified by looking at the XRD patterns of powders milled for 90 min (Figure 40) showing that the volume fraction of zirconia in samples *milled for 90 min* is overestimated (i.e. 29 vol.%).

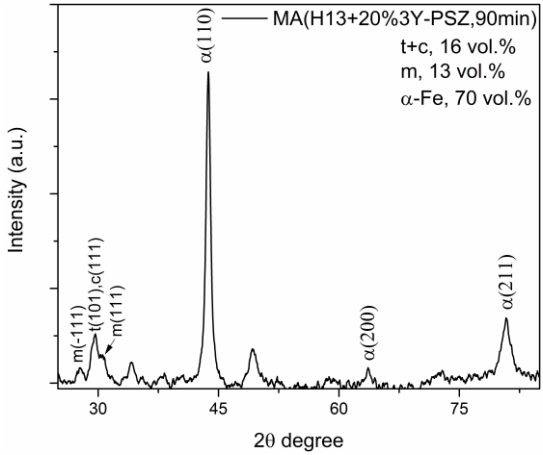

Figure IV-40. XRD pattern and vol. % of phases after 90 min MA, please note the overestimated vol. % of PSZ

Overestimation stems from the accumulation of PSZ on the surface of the powders with a thickness of about 4 µm (see Figure 36b). Whereas, for the *200 min milled powders*, in which most of the PSZ particles are trapped within the ductile matrix lamellas (see Figure 36d), the vol. % of PSZ is underestimated.

4.3.2 Spark Plasma Sintering

Figure (41a) depicts the lower punch displacement registered during sintering of MA powders. The curves qualitatively describe the samples densification. Upon applying the uniaxial pressure, the start of punch displacement nearly appears after 400s [573°C]. In this stage the steep linear increase is caused by the plastic deformation of the particles, the harder the particles, the lower the slope. This can be better appreciated when looking at the displacement, and the first derivative of displacement curves of softer AT-H13 in Figure (41b). The next stage begins immediately as the maximum uniaxial pressure (i.e. 60 MPa) is achieved, after almost 500s and the samples are being heated up to the sintering temperature. This stage is characterized by a slight decrease in the densification rate due to the ferrite to austenite transformation in AISI H13 steel (Ac_1 ~840°C) [168]. The final stage of consolidation is characterized by the achievement of a plateau for the punch displacement in Mg-PSZ reinforced composites.

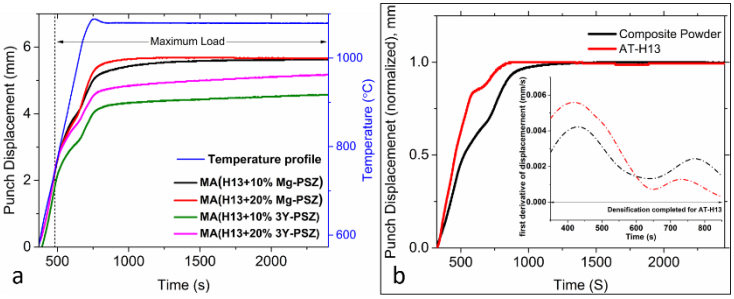

Figure IV-41. Sintering curves of a) composites and b) a comparison of sintering behavior of AT-H13 and the composites with regard to punch displacement and its first derivative

In the case of the 3Y-PSZ reinforced composites, the curves still maintain a slight positive slope confirming that complete densification is not achieved. This result can be explained in the light of the very fine particle size of the starting 3Y-PSZ particles. Accordingly, the $d_{H13}/d_{3Y\text{-}PSZ}$ particle size ratio is much smaller compared to the Mg-PSZ composite and hard zirconia particles may completely cover the H13 ones, thus hindering densification and also the diffusion processes promoting sintering. The incomplete densification of 3Y-PSZ composites will be confirmed by the aid of density measurements reported in the next section of this work.

4.4 Characterization of the tool steel-PSZ composites

4.4.1 Microstructure, hardness, and density

The micrographs of the as-sintered samples are shown in Figure (42).

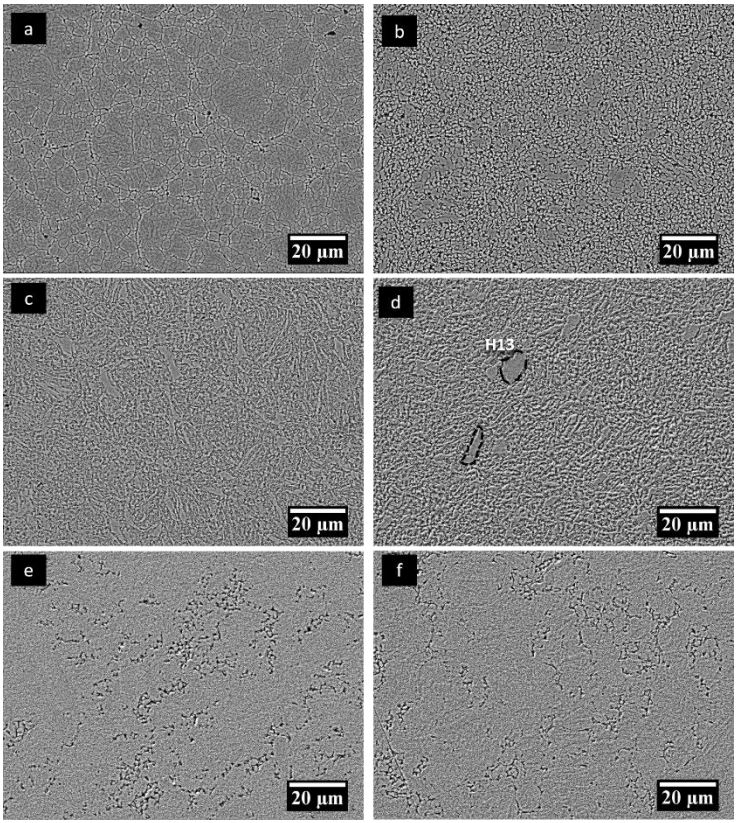

Figure IV-42. SEM micrographs of as-sintered microstructure of a) AT-H13, b) MM-H13, c) MA(H13 +10%Mg-PSZ), d) MA(H13 +20% Mg-PSZ) the dashed areas are unalloyed H13, e) MA(H13 +10%3Y-PSZ), Please note the inter-particle porosities and f) MA(H13 +20% 3Y-PSZ), Please note the inter-particle porosities

The AT-H13 (Figure 41a) shows an average grain size of nearly 5 µm, the same of the sintered sample previously described in section 4.2. The MM-H13 sample shows an ultrafine grained (UFG) microstructure with a mean grain size of 1.3 µm (Figure

42b). As it is depicted in (Figures 42c to 42f), composites also evidence an UFG microstructure. Over 80 vol. % of the bulk demonstrates the achievement of a successful PSZ dispersion while the rest of the microstructure consists of isolated unalloyed H13 areas similar to those in the milled powders (Figure 36d). In 3Y-PSZ reinforced samples, the presence of porosities at the particles interface is evidenced confirming the former deduction regarding the incomplete densification of this material. A higher magnification micrograph of the composite microstructure reveals the presence of fine PSZ particles dispersed in the matrix (Figures 43a and b).

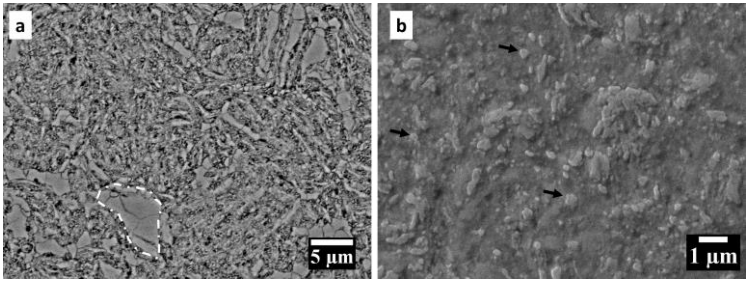

Figure IV-43. a) BSE-SEM micrograph of the 20 vol. % Mg-PSZ reinforced composite, dashed area is an unalloyed H13, and the brighter spots inside the composite area are PSZ particles and b) a higher magnification SE micrograph showing a good bonding between dispersed PSZ particles and the matrix (some PSZ particles are pointed by the arrows)

XRD patterns of the as-SPS samples, shown in Figure (44), confirm the stability of the t-ZrO_2 and c-ZrO_2 in the composites thanks to the short time, fast sintering. The t-m transformation is reported to occur at a critical grain size of t-zirconia [169–171] or due to the formation of spinel or Mg-rich silicates at the matrix-reinforcement interface leading to the destabilization of the t-zirconia [172]. Present XRD results seem to exclude both possibilities. The mean crystallite size of α-Fe in AT-H13 is approximated to be 40 nm while this value for the MM-H13 and the composites is in the range of 25 nm. For the heavily milled powders recrystallization during sintering is generally easier than that of as-received powders because of the large excess free energy. Therefore, in order to preserve the refined microstructure, short time low-temperature consolidation techniques appear to be necessary. As mentioned earlier, consolidation by SPS lead to a very limited grain growth in composites and MM-H13.

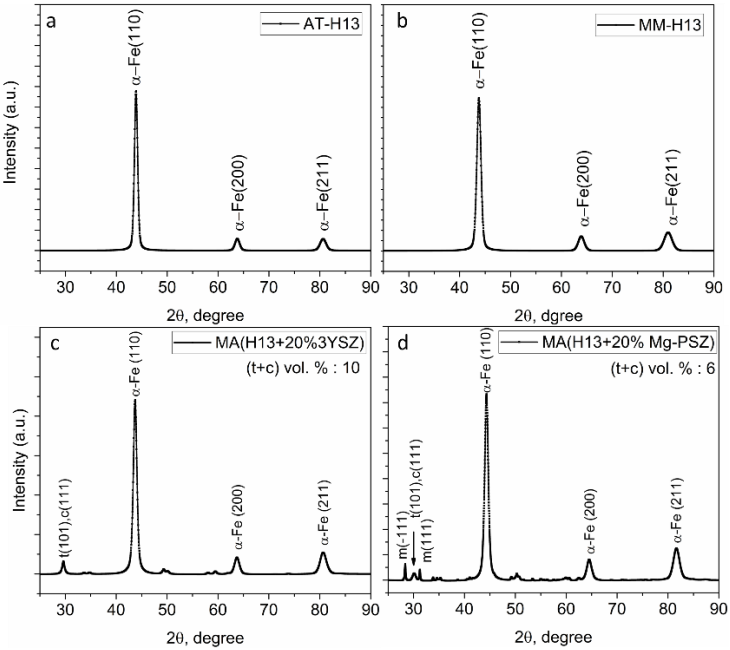

Figure IV-44. XRD patterns of as-sintered samples, a) AT-H13, b)MM-H13, c) MA(H13+20%3Y-PSZ) and d) MA(H13+20%Mg-PSZ). (Please note that the Crystallite size of Monoclinic Zirconia is set to 100 nm to make it possible to refine the crystallite size of tetragonal and α-Fe with the MAUD software)

Figure (45) shows the relative density vs. the hardness of the samples. Near full density sample (~98.6%) is achieved for MA (H13+20%Mg-PSZ). The 10 vol. % Mg-PSZ reinforced composite also shows a relatively high density (~97.5%). Therefore, for these samples, it is possible to make some considerations about the effect of microstructural refinement and strain hardening induced by high energy milling and the simultaneous effect of dispersion hardening by PSZ particles. As discussed earlier, the relatively coarse-grained AT-H13 with a density equal to 99.5% shows a hardness of 630 HV10. Despite the lower density (~98.6%), hardness is increased to 755 HV10 in MM-H13 due to the combined effect of the increased dislocation density and grain refinement. The addition of 10 vol. % and 20 vol. % Mg-PSZ led to a further increase in hardness to 850 HV10 and 920 HV10 respectively (about 100 and 150 HV10 higher compared to the MM-H13), an indicative measure of dispersion hardening effect. Any additional contribution due to further structural refinement and defect can be excluded since the mean crystallite sizes of α-Fe in MM-H13, and the

MA samples are very similar. The hardness of MA (H13+3Y-PSZ) composites is negatively affected by the incomplete densification. The very high scatter in hardness results can be justified by the porosity content.

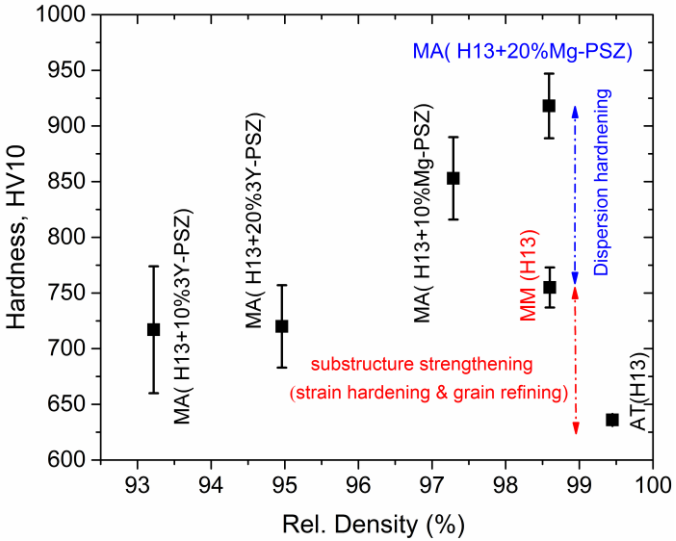

Figure IV-45. Hardness vs. density of the as-sintered samples

4.4.2 Residual stress analysis in the composites

Given the lower coefficient of thermal expansion (CTE) of the ceramic particles compared to the matrix, residual thermal stress build-up at the at the matrix-reinforcement interface upon cooling down from the processing temperature can be expected [173]. These stresses are hydrostatic in nature and are tensile in the matrix and compressive in the reinforcement. Assuming a strongly bonded particle/matrix interface and presupposing no plastic stress relaxation, it is convenient to write the developed stress in the PSZ particles as follows:

$$\sigma_p = \frac{(\alpha_m - \alpha_p)\Delta T}{\frac{0.5(1+\vartheta_m)+(1-2\vartheta_m)f}{E_m(1-f)} + \frac{(1-2\vartheta_p)}{E_p}} \quad (12)$$

Where subscripts *m* and *p* stand for matrix and particle respectively, *α* is the *CTE*, *v* is the Poisson ratio, *E* is Young modulus, and *f* is the volume fraction of the reinforcement. The stress inside the matrix might be then resolved into two principal components in a spherical coordination system.

$$\sigma_{rm} = \frac{\sigma_p}{1-f}\left(\frac{r^3}{R^3} - f\right),\ \sigma_{\theta m} = \frac{-\sigma_p}{1-f}\left(\frac{r^3}{2R^3} + f\right) \quad (13)$$

where *r* is the reinforcement (i.e. ZrO_2) radius, R is the distance from any chosen point in the matrix to the closest PSZ particle. These stresses are schematically illustrated in Figure (46a) using the data from the literature which is listed in Table 5.

Table IV-5. Material properties of matrix and reinforcement

	E (GPa)	ϑ	CTE at 1100°C (10^{-6}/°C)
Reinforcement	210[174]	0.32[174]	10.2 [175]
Matrix	208[173]	0.28[173]	16[173]

According to the calculations, tangential tensile stress is about 900 MPa at the particle/matrix interface. For the 20 vol. % reinforced composite it assumes a descending trend to an average value above 250MPa at a substantial distance (i.e. 1.7r) from the interface. The magnitude of this stress might be underestimated for the composites under study, given the very fine dispersion of PSZ particles and the very low interparticle spacing. The compressive radial stress overcomes 1000 MPa at the particle/matrix interface and decreases to zero far from the interface (i.e. 1.7r). However, even this theoretical evidence cannot be easily justified because of the overlapping of stress fields of other PSZ particles. The calculated *average* tangential stress might be approved by the mechanical equilibrium formula suggested by Mura for the MMCs [176],

$$f \times \sigma_p + (1-f) \times \sigma_{Avg\ m} = 0 \quad (14)$$

Where f is the volume fraction of reinforcement, σ_p is the stress in reinforcement (i.e. 1015 MPa) and $\sigma_{Avg\ m}$ is the average stress in the matrix. Substituting the known variables in the formula, the average stress in the matrix for 20 vol. % reinforced composites is 254 MPa, which is in a good agreement with that derived from Eq. 13.

XRD patterns of a batch of mixed powders (i.e. stress-free) and as-sintered samples were elaborated to evaluate the α-Fe peak shift (i.e. change in cell parameter) to tailor the existence of residual tensile stresses in the matrix. Peak shift to lower 2θ angles (Figure 46b) might stand for the residual tensile stresses in the matrix. The cell parameters were calculated to be 2.90352 Å and 2.90749 Å for mixed powders and sintered sample respectively. The stored elastic stress calculated by Eq. 15, reveals that a residual tensile stress equal to 280 MPa has been generated in the H13 matrix as a result of thermal mismatch.

$$\sigma = E\mathrm{\Epsilon} = E \times \left(\frac{a_{SPS} - a_{Powder}}{a_{Powder}}\right) \quad (15)$$

"a" is the cell parameter of the of α-Fe (110) and *E* being the Young's modulus of the matrix.

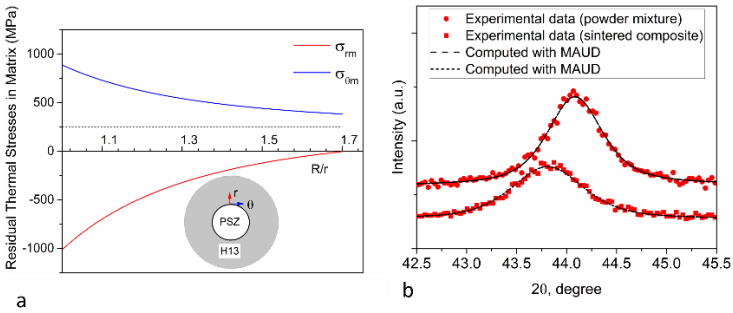

Figure IV-46. a) Schematic of residual thermal stress distribution as a function of distance from zirconia particle and b) XRD pattern [(110) peak] of mixed powders and as-sintered composites

The existence of residual stress in the matrix confirms that the bonding of PSZ/H13 is sufficiently strong to avoid relaxation by interfacial debonding. Dispersed PSZ particles are submicron in size and the steel particles size distribution has become narrower after MA as previously shown in Figure (38). The influence of particle size on the interface debonding at a given stress level might be estimated by Weibull distribution [177]. The probability is calculated as follows:

$$F_i(x) = 1 - exp[-\left(\frac{d_i}{d_0}\right)^3 \left(\frac{x}{S}\right)^m] \quad (16)$$

Where d_i is the particle diameter, x is the stress level, d_0 is a normalized parameter and S and m are the scale and shape parameters respectively. Hence, the probability debonding for a stress level between x and (x+Δx) is $f_i(x)\,dx$ where $f_i(x)$ can be written as:

$$f_i(x) = \frac{dF_i(x)}{d_x} = -\left(\frac{d_i}{d_0}\right)^3 \frac{m}{S}\left(\frac{x}{S}\right)^{m-1} exp[-\left(\frac{d_i}{d_0}\right)^3 \left(\frac{x}{S}\right)^m] \quad (17)$$

According to this equation, by decreasing the particle size, the debonding probability considerably decreases. Therefore, considering both the experimental observations and the theoretical calculations, it can be argued that the debonding at the PSZ/matrix interface should be unlikely to occur. To provide a direction to the practical implication of the findings, one has to consider the *fracture behavior* of the as-sintered composites. The tensile fields might deflect the crack towards the reinforcing particles [69] which in turn provide the necessity of incorporation of reinforcing particles with the lowest flaws and maximum fracture toughness.

4.4.3 High-temperature chemical stability

The microstructures of the sandwich structure (H13/PSZ/H13) are depicted in Figures (47a) and (47c).

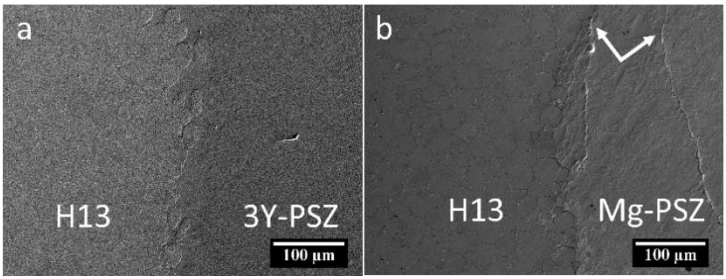

Figure IV-47. SEM micrographs on the interface of a) H13/3Y-PSZ and b) H13/Mg-PSZ (arrows are pointing to the cracks)

A seamless interface has formed in H13/3Y-PSZ while Mg-PSZ/H13 interface is characterized by cracking of the MgPSZ particles at the interface and propagation of these cracks inside the Mg-PSZ zone. The finer 3Y-PSZ powders can account for the absence of interface failure and crack extension in H13/3Y-PSZ. The tensile stress developing in the matrix upon cooling may cause cracking in the adjacent PSZ particles. Based on energy balance [178], there exist a critical particle size above which cracking is likely to occur.

$$d_c > C/\sigma_t \quad (18)$$

Where d_c is the critical particle size, C is a constant depending on the matrix/reinforcement pair, and σ_t (the tensile stress) is calculated by Eq. 13. In a large number of materials combination where the second phase shows lower CTE, relatively large particles can satisfy the crack extension condition. Therefore the 3Y-PSZ particles (d=0.5 µm) may not have satisfied the requirement in Eq.18 while the coarser as-received Mg-PSZ particles (d=5 µm) satisfied the crack extension condition. From a mechanical properties point of view, these observations further confirm the beneficial effect of MA on refining the large Mg-PSZ particles size resulting in the absence of particle cracking in MA(H13+Mg-PSZ) composites.

The EDS line scan results in H13/Mg-PSZ (Figure 48a) show that the concentration of Zr, Si, and Mg increases across the interface and remains constant within the PSZ region. The condition is the same while looking at the line scan analysis of H13/3Y-PSZ. Under present sintering condition (i.e. 1100°C, 30 min), *the consolidated bulks from as-received powders forming a planar interface* apparently show no precipitates

or any newly formed phase. The absence of reaction phases is of particular importance for Mg-PSZ reincforced composite in which silicates have been previously found to precipitate due to the presence of SiO_2 impurity[90,179]. These silicates at the interface might impede the t to m transformation in PSZ particle [117].

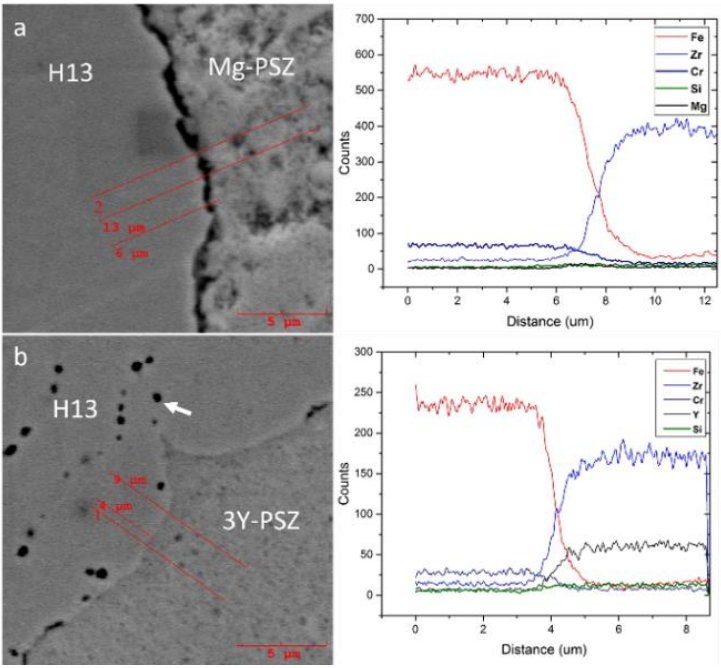

Figure IV-48. EDS line scan analysis results for the planar interface in a) H13/Mg-PSZ and b) H13/3Y-PSZ (arrow is pointing at the H13 surface oxides)

However, in *3Y-PSZ reinforced composites* produced by mechanical alloying, the backscattered electron (BSE) micrographs of the as-sintered sample revealed the formation of small sized reaction layers adjacent to the unalloyed H13 particles (Figure 49). These areas are characterized by high concentrations of Cr, V and Zr and the absence of Fe.

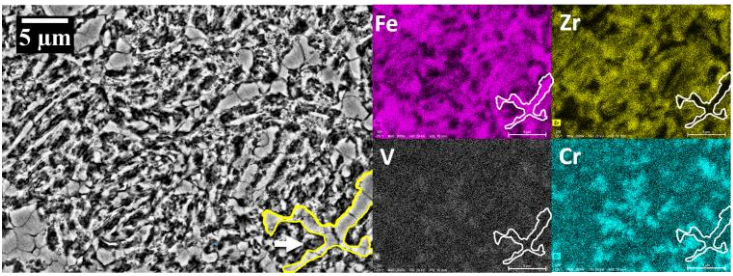

Figure IV-49. EDS elemental mapping on 3Y-PSZ reinforced composite (arrow is showing the emerged new phase, and the dashed area is un-alloyed H13)

In *Mg-PSZ reinforced composites* (Figure 50), EDS mapping did not show any visible reaction zone. In particular, considering Si distribution, it is rather hard to deduce whether silicates have been formed at the matrix-reinforcement interface or not.

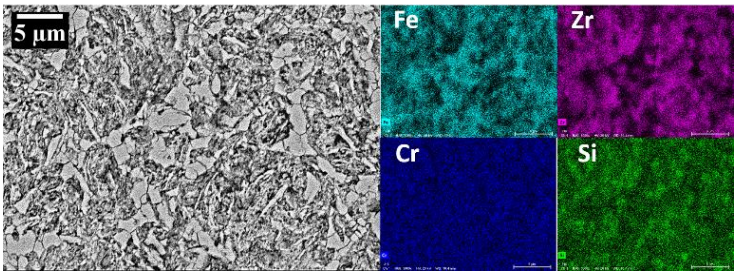

Figure IV-50. EDS elemental mapping on Mg-PSZ reinforced composite (brighter spots in BSE micrographs are PSZ particles)

The coexistence of Cr_2O_3 and ZrO_2 in Steel-Zirconia joint is thermodynamically plausible at high temperatures (i.e. 1300°C) and an oxygen partial pressure greater than 5.7×10^{-10} mbar [180] where ZrO_2 can be reduced at the expense of oxidation of Cr. The reduction of Zr does not completely occur, and zirconia will still exist in a non-stoichiometry state [181]:

$$ZrO_2 \rightarrow ZrO_{2-X} + X/2O_2, \quad 0 \leq X \leq 0.02 \qquad (19)$$

However, in a severe plastically deformed matrix with a high density of structural defects (i.e. dislocations) that might accelerate the diffusion mechanisms, these reactions might occur even at a temperature lower than that suggested in the literature. Moreover, the very fine particle size of 3Y-PSZ leads to a much larger PSZ-H13 interface area, shorter diffusion path and faster kinetics for the precipitation reactions of Cr and V oxides compared to the sandwich experiment above. As stated

earlier, the peaks pertaining to new phases could not be detected by XRD analysis, showing only the presence of *t-ZrO₂* and martensite. This can be explained by the low amount and very fine distribution of these precipitates. In the case of Mg-PSZ reinforced composites, the same phenomenon is not observed due to the coarser size of PSZ particles.

In order to prove the chemical stability of the composites and to validate the above conclusions, samples were further subjected to long time (i.e. 1 and 2 h) exposure at the sintering temperature (i.e. 1100° C) under vacuum (5.0×10^{-7} bar). After two hours (Figures 51a and 52b) in both Mg-PSZ and 3Y-PSZ reinforced composites, new phases have emerged. EDS spot analysis results for Mg-PSZ and 3Y-PSZ reinforced composites are listed in Tables 6 and 7 respectively.

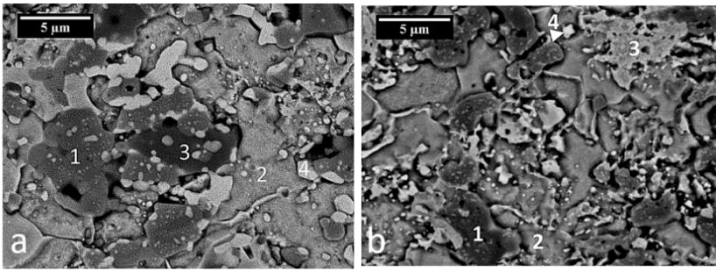

Figure IV-51. BSE micrograph of composite after 2 h holding at 1100°C, a) MA(H13+20% Mg-PSZ) and b) MA(H13+20% 3Y-PSZ)

Table IV-6. EDS spot analysis on 20 vol. % Mg-PSZ reinforced composite (wt. %)

Zone	Fe	Zr	Cr	V	Si	Mn	Mo	Mg
1	24.5	14.3	25.1	6.0	4.2	1.7	-	0.5
2	86.8	0.3	0.9	-	-	-	1.8	-
3	44.0	6.4	4.6	1.0	11.6	5.1	-	2.9
4	11.3	71.4	0.1	0.6	-	-	-	0.4

Table IV-7. EDS spot analysis on 20 vol. % 3Y-PSZ reinforced composite (wt. %)

Zone	Fe	Zr	Cr	V	Si	Mn	Mo	Y
1	38.0	8.1	20.7	5.0	1.8	1.2	-	-
2	74.2	-	0.3	-	-	-	1.7	-
3	66.8	10.8	0.5	-	0.2	-	1.4	0.6
4	23.5	52.7	0.3	-	1.7	-	1.0	1.3

Spot 1 in both micrographs is corresponding to a Cr, V rich zone. It appears that the reaction layer has been formed in the H13-ZrO_2 system. These zones might consist

of complex oxides of Cr, V, and Zr. Spot 2 in both micrographs is showing H13 matrix in the vicinity of reaction zones which has been depleted of Cr, V, and Mn. Therefore, it can be postulated that inter-diffusion of several elements has taken place during high-temperature holding thus resulting in the formation of complex oxides. In Figure (51a), Spot 3 is characterized by a high concentration of Si, Mn, and Mg that might represent the precipitation of (Mg, Mn)Si_2O_4 which was formerly reported in Steel-Mg-PSZ systems [90,179]. In Figure (51b) spot 3 is an MA area which is depleted of Cr and V. The brightest particles (Spot 4 in Figures 51a and 51b) are PSZ particles. Further investigations are needed to be performed by the aid of EBSD analysis on these samples to elaborate more on the composition and structure of the newly formed phases.

The conclusion is mostly intended to highlight the efficiency of short time sintering of SPS that has not allowed the formation of excessive reaction zones. For the as-sintered 3Y-PSZ reinforced composite, the width of the reaction layers was limited to several microns. The presence of small and limited reaction zone can be beneficial in view of the strengthening of reinforcement and matrix interface which in turn results in more efficient load transfer from the matrix to the reinforcement [182]. The absence of reaction zones in the as-sintered Mg-PSZ reinforced composites can be related to the coarser particle size corresponding to lower surface energy and lower kinetics of Mg-PSZ/Steel interfacial reaction. However, since in the present study the properties of the composites with the incorporation of fine sized Mg-PSZ particles is not elaborated, a definitive interpretation of the *dependence of the interfacial reaction kinetics on the reinforcement particle size* cannot be made.

4.4.4 Tempering resistance

Figure (52) shows the tempering curves of the as-sintered tool steels samples at 550°C and 650°C respectively.

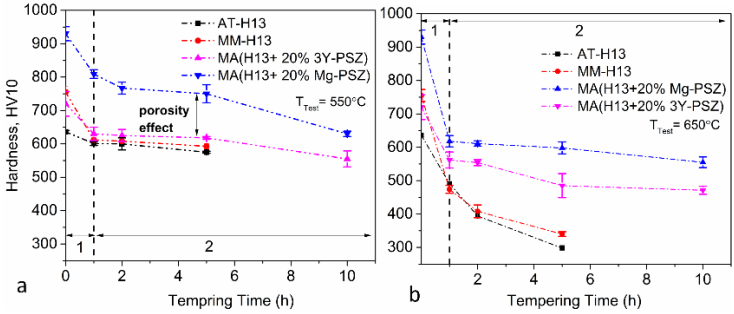

Figure IV-52. Tempering curves of the samples at a) 550°C and b) 650°C

A drastic drop in hardness is evident for all the samples after 1 hour of tempering at both temperatures (stage 1). For all samples, the rate of this drop is higher at 650°C (i.e. higher than secondary hardening peak temperature of H13) compared to 550°C which is very near to the secondary hardening peak temperature.

Moreover, In the case of MM-H13 and composites, the rate of the drop is higher than that of AT-H13. As discussed earlier, this sudden drop is caused by dislocation recovery in martensite substructure *irrespective of the initial dislocation density*. Therefore, in view of the increased initial dislocation density (i.e. strain hardening) contributing to the higher initial hardness of the milled samples, the loss of hardness (i.e. $\Delta H=H_{intial}-H_1$) as a result of dislocation recovery should be higher. By extending the tempering time, the hardness of AT-H13 and MM-H13 samples decreases at a roughly constant rate while this rate is higher at 650°C. As mentioned earlier in the present work, it appears that the MM-H13 is more resistant to softening than the AT-H13 at 650°C thanks to the presence of much finer carbides. In the case of the composites, after the primary drop, no significant reduction in hardness can be observed even after 10 hours of isothermal holding. The difference in hardness values of MA (H13-20%3Y-PSZ) and MA (H13-20%Mg-PSZ) is systematic and can be related to the higher relative density of the latter. One can deduce that after 1 hour of tempering (i.e. stage 1), the strain hardening contribution to strengthening in composites becomes insignificant especially at 650°C. In stage 2, due to the good thermal stability of PSZ particles at the test temperatures, the synergetic effect of finer carbide size and dispersion hardening by PSZ particles seems to be the dominating mechanism responsible for the higher hardness of composites.

The microstructures of the samples after tempering resistance tests are shown in Figure (53).

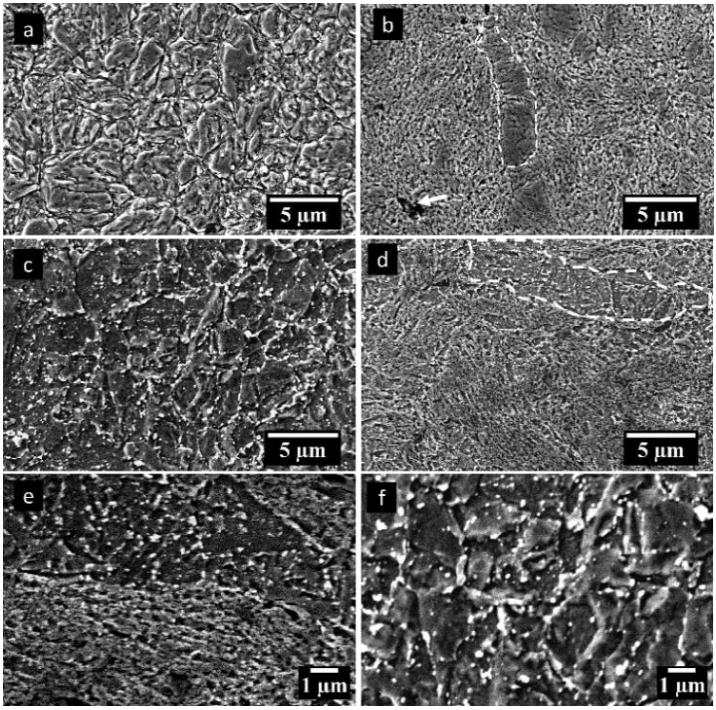

Figure IV-53. a) AT-H13 microstructure after 5 h tempering at 550°C, b) typical composite microstructure after 10 h tempering at 550°C (dashed area represent un-alloyed MM-H13), c) AT-H13 microstructure after 5 h tempering at 650°C (please note the precipitation of carbides on prior austenite boundaries), d) typical composite microstructure after 10 h tempering at 650°C (dashed area represent un-alloyed MM-H13), e) higher magnification micrograph of the composite microstructure tempered at 650C for 10 h , (please not the carbide size and distribution in un-alloyed MM-H13 regions) and f) higher magnification micrograph of the AT-H13 microstructure tempered at 650C for 5 h

Figure (53a) depicts the AT-H13 microstructure after 5h tempering at 550°C. The microstructure consists of tempered martensite with fine secondary carbides. Figure (53b) represents the typical microstructure of the composites tempered for 10 hours at 550°C showing UFG microstructure. The dashed area is representing an unalloyed, yet severely deformed region which shows a much finer microstructure compared to the AT-H13. These areas can also account for the microstructure of

MM-H13. Figure (53c) depicts the AT-H13 microstructure showing a larger number of secondary carbides precipitated (carbide films) on the prior austenite grain boundaries. Figure (53d) shows the composite tempered for 10 h at 650°C. The UFG microstructure contains very fine and homogeneously distributed carbides. Looking at the dashed area (representing the unalloyed H13) in the same figure, it can be appreciated that the carbide size is much finer than that of AT-H13 that precipitates are more homogenously distributed. The higher magnification micrographs in Figures (53e) and (53f) better highlight the size and distribution of secondary carbides inside the unalloyed H13 regions in composite (i.e. MM-H13) and the AT-H13 respectively. It can be concluded that the very fine PSZ particles embedded in the ultra-fine grained matrix seem to be stable to the temperature exposure and dispersion hardening effect holds even for longer tempering times[2].

4.4.5 Hot Compression

The hot compression test results of 20 vol. % reinforced composites and the unreinforced samples are listed in Table 8. AT-H13 shows the lowest yield strength in all testing temperatures. The yield strength of the UFG MM-H13 is around 1.3 times more than the AT-H13 thanks to the strain hardening and substructure strengthening induced by mechanical milling. The yield strength is significantly improved by the incorporation of PSZ particles especially at higher temperatures indicative of the dispersion strengthening effect of the PSZ reinforcement. Again, the lower relative density of MA (H13+20% 3Y-PSZ) might be responsible for the lower compressive yield strength of the composite compared to the Mg-PSZ reinforced counterpart.

Table IV-8. 0.2% offset compressive yield strength of the samples

Temperature (°C)	AT-H13	MM-H13	MA (H13-3Y-PSZ)`	MA (H13-Mg-PSZ)
20	1810 MPa	2130 MPa	2420 MPa	2650 MPa
450	720 MPa	1130 MPa	1920 MPa	2070 MPa
650	480 MPa	795 MPa	920 MPa	1270 MPa

It is noteworthy to mention that, the room temperature test results are in line with the approximated yield strength calculated from the hardness measurements (Table 9). The conversion of the Vickers hardness to Yield strength is done using the following relation for the "severely cold worked steel" [183].

$$\sigma_y(GPa) = 0.003HV \quad (20)$$

Dealing with particle reinforced MMCs, in a hardness test, deformation is localized, and particles undergo *compressive stresses* with a high degree of stress triaxiality[184]. As a result, particle fracture during indentation is suppressed, and HPs contribute to the "strengthening." Therefore, the *compressive yield strength* might show a meaningful correlation with the *hardness*.

Table IV-9. Estimated room temperature yield strength using the hardness results

Temperature (°C)	AT-H13	MM-H13	MA (H13-3Y-PSZ)`	MA (H13-Mg-PSZ)
20	1910 MPa	2250 MPa	2160 MPa*	2760 MPa

*relative density in this sample is 95%

The stress-strain curves at room temperature and 650°C tests are shown in Figures (54a) and (54b) respectively. Due to approaching the force limit of the equipment (i.e. 20 KN, corresponding to a stress equal to about 2800 MPa) at the initial stages of strain hardening, it was not possible to complete the room temperature compression test to 6% strain for the composites.

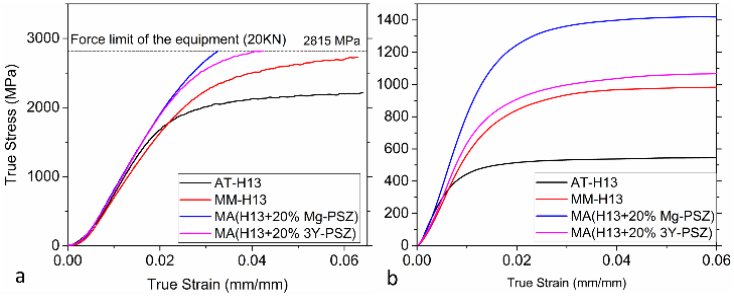

Figure IV-54. Stress-strain curves of samples tested at a) room temperature (20 °C) and b) 650°C

Figure (55) shows the strain hardening rate curves and strain hardening exponents (n) of the samples at 650°C and 450°C under quasi-static compressive deformation. The matrix strain hardening can be described by the dislocation movement and accumulation of dislocations. The general lower hardening rates at 650°C compared to 450°C is due to the loss of strength by increasing the temperature that counteracts the strain hardening by compression. The lower strain hardening rate of AT-H13 compared to MM-H13 can be attributed to its larger grain size and lower density of structural defects (i.e. dislocations) in the as-sintered condition. As it can be appreciated from the graphs, the "apparent strain hardening rate" at the initial stages of plastic deformation is highest for the Mg-PSZ reinforced sample due to the

strengthening effect of Mg-PSZ particles which is in agreement with the observations of Martin et al. [185] For TRIP steel-Mg-PSZ composites. This effect is less pronounced in 3Y-PSZ reinforced composite which is probably due to the higher amount of porosity in the composite material.

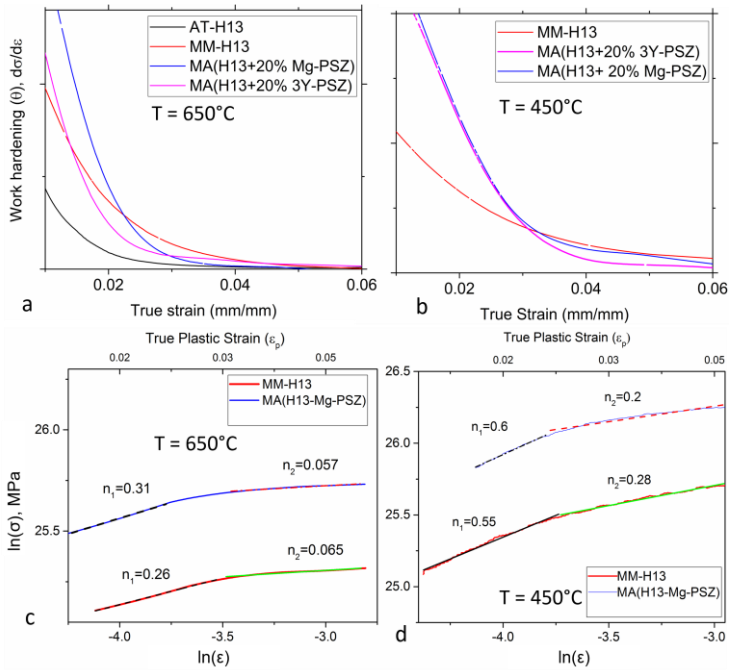

Figure IV-55. a) Strain hardening rate of the samples at 650°C, b) strain hardening rate of the samples at 450°C , c) hardening exponent (n) during plastic deformation for matrix material and Mg-PSZ reinforced composite at 650°C and d) hardening exponent (n) during plastic deformation for matrix material and Mg-PSZ reinforced composite at 450°C

From around 3% up to 6% plastic strain at both temperatures, it is evident that the hardening rate and hardening exponent drop to lower values compared to the matrix material (i.e. MM-H13). The decline in hardening rate might have caused by debonding and fracture of PSZ or the reaction products[179,186,187]. The increased work hardening rate of the MMCs can be ascribed to the geometric constraints generated by the presence of HPs impeding the dislocations movement, and local increase of HPs volume fraction under loading and accordingly the parallel decrease in volume fraction of the matrix which is being deformed. Moreover, PSZ particles may undergo t-m stress induced transformation accompanied by volume expansion. The

generation of additional compressive stresses as a result of PSZ volume expansion may also contribute to the enhanced strain hardnening of the composite. The contribution of this peculiar characteristic of PSZ particles to strenghening has to be confirmed.

To better describe the hardening response of the composites it would be appropriate to start with the considerations on the compressive yield strength (σ_y^m) of the MM-H13 matrix (i.e. 795 MPa and 920 MPa at 650°C and 450°C respectively), work of fracture of PSZ particles and the PSZ-H13 interface strength. The work of fracture of bulk 3Y-PSZ is reported to be 100 J m^{-2} and 18 J m^{-2} at room temperature and 600°C, respectively[188]. The planar Interface strength of Y-PSZ coating on stainless steel is reported to vary between 206 to 500 MPa [189].

For the present composites, additional considerations should be applied. Firstly, the successfully dispersed PSZ particles are submicron sized. Therefore the probability of the existence of critical flaws (according to Griffith theorem) inside these particles is very low. This was confirmed by the observations in Section 4.4.2. So it is possible to postulate that the work of fracture for these particles can be as higher than 20 J m^{-2} at 650°C. The larger (un-dispersed) PSZ particles or the brittle reaction products might fracture at lower stresses, so it is possible to set the fracture energy lower than 18 J m^{-2} for these particles. Secondly, referring to the considerations in section 4.4.2, no debonding was observed at the interface upon cooling and subsequent development of thermal stresses, therefore, interfacial strength (σ_{max}, i.e. the maximum stress at the interface calculated from eq.13) of the fine spherical shape PSZ particles embedded in the matrix should be higher than that observed in a planar interface and can be set to 900 MPa which is equal to the developed tensile stress upon cooling.

Following the work of Zhang et al. [187] and Pruger et al. [189], it is possible to define the normalized interface strength (α) as the ratio of the "unreinforced matrix" yield stress (σ_y^m) to (σ_{max}) which is equal to 1.13 at 650°C. For α>0.5 it is possible to assume a **strong** interfacial bonding in compression. It should be noted that this threshold increases to 1 in tension. In general, under compression, reinforcements provide much more strengthening than in tension. One explanation is that, debonding in compression occurs with considerably lower magnitude at the same strain level.

Taking the normalized interface strength *(α)* and the fracture energies into account, it will be possible to classify the interfaces in the H13-PSZ system as a ***strong*** interface. The "strong" interface fails by debonding of flawless fine PSZ particles upon straining to a critical strain associated with matrix strain hardening at the poles of the particles. While for the larger PSZ particles or brittle reaction products, well before interface debonding, particle fracture occurs and is considered as the main

damage mechanism[190]. The stress-strain curves are showing that the particles have significantly contributed to the strengthening of the composite and are in good agreement with the work of Zhang et al.[187] stating that the ***strong interface*** effectively strengthens the material until a full debonding occurs. Effective load transfer from the matrix to the reinforcement which is a function of the strength of the interface may trigger the t to m transformation in PSZ particles, especially during compression[115,189]. Because under compression, the t-m transformation may continue even if full debonding occurs but this event will take place at a lower rate [189]. In order to check if the t-m transformation has been taken place during the compression test, the XRD patterns of the "*deformed zone"* of the compressed MA (H13+20% 3Y-PSZ) which showed the highest vol. % of the tetragonal phase in as-sintered condition was analyzed. As it is shown in Figure (56), the compressed area did not show the initial t-ZrO_2 content (i.e. 10 vol. %), moreover the vol. % of monoclinic phase is increased to 7.5 vol. %. Therefore, it is possible to postulate that the stress induced t-m transformation contributes to the increased hardening rate of the MMCs at the initial stages of plastic deformation. It has to be stated that the MM-H13 shows a reasonably high strength even at high temperatures. Therefore, at a critical strain level, stress concentration at the poles of the PSZ particles is expected to be high enough to cause damage to the interface or large PSZ particles.

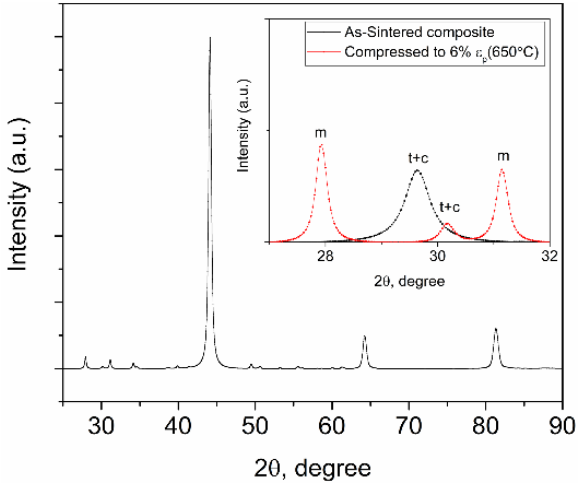

Figure IV-56. XRD pattern collected from the deformed MA (H13+20% 3Y-PSZ) at 650°C. (Please note the comparison of the spectra with the spectra of as-sintered sample)

Unfortunately, reliable results could not be obtained from the XRD analysis on Mg-PSZ reinforced composites mainly because of low vol. % of t-ZrO_2 in as sintered samples and difficulties in sample preparation.

Figure (57a) is showing the un-deformed surface of the Mg-PSZ reinforced composite. Figure (57b-c) are showing the deformed surface of Mg-PSZ reinforced composite subjected to hot compression at 650°C and Figure (57d) is showing the debonding of a fine PSZ particle (spot 1). The figure also highlights the fracture of a reaction product which is rich in Si, Mn, and Zr, (spot 2). The EDS spot analysis results of the particle are listed in Table 10.

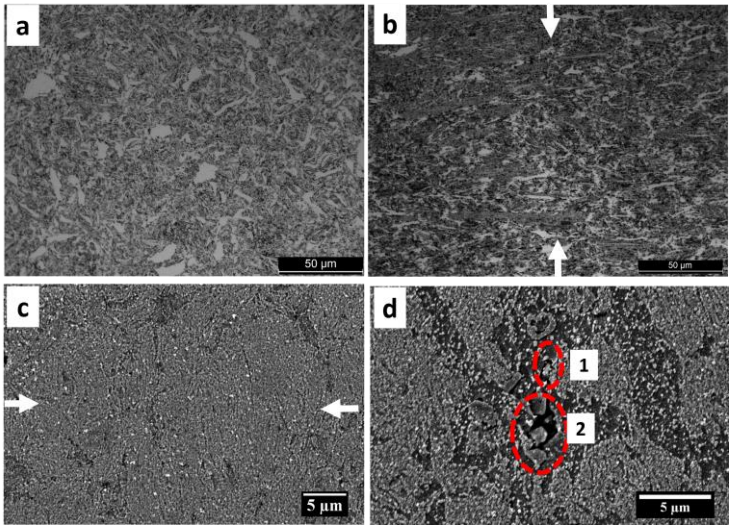

Figure IV-57. Deformed surface of the samples at 650°C, a) OM micrograph of the un-deformed composite (white isolated regions are un-alloyed H13), b) OM micrograph of the deformed composite, please see the plastic deformation of unalloyed H13, arrows indicating compression direction, c) SEM micrograph of the deformed surface, arrows indicating compression direction and d) higher magnification SEM micrograph showing particle debonding (1) and particle fracture (2)

Table IV-10. EDS spot analysis results on particles (1) and (2) in Figure (57d), wt. %

spot	Fe	Zr	Cr	V	Si	Mn	Mo	Mg
1	52	35	5	1.4	1	0.4	-	0.3
2	62	25	7	1	5	1.7	1	-

It appears that the transformation of *t* to *m* can be successfully exploited to strengthen the H13 matrix.

Application of higher heating rates for the SPS may completely exclude the formation of thermodynamically plausible reaction products. On one side, elimination of the reaction layers can be beneficial since these products are generally brittle and detrimental to strength. Moreover, their emergence is accompanied by t-ZrO_2 destabilization. On the other hand, extremely thin and limited reaction layers can promote the interfacial strength allowing more efficient load transfer. Therefore, elaboration on the extent and composition of silicates and possibly spinel phases are of the future work of the author.

4.4.6 Fracture Toughness

The hardness vs. fracture toughness of heat-treated composites together with the results of 20 vol. % TiC reinforced H13 are shown in Figure 58. The TiC reinforced composite showed a relative density equal to ~ 98.5 %. In comparison with the data of unreinforced MM-H13 (i.e. ~420 HV10 and K_{app}=36 MPa $m^{1/2}$) a general decrease in fracture toughness and a general increase in hardness can be appreciated. The apparent fracture toughness of Mg-PSZ reinforced composite is the highest among all 3 samples, the hardness being practically the same of TiC reinforced composite. The MA (H13+ 20%3Y-PSZ) is showing the lowest fracture toughness and also a very low hardness compared to the other counterparts, due to the high inter-particle porosity.

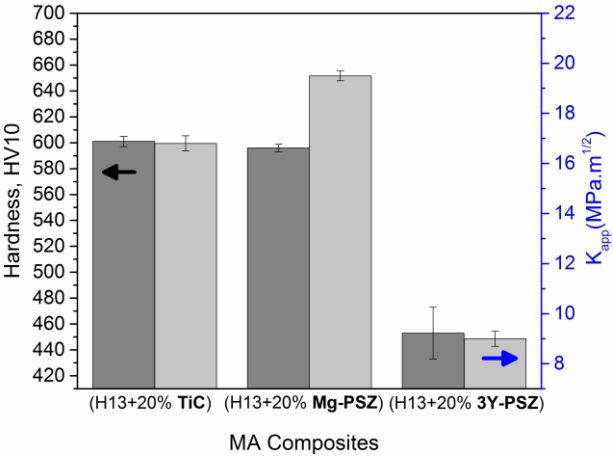

Figure IV-58. Hardness vs. apparent fracture toughness of the composites

Figure (59a) depicts the fracture surface of TiC reinforced composite. The surface seems to exclude any ductility contribution to fracture. The interparticle fracture (dashed area), and very fine and limited cleavage facets probably belong to the unalloyed H13 zones can be seen in Figure (59d). The higher magnification micrograph in Figure (59d) reveals the mechanism of void initiation by matrix/TiC decohesion. There also exists a few number of fractured TiC particles on the fracture surface (see Figure 60). The EDS area analysis as a semi-quantitative analysis revealed the presence of 15±1.5 wt. % Ti on the fracture surfaces corresponding to around 25 vol. % of TiC which is 1.25 times higher than the initial mixing volume. The fracture surface analysis suggests that the crack has propagated mainly through the reinforcement or by decohesion at reinforcement/particle interface. The fracture surface of Mg-PSZ reinforced composite shown in Figures (59b) and (59d) features some decohesion between the unalloyed H13 regions and the composite parts. The higher magnification micrograph (Figure 59f) reveals the occurrence of the particle/matrix decohesion together with the presence of clusters of PSZ and also regions characterized by fractured "reaction products." The vol. % of Mg-PSZ on the fracture surfaces is approximately 1.1 times higher than the nominal mixing volume. In these composites, the absence of extensive interparticle fracture confirms successful consolidation and development of strong metallic bonding. Therefore, upon the increase of stress concentration at the poles of the particles, the reinforcing particles fractured or debonded and crack propagated in the most energetically preferential path. This type of fracture behavior was formerly evidenced for the MMCs processed with severe plastic deformation showing a very homogeneous distribution of fine HPs [87]. Generation of tensile fields (as a result of the thermal mismatch between matrix and reinforcement) near the particle/matrix interface, might also be effective in view of crack deviation towards the particle/matrix interface [18].

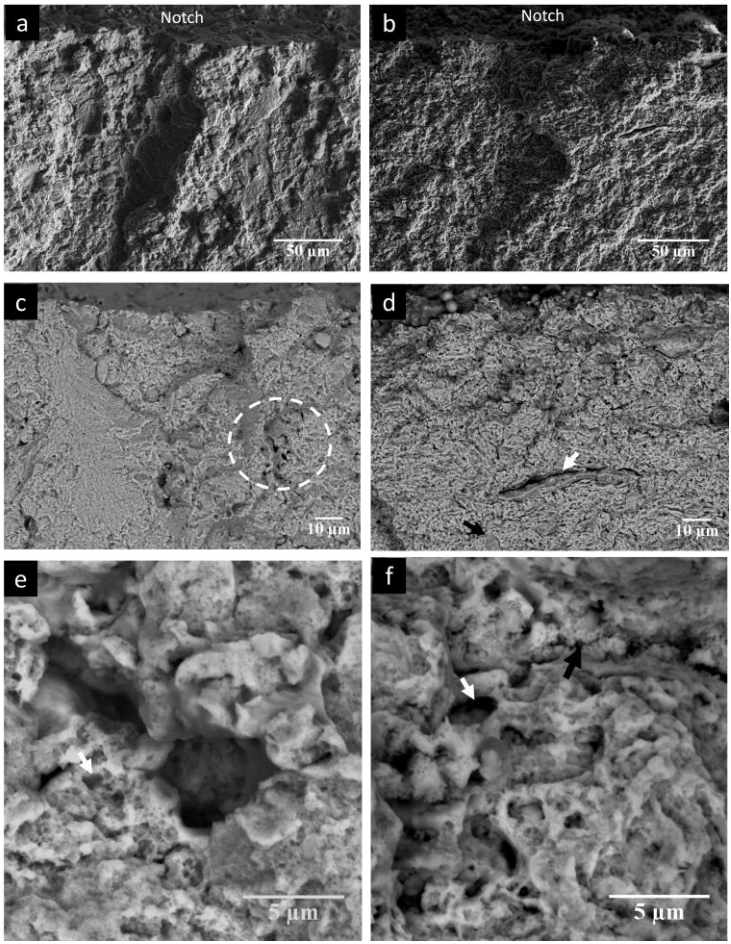

Figure IV-59. SEM micrographs of fracture surfaces of a) TiC reinforced composite, b) Mg-PSZ reinforced composite, c) higher magnification micrograph showing interparticle fracture at a porous region (dashed circle) in TiC reinforced composite, d) higher magnification micrograph showing some cleavage facets (black arrow) and decohesion at the un-alloyed H13/composite interface (white arrow), e) BSE higher magnification micrograph showing formation of voids (<1µm) as a result of particle matrix decohesion in TiC reinforced composite (arrow is pointing to a relatively big TiC particle) and f) BSE higher magnification micrograph showing plenty of voids , clusters of zirconia (black arrow) and a cracked reaction product (white arrow) in Mg-PSZ reinforced composite.

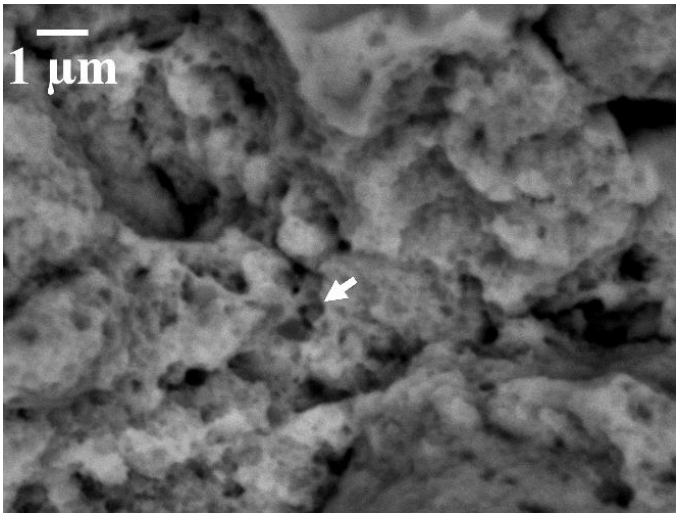

Figure IV-60. Fracture surface of TiC reinforced composite (arrow points at the fractured TiC particle)

MA (H13+20% 3Y-PSZ) shows a pure inter-particle fracture presenting lots of fine un-dispersed PSZ particle clusters on the fracture surface as shown in Figures (61a) and (61b) respectively.

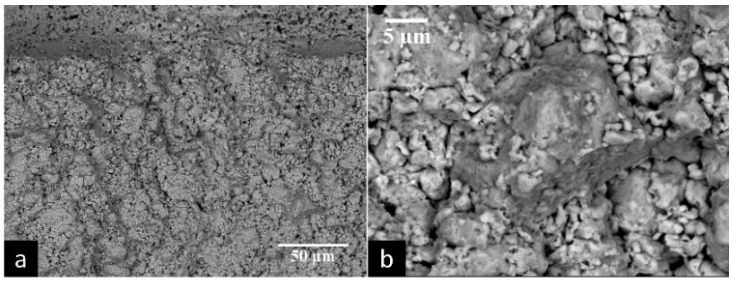

Figure IV-61.a) BSE micrographs of fracture surface of 3Y-PSZ reinforced composite showing a pure interparticle fracture and b) higher magnification BSE micrograph showing aggregated PSZ particles (brighter fine particles)

The crack propagation paths are displayed in Figure (62). Crack path in TiC reinforced composite is relatively smooth (Figure 62a) showing signs of particle decohesion, while the crack in Mg-PSZ reinforced composite tends to be deflected by the unalloyed H13/MA interface, and also through the brittle reaction products

(Figure 62b). The increased crack path tortuosity, higher fracture stress of PSZ particles with respect to TiC particles may be responsible for the increased "apparent fracture toughness" of Mg-PSZ reinforced composite. It should be noted that the existence of more extensive reaction products in the "*fracture toughness specimen*" can be related to the lower heating rate during SPS (i.e. 50 °C/min) allowing the formation of thermodynamically stable reaction products. Finally, Figure (62c) shows a pure inter-particle crack propagation in 3Y-PSZ reinforced composite confirming the poor densification and consolidation of this composite due to the accumulation of fine 3Y-PSZ particles on the steel powders surface impeding the development of metallic bonding between them during SPS.

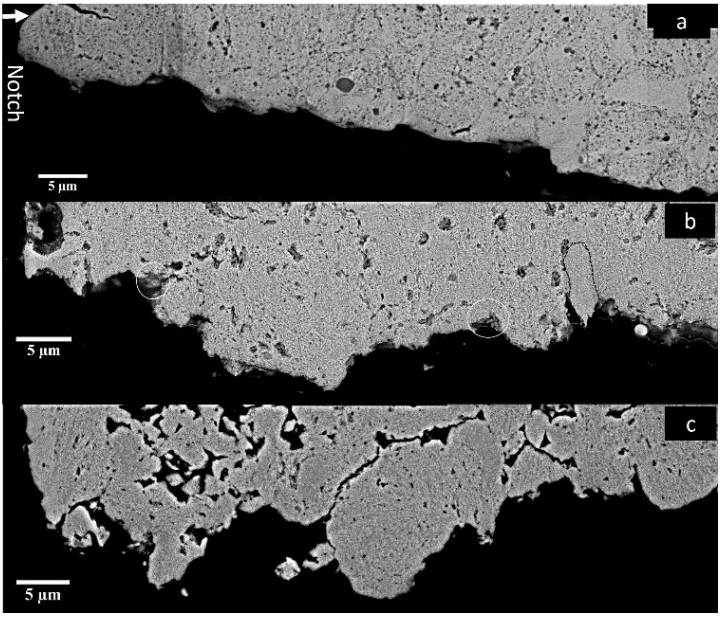

Figure IV-62. Crack propagation paths a) MA (H13+20%TiC), b) of MA (H13+20%Mg-PSZ), please see the interface decohesion of un-alloyed H13 (dashed area) and composite, and crack deflection towards the reaction products (highlighted by dashed circles) and c) of MA (H13+20%3Y-PSZ), please note the inter-particle fracture

Conclusions of part 2

- Near full density composites were successfully produced by optimized Mechanical Alloying and fast Spark Plasma Sintering.
- A too fine particle size negatively affects the densification of MA (H13+3Y-PSZ) composites due to overcoming the percolation threshold, impeding the direct H13-H13 contact during sintering. Therefore, in order to achieve a more homogenous distribution of PSZ particles into the matrix, the initial particle size of the PSZ (or the particle size ratio d_{H13}/d_{PSZ}) has to be properly selected. The practical interpretation of the present results can be summarized as follows. MA can be considered as an efficient method to refine the size of relatively large HPs (d ~ 5 μm, d_{matrix}/d_{hp} = 4) down to less than 1 μm and provide a homogenous distribution of these particles inside the matrix. A condition which guarantees the achievement of near fully dense composite reinforced with high strength flawless fine HPs. In view of the present results, this combination cannot be achieved using 10 and 20 vol. % of ultrafine HPs as the starting powder (d ~ 0.5 μm, d_{matrix}/d_{hp}= 40), since in these particles the rate of agglomeration takes over the fragmentation rate during early stages of MA. Therefore, agglomerates of ceramic particles which are mostly found on the ductile matrix particles surface may not be fully dispersed within the matrix lamellas by the continuation of MA. This will lead to incomplete densification at relatively low temperatures (i.e. 1100 °C) because of the impediment of the development of metallic contacts due to the presence of HPs on the surface.
- The tetragonal phase is partially retained in as-sintered samples and opens the way to exploit the beneficial effect of t to m stress induced transformation of ZrO_2 on fracture toughness and strength.
- The composites show improved hardness due to the combined effect of strain hardening and grain refinement induced by high energy mechanical alloying, and dispersion hardening by hard particles.
- There exists a residual thermal stress build up in the composites due to the thermal mismatch between steel matrix and reinforcement. Stresses are tensile in the matrix and compressive in the particle.
- For the samples sintered at 100°C/min, the H13/3Y-PSZ interface is characterized by a limited reaction layer with a thickness of a few microns after fast consolidation by SPS, whereas, in the Mg-PSZ reinforced composite no reaction zone was found.
- Tempering resistance of the composites was significantly increased as a result of the good thermal stability of the PSZ particles at testing temperatures.
- The room temperature and hot compressive strength of the composites were significantly enhanced by the incorporation of PSZ particles. The contribution of

stress-induced phase transformation to the strengthening of the composites was confirmed for the 3Y-PSZ reinforced composite. Fracture of large particles and debonding of fine PSZ particles occurred during the hot compression test. According to the strain hardening rate curves, fracture and debonding occur at a critical strain level of 2.5 to 3%.

- The hardness of the heat-treated composites was improved with respect to the unreinforced matrix while, as expected, fracture toughness drastically decreased. However, one of the PSZ reinforced composites (i.e. Mg-PSZ reinforced composite) showed slightly higher fracture toughness compared to the TiC reinforced composite. In view of the practically same hardness and similar densities of these two samples, the higher toughness of PSZ particles may be responsible for this increase. On the other hand, the 3Y-PSZ composite with lower density showed an inter-particle failure with poor fracture toughness.
- The lower heating rate during spark plasma sintering triggered the formation of thermodynamically plausible reaction products in PSZ-reinforced composites. Therefore in the future endeavor, the possibility of SPS at a higher heating rate should be taken into consideration.

Chapter V

Conclusions and Future Perspectives

Some of the mechanical properties of developed materials are listed in Table 1. The results obtained in the frame of this Ph.D. thesis open interesting opportunities for many industrial applications. Harmonic steels could be tested when a relatively high toughness/hardness ratio is required, i.e. for forging dies. On the other side, according to the well higher hardness of the composites, a higher abrasive wear resistance is expected. PSZ reinforced Tool Steels become a more suited solution when high wear resistance is prominent, i.e. for in extrusion dies. Therefore, examining the wear resistance and also thermal fatigue resistance of the newly developed composites will be a future work of the author. Nevertheless, present results also highlighted some limits of the PM process (e.g. surface oxidation of powder particles), which should be solved in order to get the maximum benefits from the toughening/strengthening effects reported in this work. Very important design criteria could be investigated and implemented, looking for the development of novel PM steels.

Table V-1. List of some mechanical properties of the samples developed in the present thesis

	Sample	Rel. density (%)	Rel. Density (%) (Mixtures Rule)	Hardness HV10 (sintered)	0.2% offset Yield Stress MPa	Hardness HV10 (Heat Treated)	Hardness HV10 (Heat Treated) Mixtures Rule	Fracture toughness (Ka) MPa $m^{1/2}$	Fracture toughness (Ka) Mixtures Rule MPa $m^{1/2}$
Tool Steels	AT-H13	99.6	99.6	636±5	1053±6	388±2	388	61.5±1	61.5
	MM-H13	98.6	98.6	755±18	1387±10	417±4	417	36.0±1	36.0
	HS-H13 (60%MM)	98.8	99.0	687±13	1233±40 *	405±3	406	52.0±3	46.2
Tool steel-Composites	MA (H13+20%3Y-PSZ)	95.0	-	720±40	-	452±20	-	9.0±0.3	-
	MA (H13+20%Mg-PSZ)	98.6	-	918±29	-	595±5	-	19.5±0.2	-
	MA (H13+20%TiC)	98.0	-	850±10	-	601±7	-	16.8±0.3	-

* Obtained by spherical indentation method

References

1. Ritchie, R. O. The conflicts between strength and toughness. *Nat. Mater.* **10,** 817–822 (2011).
2. Dieter, G. E. & Bacon, D. J. *Mechanical metallurgy*. **3,** (McGraw-Hill New York, 1986).
3. Li, J. C. M. & Chou, Y. T. The role of dislocations in the flow stress grain size relationships. *Metall. Mater. Trans.* **1,** 1145 (1970).
4. Song, R., Ponge, D., Raabe, D., Speer, J. G. & Matlock, D. K. Overview of processing, microstructure and mechanical properties of ultrafine grained bcc steels. *Mater. Sci. Eng. A* **441,** 1–17 (2006).
5. Meyers, M. A., Mishra, A. & Benson, D. J. Mechanical properties of nanocrystalline materials. *Prog. Mater. Sci.* **51,** 427–556 (2006).
6. Takaki, S., Kawasaki, K. & Kimura, Y. Mechanical properties of ultra fine grained steels. *J. Mater. Process. Technol.* **117,** 359–363 (2001).
7. Nardone, V. C. & Prewo, K. M. On the strength of discontinuous silicon carbide reinforced aluminum composites. *Scr. Metall.* **20,** 43–48 (1986).
8. Arsenault, R. J. & Shi, N. Proceedings of the International Conference on Low Energy Dislocation Structures Dislocation generation due to differences between the coefficients of thermal expansion. *Mater. Sci. Eng.* **81,** 175–187 (1986).

9. Zhang, Z. & Chen, D. L. Contribution of Orowan strengthening effect in particulate-reinforced metal matrix nanocomposites. *Mater. Sci. Eng. A* **483–484,** 148–152 (2008).

10. Chawla, N. & Shen, Y.-L. Mechanical Behavior of Particle Reinforced Metal Matrix Composites. *Adv. Eng. Mater.* **3,** 357–370 (2001).

11. Shewfelt, R. S. W. & Brown, L. M. HighTemperature Strength of Dispersion-Hardened Single Crystals II. Theory. *Philos. Mag.* **35,** 945–962 (1977).

12. Suryanarayana, C. Mechanical alloying and milling. *Prog. Mater. Sci.* **46,** 1–184 (2001).

13. Krauss, G. Martensite in steel: strength and structure. *Mater. Sci. Eng. A* **273–275,** 40–57 (1999).

14. Norström, L.-Å. The relation between microstructure and yield strength in tempered low-carbon lath martensite with 5% nickel. *Met. Sci.* **10,** 429–436 (1976).

15. Badmos, A. Y., Bhadeshia, H. & MacKay, D. J. C. Tensile properties of mechanically alloyed oxide dispersion strengthened iron alloys Part 1-Neural networkmodels. *Mater. Sci. Technol.* **14,** 793–809 (1998).

16. J.W. Morris, J., Guo, Z., Krenn, C. R. & Kim, Y.-H. The Limits of Strength and Toughness in Steel. *ISIJ Int.* **41,** 599–611 (2001).

17. Tsipouridis, P., Werner, E., Krempaszky, C. & Tragl, E. Formability of High Strength Dual-phase Steels. *Steel Res. Int.* **77,** 654–667 (2006).

18. Pagounis, E. & Lindroos, V. K. Processing and properties of particulate reinforced steel matrix composites. *Mater. Sci. Eng. A* **246,** 221–234 (1998).

19. Liaw, P. K. & Landes, J. D. Influence of prestrain history on fracture toughness properties of steels. *Metall. Trans. A* **17,** 473 (1986).

20. Wang, C., Wang, M., Shi, J., Hui, W. & Dong, H. Effect of microstructural refinement on the toughness of low carbon martensitic steel. *Scr. Mater.* **58,** 492–495 (2008).

21. Schwalbe, K.-H. On the influence of microstructure on crack propagation mechanisms and fracture toughness of metallic materials. *Eng. Fract. Mech.* **9,** 795–832 (1977).

22. Tetelman, A. S. & McEvily, A. J. *Fracture of structural materials*. (Wiley, 1967).

23. Song, R., Ponge, D. & Raabe, D. Mechanical properties of an ultrafine grained C–Mn steel processed by warm deformation and annealing. *Acta Mater.* **53,** 4881–4892 (2005).

24. Hohenwarter, A. & Pippan, R. Fracture and fracture toughness of nanopolycrystalline metals produced by severe plastic deformation. *Phil Trans R Soc A* **373,** 20140366 (2015).

25. Pippan, R. & Hohenwarter, A. The importance of fracture toughness in ultrafine and nanocrystalline bulk materials. *Mater. Res. Lett.* **4,** 127–136 (2016).

26. Liu, M. *et al.* A submicron mild steel produced by simple warm deformation. *Mater. Sci. Eng. A* **360,** 101–106 (2003).

27. Wiley: Ultrafine Grained Materials III - Yuntian Theodore Zhu, Terence G. Langdon, Ruslan Z. Valiev, et al. Available at:

http://www.wiley.com/WileyCDA/WileyTitle/productCd-0873395719.html. (Accessed: 12th December 2016)

28. Hickson, M. R. & Hodgson, P. D. Effect of preroll quenching and post-roll quenching on production and properties of ultrafine ferrite in steel. *Mater. Sci. Technol.* **15,** 85–90 (1999).

29. Lian, J., Baudelet, B. & Nazarov, A. A. Model for the prediction of the mechanical behaviour of nanocrystalline materials. *Mater. Sci. Eng. A* **172,** 23–29 (1993).

30. Valiev, R. Z. *et al.* Deformation behaviour of ultra-fine-grained copper. *Acta Metall. Mater.* **42,** 2467–2475 (1994).

31. Park, K.-T., Kim, Y.-S., Lee, J. G. & Shin, D. H. Thermal stability and mechanical properties of ultrafine grained low carbon steel. *Mater. Sci. Eng. A* **293,** 165–172 (2000).

32. Ma, E. Instabilities and ductility of nanocrystalline and ultrafine-grained metals. *Scr. Mater.* **49,** 663–668 (2003).

33. Kasak, A. & Dulis, E. J. Powder-Metallurgy Tool Steels. *Powder Metall.* **21,** 114–123 (1978).

34. Shephard, R. G., Harrison, J. D. L. & Russell, L. E. The Fabrication of High-Speed Tool Steel by Ultrafine Powder Metallurgy. *Powder Metall.* **16,** 200–219 (1973).

35. Rosso, M., Ugues, D. & Grande, M. A. The challenge of PM tool steels for the innovation. *J. Achiev. Mater. Manuf. Eng.* **18,** (2006).

36. Benjamin, J. S. & Volin, T. E. The mechanism of mechanical alloying. *Metall. Trans.* **5,** 1929–1934 (1974).

37. Fecht, H. J., Hellstern, E., Fu, Z. & Johnson, W. L. Nanocrystalline metals prepared by high-energy ball milling. *Metall. Trans. A* **21,** 2333 (1990).

38. Khatirkar, R. K. & Murty, B. S. Structural changes in iron powder during ball milling. *Mater. Chem. Phys.* **123,** 247–253 (2010).

39. Daróczi, L., Beke, D. L., Posgay, G., Zhou, G. F. & Bakker, H. Production and magnetic properties of nanocrystalline Fe and Ni. *Nanostructured Mater.* **2,** 515–525 (1993).

40. Jang, J. S. C. & Koch, C. C. The hall-petch relationship in nanocrystalline iron produced by ball milling. *Scr. Metall. Mater.* **24,** 1599–1604 (1990).

41. Eckert, J., Holzer, J. C., Iii, C. E. K. & Johnson, W. L. Mechanically driven alloying and grain size changes in nanocrystalline Fe-Cu powders. *J. Appl. Phys.* **73,** 2794–2802 (1993).

42. Kimura, Y., Takaki, S., Suejima, S., Uemori, R. & Tamehiro, H. Ultra Grain Refining and Decomposition of Oxide during Super-heavy Deformation in Oxide Dispersion Ferritic Stainless Steel Powder. *ISIJ Int.* **39,** 176–182 (1999).

43. Suryanarayana, C. Does a disordered γ-TiAl phase exist in mechanically alloyed TiAl powders? *Intermetallics* **3,** 153–160 (1995).

44. Pellizzari, M., Fedrizzi, A. & Zadra, M. Spark Plasma co-Sintering of hot work and high speed steel powders for fabrication of a novel tool steel with composite microstructure. *Powder Technol.* **214,** 292–299 (2011).

45. Kim, K. T. & Kim, J. S. Stage 1 Compaction Behaviour of Tool Steel Powder Under Die Pressing. *Powder Metall.* **41,** 199–204 (1998).

46. Arzt, E., Ashby, M. F. & Easterling, K. E. Practical applications of hotisostatic Pressing diagrams: Four case studies. *Metall. Trans. A* **14,** 211–221 (1983).

47. El-Eskandarany, M. S. *Mechanical alloying: For fabrication of advanced engineering materials*. (William Andrew, 2001).

48. Grinder, O. The HIP way to make cleaner, better steels. *Met. Powder Rep.* **62,** 16–22 (2007).

49. Kim, H. S. Densification mechanisms during hot isostatic pressing of stainless steel powder compacts. *J. Mater. Process. Technol.* **123,** 319–322 (2002).

50. Atkinson, H. V. & Davies, S. Fundamental aspects of hot isostatic pressing: An overview. *Metall. Mater. Trans. A* **31,** 2981–3000 (2000).

51. Takigawa, H., Manto, H., Kawai, N. & Homma, K. Properties of High-Speed Steels Produced by Powder Metallurgy. *Powder Metall.* **24,** 196–202 (1981).

52. Kimura, Y. & Takaki, S. Microstructural Changes during Annealing of Work-Hardened Mechanically Milled Metallic Powders (<I>Overview</I>). *Mater. Trans. JIM* **36,** 289–296 (1995).

53. Zoz, H., Ameyama, K., Umekawa, S., Ren, H. & Jaramillo, V. D. Alternative mechanical milling routes for grain-refinement of conventional high-speed steel powder for later consolidation by SPS....640. *Metall* **57,** 640–648 (2003).

54. Menapace, C., Lonardelli, I., Tait, M. & Molinari, A. Nanostructured/ultrafine multiphase steel with enhanced ductility obtained by mechanical alloying and spark plasma sintering of powders. *Mater. Sci. Eng. A* **517,** 1–7 (2009).

55. Zhang, Z., Vajpai, S. K., Orlov, D. & Ameyama, K. Improvement of mechanical properties in SUS304L steel through the control of bimodal microstructure characteristics. *Mater. Sci. Eng. A* **598,** 106–113 (2014).

56. Fedrizzi, A., Pellizzari, M., Zadra, M. & Marin, E. Microstructural study and densification analysis of hot work tool steel matrix composites reinforced with TiB2 particles. *Mater. Charact.* **86,** 69–79 (2013).

57. Orrù, R., Licheri, R., Locci, A. M., Cincotti, A. & Cao, G. Consolidation/synthesis of materials by electric current activated/assisted sintering. *Mater. Sci. Eng. R Rep.* **63,** 127–287 (2009).

58. Chen, W., Anselmi-Tamburini, U., Garay, J. E., Groza, J. R. & Munir, Z. A. Fundamental investigations on the spark plasma sintering/synthesis process: I. Effect of dc pulsing on reactivity. *Mater. Sci. Eng. A* **394,** 132–138 (2005).

59. Tokita, M. Mechanism of spark plasma sintering. in *Proceeding of NEDO International Symposium on Functionally Graded Materials* **21,** 22 (Japan, 1999).

60. Libardi, S., Zadra, M., Casari, F. & Molinari, A. Mechanical properties of nanostructured and ultrafine-grained iron alloys produced by spark plasma sintering of ball milled powders. *Mater. Sci. Eng. A* **478,** 243–250 (2008).

61. Zhang, H. W., Gopalan, R., Mukai, T. & Hono, K. Fabrication of bulk nanocrystalline Fe-C alloy by spark plasma sintering of mechanically milled powder. *Scr. Mater.* **53,** 863–868 (2005).

62. Munir, Z. A., Anselmi-Tamburini, U. & Ohyanagi, M. The effect of electric field and pressure on the synthesis and consolidation of materials: A review of the spark plasma sintering method. *J. Mater. Sci.* **41,** 763–777 (2006).

63. Bonifacio, C. S., Holland, T. B. & van Benthem, K. Evidence of surface cleaning during electric field assisted sintering. *Scr. Mater.* **69,** 769–772 (2013).

64. Bonifacio, C. S., Holland, T. B. & van Benthem, K. Time-dependent dielectric breakdown of surface oxides during electric-field-assisted sintering. *Acta Mater.* **63,** 140–149 (2014).

65. Arnberg, L. & Karlsson, A. Influence of powder surface oxidation on some properties of a HIPed martensitic chromium steel. *Int. J. Powder Metall. 1986* **24,** 107–112 (1988).

66. Brust, S. Transformation of Surface Oxides during Vacuum Heat Treatment of a Powder Metallurgical Hot Work Tool Steel. (2013).

67. Tool Steels, 5th Edition - ASM International. Available at: http://www.asminternational.org/search/-/journal_content/56/10192/06590G/PUBLICATION. (Accessed: 14th December 2016)

68. Viswanathan, S., Ren, W., Luk, K. & Brucher, H. G. *Manufacture of Die Casting Dies by Hot Isostatic Pressing. Crada Final Report*. (Oak Ridge National Lab., TN (United States), 1998).

69. Pagounis, E., Talvitie, M. & Lindroos, V. K. Microstructure and Mechanical Properties of Hot Work Tool Steel Matrix Composites Produced by Hot Isostatic Pressing. *Powder Metall.* **40,** 55–61 (1997).

70. Fedrizzi, A., Pellizzari, M., Zadra, M. & Dies, F. Studio del processo di macinazione meccanica di un acciaio per lavorazioni a caldo. *Metall. Ital.* (2013).

71. Fedrizzi, A. Production of steel matrix composites by mechanical milling and spark plasma sintering. (University of Trento, 2013).

72. Berns, H. Comparison of wear resistant MMC and white cast iron. *Wear* **254,** 47–54 (2003).

73. Nair, F. & Karamis, M. B. An investigation of the tribological interaction between die damage and billet deformation during MMC extrusion. *Tribol. Int.* **43,** 347–355 (2010).

74. Pagounis, E., Talvitie, M. & Lindroos, V. K. Consolidation behavior of a particle reinforced metal matrix composite during HIPing. *Mater. Res. Bull.* **31,** 1277–1285 (1996).

75. Bouvard, D. Densification behaviour of mixtures of hard and soft powders under pressure. *Powder Technol.* **111,** 231–239 (2000).

76. Olmos, L., Martin, C. L. & Bouvard, D. Sintering of mixtures of powders: Experiments and modelling. *Powder Technol.* **190,** 134–140 (2009).

77. Lange, F. F., Atteraas, L., Zok, F. & Porter, J. R. Deformation consolidation of metal powders containing steel inclusions. *Acta Metall. Mater.* **39,** 209–219 (1991).

78. Fedrizzi, A., Pellizzari, M. & Zadra, M. Influence of particle size ratio on densification behaviour of AISI H13/AISI M3:2 powder mixture. *Powder Technol.* **228,** 435–442 (2012).

79. Evans, A. G. Perspective on the Development of High-Toughness Ceramics. *J. Am. Ceram. Soc.* **73,** 187–206 (1990).

80. Angers, R., Krishnadev, M. R., Tremblay, R., Corriveau, J.-F. & Dubé, D. Characterization of SiCp/2024 aluminum alloy composites prepared by mechanical processing in a low energy ball mill. *Mater. Sci. Eng. A* **262,** 9–15 (1999).

81. Boey, F. Y. C., Yuan, Z. & Khor, K. A. Mechanical alloying for the effective dispersion of sub-micron SiCp reinforcements in Al–Li alloy composite. *Mater. Sci. Eng. A* **252,** 276–287 (1998).

82. Liu, Z. Y., Loh, N. H., Khor, K. A. & Tor, S. B. Mechanical alloying of TiC/M2 high speed steel composite powders and sintering investigation. *Mater. Sci. Eng. A* **311,** 13–21 (2001).

83. Gahr, K.-H. Z. & Doane, D. V. Optimizing fracture toughness and abrasion resistance in white cast irons. *Metall. Trans. A* **11,** 613–620 (1980).

84. McKimpson, M. G. & Scott, T. E. Processing and properties of metal matrix composites containing discontinuous reinforcement. *Mater. Sci. Eng. A* **107,** 93–106 (1989).

85. Murphy, A. M., Howard, S. J. & Clyne, T. W. Characterisation of severity of particle clustering and its effect on fracture of particulate MMCs. *Mater. Sci. Technol.* **14,** 959–968 (1998).

86. Tan, M. J. & Zhang, X. Powder metal matrix composites: selection and processing. *Mater. Sci. Eng. A* **244,** 80–85 (1998).

87. Sabirov, I., Kolednik, O., Valiev, R. Z. & Pippan, R. Equal channel angular pressing of metal matrix composites: Effect on particle distribution and fracture toughness. *Acta Mater.* **53,** 4919–4930 (2005).

88. Akhtar, F. Ceramic reinforced high modulus steel composites: processing, microstructure and properties. *Can. Metall. Q.* **53,** 253–263 (2014).

89. Parashivamurthy, K. I., Kumar, R. K., Seetharamu, S. & Chandrasekharaiah, M. N. Review on TiC reinforced steel composites. *J. Mater. Sci.* **36,** 4519–4530 (2001).

90. Baumgart, C., Weigelt, C., Krüger, L. & Aneziris, C. G. Investigations on the sintering response of steel-ceramic composites. *IOP Conf. Ser. Mater. Sci. Eng.* **139,** 012013 (2016).

91. Lu, K. & Lu, J. Nanostructured surface layer on metallic materials induced by surface mechanical attrition treatment. *Mater. Sci. Eng. A* **375–377,** 38–45 (2004).

92. Fang, T. H., Li, W. L., Tao, N. R. & Lu, K. Revealing Extraordinary Intrinsic Tensile Plasticity in Gradient Nano-Grained Copper. *Science* **331,** 1587–1590 (2011).

93. Ma, E. Eight routes to improve the tensile ductility of bulk nanostructured metals and alloys. *JOM* **58,** 49–53 (2006).

94. Howe, A. A. Ultrafine grained steels: industrial prospects. *Mater. Sci. Technol.* **16,** 1264–1266 (2000).

95. Hodgson, P. D., Hickson, M. R. & Gibbs, R. K. The Production and Mechanical Properties of Ultrafine Ferrite. *Mater. Sci. Forum* **284–286,** 63–72 (1998).

96. Wang, Y., Chen, M., Zhou, F. & Ma, E. High tensile ductility in a nanostructured metal. *Nature* **419,** 912–915 (2002).

97. Witkin, D., Lee, Z., Rodriguez, R., Nutt, S. & Lavernia, E. Al–Mg alloy engineered with bimodal grain size for high strength and increased ductility. *Scr. Mater.* **49,** 297–302 (2003).

98. Ashby, M. F. The deformation of plastically non-homogeneous materials. *Philos. Mag.* **21,** 399–424 (1970).

99. Ma, E. & Zhu, T. Towards strength–ductility synergy through the design of heterogeneous nanostructures in metals. *Mater. Today* doi:10.1016/j.mattod.2017.02.003

100. Chakrabarti, D., Strangwood, M. & Davis, C. Effect of Bimodal Grain Size Distribution on Scatter in Toughness. *Metall. Mater. Trans. A* **40,** 780–795 (2009).

101. Ameyama, K. & Fujiwara, H. Creation of Harmonic Structure Materials with Outstanding Mechanical Properties. *Mater. Sci. Forum* **706–709,** 9–16 (2012).

102. Sawangrat, C., Kato, S., Orlov, D. & Ameyama, K. Harmonic-structured copper: performance and proof of fabrication concept based on severe plastic deformation of powders. *J. Mater. Sci.* **49,** 6579–6585 (2014).

103. Okada S, S. K. Harmonic Structure Design and Mechanical Properties of Pure Ni Compact. *J. Powder Metall. Min.* **03,** (2014).

104. Ciuca, O. P., Ota, M., Deng, S. & Ameyama, K. Harmonic Structure Design of a SUS329J1 Two Phase Stainless Steel and Its Mechanical Properties. *Mater. Trans.* **54,** 1629–1633 (2013).

105. Zhang, Z., Orlov, D., Vajpai, S. K., Tong, B. & Ameyama, K. Importance of Bimodal Structure Topology in the Control of Mechanical Properties of a Stainless Steel. *Adv. Eng. Mater.* **17,** 791–795 (2015).

106. Sekiguchi, T., Ono, K., Fujiwara, H. & Ameyama, K. New Microstructure Design for Commercially Pure Titanium with Outstanding Mechanical Properties by Mechanical Milling and Hot Roll Sintering. *Mater. Trans.* **51,** 39–45 (2010).

107. Sjöström, J. & Bergström, J. Thermal fatigue testing of chromium martensitic hot-work tool steel after different austenitizing treatments. *J. Mater. Process. Technol.* **153–154,** 1089–1096 (2004).

108. Pellizzari, M., Molinari, A., Cescato, D., Ghidini, A. & S. Cantini. Thermal fatigue properties of hot-work tool steels. *Int. J. Microstruct. Mater. Prop.* **3,** 363–372 (2008).

109. Bacon, D. H., Edwards, L., Moffatt, J. E. & Fitzpatrick, M. E. Fatigue and fracture of a 316 stainless steel metal matrix composite reinforced with 25% titanium diboride. *Int. J. Fatigue* **48,** 39–47 (2013).

110. Garvie, R. C., Hannink, R. H. & Pascoe, R. T. Ceramic steel? *Nature* **258,** 703–704 (1975).

111. Hannink, R. H. J., Kelly, P. M. & Muddle, B. C. Transformation Toughening in Zirconia-Containing Ceramics. *J. Am. Ceram. Soc.* **83,** 461–487 (2000).

112. McMeeking, R. M. Effective Transformation Strain in Binary Elastic Composites. *J. Am. Ceram. Soc.* **69,** C-301 (1986).

113. Hannink, R. H. J., Murray, M. J. & Scott, H. G. Friction and wear of partially stabilized zirconia: Basic science and practical applications. *Wear* **100,** 355–366 (1984).

114. Doğan, C. P. & Hawk, J. A. Role of zirconia toughening in the abrasive wear of intermetallic and ceramic composites. *Wear* **212,** 110–118 (1997).

115. Martin, S. *et al.* Reinforcing Mechanism of Mg-PSZ Particles in Highly-Alloyed TRIP Steel. *Steel Res. Int.* **82,** 1133–1140 (2011).

116. Krüger, L. *et al.* Strength and Failure Behaviour of Spark Plasma Sintered Steel-Zirconia Composites Under Compressive Loading. *Steel Res. Int.* **82,** 1017–1021 (2011).

117. Eckner, R., Krampf, M., Segel, C. & Krüger, L. Strength and Fracture Behavior of a Particle-Reinforced Transformation-Toughened Trip Steel/ZrO2 Composite. *Mech. Compos. Mater.* **51,** 707–720 (2016).

118. Gotor, F. J., Achimovicova, M., Real, C. & Balaz, P. Influence of the milling parameters on the mechanical work intensity in planetary mills. *Powder Technol.* **233,** 1–7 (2013).

119. Mio, H., Kano, J., Saito, F. & Kaneko, K. Effects of rotational direction and rotation-to-revolution speed ratio in planetary ball milling. *Mater. Sci. Eng. A* **332,** 75–80 (2002).

120. Lutterotti, L., Matthies, S., Wenk, H.-R., Schultz, A. S. & Jr, J. W. R. Combined texture and structure analysis of deformed limestone from time-of-flight neutron diffraction spectra. *J. Appl. Phys.* **81,** 594–600 (1997).

121. B962-08 Standard Test Methods for Density of Compacted or Sintered Powder Metallurgy (PM) Products Using Archimedes' Principle, 2008 - MADCAD.com. Available at: http://www.madcad.com/library/ASTM-B962-08/. (Accessed: 5th August 2016)

122. ASTM E92 - 82(2003) Standard Test Method for Vickers Hardness of Metallic Materials. Available at: http://www.astm.org/DATABASE.CART/HISTORICAL/E92-82R03.htm. (Accessed: 3rd September 2016)

123. Herbert, E. G., Pharr, G. M., Oliver, W. C., Lucas, B. N. & Hay, J. L. On the measurement of stress–strain curves by spherical indentation. *Thin Solid Films* **398–399,** 331–335 (2001).

124. Mesarovic, S. D. & Fleck, N. A. Spherical indentation of elastic–plastic solids. *Proc. R. Soc. Lond. Math. Phys. Eng. Sci.* **455,** 2707–2728 (1999).

125. Tabor, D. *The Hardness of Metals*. (OUP Oxford, 2000).

126. Pharr, G. M., Herbert, E. G. & Gao, Y. The indentation size effect: a critical examination of experimental observations and mechanistic interpretations. *Annu. Rev. Mater. Res.* **40,** 271–292 (2010).

127. Lee, B.-W., Jang, J. & Kwon, D. Evaluation of fracture toughness using small notched specimens. *Mater. Sci. Eng. A* **334,** 207–214 (2002).

128. ASTM E399-90 (Reapproved 1997). Standard test method for plane-strain fracture toughness of metallic materials.

129. Pellizzari, M., Molinari, A. & Straffelini, G. Thermal fatigue resistance of gas and plasma nitrided 41CrAlMo7 steel. *Mater. Sci. Eng. A* **352,** 186–194 (2003).

130. Delhez, R., de Keijser, T. H. & Mittemeijer, E. J. Role of X-Ray Diffraction Analysis in Surface Engineering: Investigation of Microstructure of Nitrided Iron and Steels. *Surf. Eng.* **3,** 331–342 (1987).

131. Armstrong, R. W. Cleavage crack propagation within crystals by the Griffith mechanism versus a dislocation mechanism. *Mater. Sci. Eng.* **1,** 251–254 (1966).

132. Ayres, R. & Stein, D. F. A dislocation dynamics approach to prediction of cleavage planes in b.c.c. metals. *Acta Metall.* **19,** 789–794 (1971).

133. Lee, S., Kim, S., Hwang, B., Lee, B. S. & Lee, C. G. Effect of carbide distribution on the fracture toughness in the transition temperature region of an SA 508 steel. *Acta Mater.* **50,** 4755–4762 (2002).

134. Kimura, Y., Hidaka, H. & Takaki, S. Work-Hardening Mechanism during Super-Heavy Plastic Deformation in Mechanically Milled Iron Powder. *Mater. Trans. JIM* **40,** 1149–1157 (1999).

135. Valiev, R. Z., Korznikov, A. V. & Mulyukov, R. R. Structure and properties of ultrafine-grained materials produced by severe plastic deformation. *Mater. Sci. Eng. A* **168,** 141–148 (1993).

136. Calcagnotto, M., Ponge, D. & Raabe, D. On the Effect of Manganese on Grain Size Stability and Hardenability in Ultrafine-Grained Ferrite/Martensite Dual-Phase Steels. *Metall. Mater. Trans. A* **43,** 37–46 (2012).

137. Yang, H.-S. & Bhadeshia, H. K. D. H. Austenite grain size and the martensite-start temperature. *Scr. Mater.* **60,** 493–495 (2009).

138. Sugimoto, K., Misu, M., Kobayashi, M. & Shirasawa, H. Effects of Second Phase Morphology on Retained Austenite Morphology and Tensile Properties in a TRIP-aided Dual-phase Steel Sheet. *ISIJ Int.* **33,** 775–782 (1993).

139. Sanders, P. G., Eastman, J. A. & Weertman, J. R. Elastic and tensile behavior of nanocrystalline copper and palladium. *Acta Mater.* **45,** 4019–4025 (1997).

140. Luo, J. & Stevens, R. Porosity-dependence of elastic moduli and hardness of 3Y-TZP ceramics. *Ceram. Int.* **25,** 281–286 (1999).

141. Kramer, D. *et al.* Yield strength predictions from the plastic zone around nanocontacts. *Acta Mater.* **47,** 333–343 (1998).

142. Sauvage, X., Wilde, G., Divinski, S. V., Horita, Z. & Valiev, R. Z. Grain boundaries in ultrafine grained materials processed by severe plastic deformation and related phenomena. *Mater. Sci. Eng. A* **540,** 1–12 (2012).

143. Fillon, A. *et al.* Influence of severe plastic deformation on the precipitation hardening of a FeSiTi steel. *J. Mater. Sci.* **47,** 7939–7945 (2012).

144. Hanamura, T. & Qiu, H. Ultra-Fine Grained Steel: Relationship Between Grain Size and Tensile Properties. in *Analysis of Fracture Toughness Mechanism in Ultra-fine-grained Steels* 9–25 (Springer Japan, 2014). doi:10.1007/978-4-431-54499-9_2

145. Lesuer, D. R., Syn, C. K. & Sherby, O. D. Influence of Iron Oxide Particles on the Strength of Ball-Milled Iron. *Mater. Trans.* **47,** 1508–1517 (2006).

146. Sjöström, J. Chromium martensitic hot-work tool steels : damage, performance and microstructure. (2004).

147. Sherby, O. D. *et al.* Mechanical Property - Microstructure Relations in Iron-Carbon Alloys from 1.0 to 5.2% Carbon. *Mater. Sci. Forum* **426–432,** 11–18 (2003).

148. Zheng, R. *et al.* Enhanced ductility in harmonic structure designed SUS316L produced by high energy ball milling and hot isostatic sintering. *Mater. Sci. Eng. A* **674,** 212–220 (2016).

149. Srinivasarao, B., Oh-ishi, K., Ohkubo, T. & Hono, K. Bimodally grained high-strength Fe fabricated by mechanical alloying and spark plasma sintering. *Acta Mater.* **57,** 3277–3286 (2009).

150. Massart, T. J. & Pardoen, T. Strain gradient plasticity analysis of the grain-size-dependent strength and ductility of polycrystals with evolving grain boundary confinement. *Acta Mater.* **58,** 5768–5781 (2010).

151. Wang, Y. M. & Ma, E. Three strategies to achieve uniform tensile deformation in a nanostructured metal. *Acta Mater.* **52,** 1699–1709 (2004).

152. Blaha, J., Krempaszky, C., Werner, E. A. & Liebfahrt, W. Carbide distribution effects in cold work tool steels. in *6th International Tooling Conference* 245–252 (Karlstadt University, Schweden, 2002).

153. Wei, Q., Cheng, S., Ramesh, K. T. & Ma, E. Effect of nanocrystalline and ultrafine grain sizes on the strain rate sensitivity and activation volume: fcc versus bcc metals. *Mater. Sci. Eng. A* **381,** 71–79 (2004).

154. Malow, T. R. & Koch, C. C. Mechanical properties in tension of mechanically attrited nanocrystalline iron by the use of the miniaturized disk bend test. *Acta Mater.* **46,** 6459–6473 (1998).

155. Han, B. O., Lavernia, E. J., Lee, Z., Nutt, S. & Witkin, D. Deformation behavior of bimodal nanostructured 5083 Al alloys. *Metall. Mater. Trans. A* **36,** 957–965 (2005).

156. Neu, R. W. & Sehitoglu, H. Thermomechanical fatigue, oxidation, and creep: Part i. Damage mechanisms. *Metall. Trans. A* **20,** 1755–1767 (1989).

157. Norström, L.-Å., Svensson, M. & Öhrberg, N. Thermal-fatigue behaviour of hot-work tool steels. *Met. Technol.* **8,** 376–381 (1981).

158. Fedrizzi, A., Pellizzari, M. & Zadra, M. Sviluppo di un acciaio per lavorazione a caldo rinforzato tramite alligazione meccanica. *Metall. Ital.* **0,** (2013).

159. Gao, H., Huang, Y., Nix, W. D. & Hutchinson, J. W. Mechanism-based strain gradient plasticity— I. Theory. *J. Mech. Phys. Solids* **47,** 1239–1263 (1999).

160. Ma, E. Instabilities and ductility of nanocrystalline and ultrafine-grained metals. *Scr. Mater.* **49,** 663–668 (2003).

161. Scardi, P., Lutterotti, L. & Maggio, R. D. XRD Microstructural Characterization of Tetragonal Pure Zirconia Powders Obtained by Controlled Hydrolysis of Zirconium Alkoxides. *Powder Diffr.* **6,** 20–25 (1991).

162. Mitsuhashi, T., Ichihara, M. & Tatsuke, U. Characterization and Stabilization of Metastable Tetragonal ZrO2. *J. Am. Ceram. Soc.* **57,** 97–101 (1974).

163. Skovgaard, M., Ahniyaz, A., Sørensen, B. F., Almdal, K. & van Lelieveld, A. Effect of microscale shear stresses on the martensitic phase transformation of nanocrystalline tetragonal zirconia powders. *J. Eur. Ceram. Soc.* **30,** 2749–2755 (2010).

164. Liu, X., Wang, Z. & Bian, X. Monoclinic to cubic phase transformation of ZrO2 induced by ball milling. *J. Mater. Sci.* **39,** 2585–2587 (2004).

165. Stubičar, N., Bermanec, V., Stubičar, M., Popović, D. & Kaysser, W. A. X-ray diffraction study of microstructural evolution of some ZrO2–Y2O3–MgO powder mixtures induced by high-energy ball milling. *J. Alloys Compd.* **379,** 216–221 (2004).

166. Dai, L. H., Ling, Z. & Bai, Y. L. Size-dependent inelastic behavior of particle-reinforced metal–matrix composites. *Compos. Sci. Technol.* **61,** 1057–1063 (2001).

167. Taylor, J. C. & Matulis, C. E. Absorption contrast effects in the quantitative XRD analysis of powders by full multiphase profile refinement. *J. Appl. Crystallogr.* **24,** 14–17 (1991).

168. Pellizzari, M., Fedrizzi, A. & Zadra, M. Influence of processing parameters and particle size on the properties of hot work and high speed tool steels by Spark Plasma Sintering. *Mater. Des.* **32,** 1796–1805 (2011).

169. Bravo-Leon, A., Morikawa, Y., Kawahara, M. & Mayo, M. J. Fracture toughness of nanocrystalline tetragonal zirconia with low yttria content. *Acta Mater.* **50,** 4555–4562 (2002).

170. Miriyev, A., Grützner, S., Krüger, L., Kalabukhov, S. & Frage, N. Bonding of TRIP-Steel/Al2O3-(3Y)-TZP Composites and (3Y)-TZP Ceramic by a Spark Plasma Sintering (SPS) Apparatus. *Materials* **9,** 558 (2016).

171. Ruiz, L. & Readey, M. J. Effect of Heat Treatment on Grain Size, Phase Assemblage, and Mechanical Properties of 3 mol% Y-TZP. *J. Am. Ceram. Soc.* **79,** 2331–2340 (1996).

172. Franke, P., Ksyta, M. & Seifert, H. j. Interfacial Reactions in TRIP-Steel/ZrO2 Composites. *Steel Res. Int.* **82,** 1149–1157 (2011).

173. Pagounis, E. *et al.* Effect of thermal expansion coefficients on the martensitic transformation in a steel matrix composite. *Scr. Mater.* **34,** 407–413 (1996).

174. Selçuk, A. & Atkinson, A. Elastic properties of ceramic oxides used in solid oxide fuel cells (SOFC). *J. Eur. Ceram. Soc.* **17,** 1523–1532 (1997).

175. Hayashi, H. *et al.* Thermal expansion coefficient of yttria stabilized zirconia for various yttria contents. *Solid State Ion.* **176,** 613–619 (2005).

176. Mura, T. *Micromechanics of defects in solids*. **3,** (Springer Netherlands, 1987).

177. Yamada, Y., Kawasaki, A., Taya, M. & Watanabe, R. Effect of Debonding at the Phase Interface on Young's Modulus of Sintered PSZ/Stainless Steel Composite. *Mater. Trans. JIM* **35,** 814–820 (1994).

178. Claussen, N. Fracture Toughness of Al2O3 with an Unstabilized ZrO2Dispersed Phase. *J. Am. Ceram. Soc.* **59,** 49–51 (1976).

179. Weigelt, C. *et al.* Compressive and tensile deformation behaviour of TRIP steel-matrix composite materials with reinforcing additions of zirconia and/or aluminium titanate. *J. Alloys Compd.* **695,** 9–20 (2017).

180. Dourandish, M., Simchi, A., Tamjid Shabestary, E. & Hartwig, T. Pressureless Sintering of 3Y-TZP/Stainless-Steel Composite Layers. *J. Am. Ceram. Soc.* **91,** 3493–3503 (2008).

181. Hanson, W. B., Ironside, K. I. & Fernie, J. A. Active metal brazing of zirconia. *Acta Mater.* **48,** 4673–4676 (2000).

182. Berek, H., Ballaschk, U., Aneziris, C. G., Losch, K. & Schladitz, K. The correlation of local deformation and stress-assisted local phase transformations in MMC foams. *Mater. Charact.* **107,** 139–148 (2015).

183. Cahoon, J. R., Broughton, W. H. & Kutzak, A. R. The determination of yield strength from hardness measurements. *Metall. Trans.* **2,** 1979–1983 (1971).

184. Shen, Y. L., Fishencord, E. & Chawla, N. Correlating macrohardness and tensile behavior in discontinuously reinforced metal matrix composites. *Scr. Mater.* **42,** 427–432 (2000).

185. Martin, S. *et al.* Reinforcing Mechanism of Mg-PSZ Particles in Highly-Alloyed TRIP Steel. *Steel Res. Int.* **82,** 1133–1140 (2011).

186. Singh, J. & Alpas, A. T. High-temperature wear and deformation processes in metal matrix composites. *Metall. Mater. Trans. A* **27,** 3135–3148 (1996).

187. Zhang, H., Ramesh, K. T. & Chin, E. S. C. Effects of interfacial debonding on the rate-dependent response of metal matrix composites. *Acta Mater.* **53,** 4687–4700 (2005).

188. Pastor, J. Y., Planas, J. & Elices, M. Ambient and High-Temperature Stable Fracture Tests in Ceramics: Applications to Yttria-Partially-Stabilized Zirconia. *J. Am. Ceram. Soc.* **76,** 2927–2929 (1993).

189. Prüger, S., Mehlhorn, L., Mühlich, U. & Kuna, M. Study of Reinforcing Mechanisms in TRIP-Matrix Composites under Compressive Loading by Means of Micromechanical Simulations. *Adv. Eng. Mater.* **15,** 542–549 (2013).

190. Buffière, J.-Y., Maire, E., Cloetens, P., Lormand, G. & Fougères, R. Characterization of internal damage in a MMCp using X-ray synchrotron phase contrast microtomography. *Acta Mater.* **47,** 1613–1625 (1999).

Scientific Production

International Journals

[1] F. Deirmina, M. Pellizzari, and M. Federici, "Production of a Powder Metallurgical Hot Work Tool Steel with Harmonic Structure by Mechanical Milling and Spark Plasma Sintering," Metall. Mater. Trans. A, vol. 48, no. 4, pp. 1910–1920, Apr. 2017.

[2] F. Deirmina and M. Pellizzari, "Production and characterization of a tool steelPSZ composite by mechanical alloying and spark plasma sintering," J. Alloys Compd., vol. 709, pp. 742–751, Jun. 2017.

[3] M. Pellizzari and F.Deirmina, **"POWDER METALLURGY OPENS NEW WAYS FOR TOOL STEELS,"** *(In press)*, International Journal of Microstructure and Materials Properties.

Proceedings

[1] F. Deirmina and M. Pellizzari, "Thermal fatigue resistance of a PM tool steel with bimodal grain size", Proc. of 10th TOOL Conference, ASMET, the Austrian Society for Metallurgy and Materials, 4-7 October 2016, Bratislava, Slovakia, ISBN : 978-3-200-04786-0.

[2] F. Deirmina and M.Pellizzari, "Production of HWTS (AISI H13) Matrix Composite Reinforced With Partially Stabilized Zirconia", Proc. of the World PM 2016 Congress & Exhibition 9-13 October, Hamburg, Germany, ISBN: 978-1-899072-47-7.

[3] D. Ugues, F.Gobber, A. Pisa, M.Pellizzari and F.Deirmina, "Influence of surface finishing on the resistance to washout of an Al-Alloy die casting tool steel", Proc. of 10th TOOL Conference, ASMET, the Austrian Society for Metallurgy and Materials, 4-7 October 2016, Bratislava, Slovakia, ISBN : 978-3-200-04786-0.

[4] A.Molinari, S.Amirabdollahian and F.Deirmina, "Study Of the Pores Characteristics in the Uniaxially Cold Compacted Green Parts by Image Analysis", Proc. of the World PM 2016 Congress & Exhibition 9-13 October, Hamburg, Germany, ISBN: 978-1-899072-47-7.

Acknowledgements

Firstly, I would like to express my sincere gratitude to my advisor Prof. Massimo Pellizzari for the continuous support of my Ph.D. study, for his patience, motivation, and immense knowledge in the field. I really have been privileged for having the opportunity to work with him. I am grateful to Prof. Lutterotti for sharing his precious experience in X-ray diffraction theory and applications with me.

I am grateful to my father in law and mother in law, Bahram and Fati, who have provided me through moral and emotional support during these years. I am also grateful to my family and friends who have supported me along the way.

I thank my fellow lab mates, Marco, Samuel, Giulia and Lorena for their generous help and for all the fun we have had during the past 3 years. A special thanks goes to Sasan Amirbodalliahin and Hamid Hassani who were always there for me.